PolyPublie
Polytechnique Montréal

POLYTECHNIQUE MONTRÉAL
UNIVERSITÉ D'INGÉNIERIE

| | |
|---|---|
| **Titre:** Title: | All-Optical Ultrasound Detection Using Optical Microring Resonators and Optical Dual Frequency Combs |
| **Auteur:** Author: | Ahmed Sami Bahgat Abdelaziz |
| **Date:** | 2023 |
| **Type:** | Mémoire ou thèse / Dissertation or Thesis |
| **Référence:** Citation: | Abdelaziz, A. S. B. (2023). All-Optical Ultrasound Detection Using Optical Microring Resonators and Optical Dual Frequency Combs [Thèse de doctorat, Polytechnique Montréal]. PolyPublie. https://publications.polymtl.ca/55849/ |

**Document en libre accès dans PolyPublie**
Open Access document in PolyPublie

| | |
|---|---|
| **URL de PolyPublie:** PolyPublie URL: | https://publications.polymtl.ca/55849/ |
| **Directeurs de recherche:** Advisors: | Yves-Alain Peter, Jean Provost, & Denis Seletskiy |
| **Programme:** Program: | Génie physique |

**Ce fichier a été téléchargé à partir de PolyPublie, le dépôt institutionnel de Polytechnique Montréal**
This file has been downloaded from PolyPublie, the institutional repository of Polytechnique Montréal

https://publications.polymtl.ca

**POLYTECHNIQUE MONTRÉAL**
affiliée à l'Université de Montréal

# All-Optical Ultrasound Detection Using Optical Microring Resonators and Optical Dual Frequency Combs

**AHMED SAMI BAHGAT ABDELAZIZ**
Département de génie physique

Thèse présentée en vue de l'obtention du diplôme de *Philosophiæ Doctor*
Génie physique

Août 2023

© Ahmed Sami Bahgat Abdelaziz, 2023.

**POLYTECHNIQUE MONTRÉAL**
affiliée à l'Université de Montréal

Cette thèse intitulée :

**All-Optical Ultrasound Detection Using Optical Microring Resonators and Optical Dual Frequency Combs**

présentée par **Ahmed Sami Bahgat ABDELAZIZ**
en vue de l'obtention du diplôme de *Philosophiæ Doctor*
a été dûment acceptée par le jury d'examen constitué de :

**Stephan REUTER**, président
**Yves-Alain PETER**, membre et directeur de recherche
**Jean PROVOST**, membre et codirecteur de recherche
**Denis SELETSKIY**, membre et codirecteur de recherche
**Frédéric LESAGE**, membre
**Ricardo IZQUIERDO**, membre externe

# DEDICATION

*To my family, lab members, and Asmaa, my wife,*
*who have supported and encouraged me throughout my Ph.D. journey ...*

## ACKNOWLEDGEMENTS

After thanking Allah, many wonderful people helped me during my Ph.D. journey; I want to thank them with a few words, which would never be enough to show my gratitude.

First and foremost, I want to express my sincere gratitude to my supervisor Yves-Alain Peter for allowing me to work in his group for my Ph.D. study. This thesis would not have been possible without his guidance, advice, and mentorship. His endless patience and complete trust helped me overcome the research difficulties. I also want to thank my co-supervisors, Denis Seletisky and Jean Provost; they shared their broad knowledge and suggested ways to improve me. In addition to being an excellent mentor, I feel fortunate to have met and worked with them. Their help paved the way for me to develop more skills in other fields rather than mine. The professional skills I learned from them will help me throughout my career. Additionally, I would like to extend my appreciation to the members of the jury who dedicated their time and expertise to review and evaluate my thesis thoroughly. Their valuable comments, constructive feedback, and critical analysis have contributed to the refinement and overall quality of this work.

I am most grateful to my lab members, Cédric, Régis, Marc-Antoine, Antoine, and Thomas, for lending me their expertise and intuition to my scientific and technical problems. I was glad to work with them during these years, and I will never forget my whole life, the days we spent, and the activities we did together. I also offer my special regards and blessings to the LMF staff, Marie-Hélène, and Christophe for their continuous assistance and support in my fabrication challenges. I also want to express my gratitude to the technicians within the department, Mikaël and Yves that helped me a lot during the building and conducting of my experiments.

I am deeply grateful to the Egyptian Ministry of Defense (MOD) which generously supported my study throughout my doctoral journey. Their financial assistance provided me with the necessary resources and opportunities to pursue my studies and achieve the goals of this thesis. I extend my sincere thanks to the Fonds de recherche du Québec- Nature et technologies (FRQNT), CMC Microsystems, and Natural Sciences and Engineering Research Council of Canada (NSERC) for their unwavering support, which enabled me to fabricate devices, conduct experiments, and access research materials and equipment.

Without the support of my parents, I would never have been able to overcome the difficulties of my life. They supported me all the time; I cannot thank them enough. Finally, I would like to thank my dear wife, Asmaa, my daughters, Renad and Leen, and my son Yunus for

their endless support, understanding, and help. I would never have been able to finish this work, especially when I was about to give up, but Asmaa and her love were, and are still, always there for me and encouraged me to continue. I feel blessed to have her in my life.

*Ahmed . . .*

# RÉSUMÉ

L'imagerie ultrasonique est une technique de diagnostique non-invasivet répandue qui permet d'obtenir une image en temps réel des structures internes et des organes du corps à l'aide d'ondes acoustiques à haute fréquence. Les transducteurs piézoélectriques sont couramment utilisés dans l'imagerie par ultrasons en raison de leur simplicité et de leur faible consommation d'énergie, et ils ont joué un rôle important dans l'amélioration des capacités d'imagerie. Cependant, l'utilisation simultanée d'un grand nombre d'éléments piézoélectriques pour l'imagerie ultrasonore à haute fréquence pose des problèmes en termes de complexité électronique et de limitation du traitement des données. Pour relever ces défis, les chercheurs ont exploré des transducteurs alternatifs basés sur différent phénomènes physiques, y compris des transducteurs optiques sur puce tels que les résonateurs à micro-anneaux. Les résonateurs à micro-anneaux offrent plusieurs avantages qui en font des transducteurs à ultrasons prometteurs, notamment dû aux dimensions réduites, une sensibilité élevée ainsi qu'un immunité aux bruits d'interférence électromagnétique.

Cette thèse présente la conception, la fabrication et la mise en œuvre d'un récepteur à ultrasons entièrement optique comprenant un réseau de résonateurs à micro-anneaux. Les caractéristiques dynamiques de ce récepteur le rendent adapté à diverses applications acoustiques telle que l'imagerie ultrasonore classique et l'imagerie dynamique ultrarapide. Le réseau de résonateurs à micro-anneaux sur puce est couplé à un seul guide d'onde bus, ce qui réduit le nombre de canaux requis par rapport aux configurations traditionnelles. Lorsque le résonateur à micro-anneaux est perturbé par des ultrasons, les paramètres de sa cavité changent, ce qui entraîne un déplacement détectable du spectre de résonance. La mesure des signaux en parallèler est réalisée à l'aide de deux peignes de fréquence optiques générés par deux modulateurs électro-optiques. Cette technique génère duex spectres monomodes mutuellement cohérents et équidistants en fréquence, ce qui permet un échantillonnage efficace du grand réseau de transducteurs. Une détection hétérodyne est utilisée pour des mesures à faible bruit et à haute sensibilité.

Nous étudions les aspects théoriques et de simulation associés à ce récepteur entièrement optique. Outre la simulation du comportement des ondes optiques dans les résonateurs à micro-anneaux, nous développons un algorithme pour sélectionner les rayons d'anneau appropriés dans le réseau afin d'optimiser à la fois les performances optiques et acoustiques, ainsi que la sensibilité aux ultrasons. Nous explorons la conception théorique du double peigne de fréquence optique, en mettant l'accent sur les paramètres clés du système, et nous

simulons la conversion du signal optique dans le domaine des radiofréquences (RF) à l'aide de la technique de détection hétérodyne, garantissant un traitement fiable du signal. L'analyse des signaux simulés fait appel à deux techniques de traitement du signal : la transformée de Fourier à court terme et la conversion en bande de base.

En termes de travail expérimental, nous fabriquons un réseau de résonateurs à micro-anneaux fait de SU-8 à l'aide d'une technique de nano-impression à faible coût. La technique permet d'atteindre un facteur de qualité élevé de $6 \times 10^4$, améliorant ainsi la sensibilité de la détection des ultrasons. Nous avons construit un montage de caractérisation optique et acoustique pour déduire les caractéristiques de performance optique et acoustique des dispositifs fabriqués. Les dispositifs fabriqués présentent une réponse acoustique très sensible avec une sensibilité de $31mV/kPa$ et une pression équivalente au bruit de $161,3Pa$ avec une largeur de bande de 6 dB$de13MHz$ centrée sur la fréquence acoustique de $9MHz$.

Enfin, nous établissons un montage optique d'un peigne à double fréquence qui, à notre connaissance, introduit une nouvelle technique entièrement optique pour la détection simultanée du signal ultrasonique par le réseau de résonateurs micro-anneaux avec une sensibilité élevée. Cette thèse ouvre ainsi de nouvelles voies pour des avancées significatives dans le domaine d'acquisition acoustique ultrarapide, photonique à impulsions ultracourtes et intégration de résonateurs à micro-anneaux.

# ABSTRACT

Diagnostic ultrasound imaging is a widely used non-invasive diagnostic technique that provides real-time imaging of internal structures and organs in the body using high-frequency acoustic waves. Piezoelectric transducers are commonly employed in ultrasound imaging due to their simplicity and low power consumption, and they have played a significant role in the advancement of imaging capabilities. However, the use of a large number of piezoelectric elements working simultaneously for high frame rate ultrasound imaging has posed challenges in terms of electronic complexity and data handling limitations. To address these challenges, researchers have explored alternative transducers based on different physics and operating theories, including on-chip optical microresonators such as microring resonators. Microring resonators offer several advantages that make them promising ultrasound detectors, including small dimensions, high sensitivity, and immunity to electromagnetic interference noise.

This thesis presents the design, fabrication, and implementation of an all-optical ultrasound receiver formed of an array of microring resonators. The dynamic characteristics of this receiver make it suitable for various acoustic applications such as conventional ultrasound imaging and ultrafast dynamic imaging. The on-chip array of microring resonators is coupled to a single bus optical waveguide, reducing the required number of channels compared to traditional configurations. When the microring resonator is perturbed by an ultrasound wave, its cavity parameters change, leading to a detectable shift in the resonance spectrum. Parallel signal interrogation was achieved using dual optical frequency combs generated by two electrooptic modulators. This technique generates a spectrum of mutually coherent, frequency-equidistant single-mode emission, enabling efficient sampling of the large array of transducers. A balanced heterodyne detection scheme is used for low-noise and high-sensitivity measurements.

We investigate the theoretical and simulation aspects associated with this all-optical receiver. In addition to simulating the optical wave behavior within the microring resonators, we develop an algorithm for selecting suitable ring radii within the array to optimize both optical and acoustic performances, as well as ultrasound sensitivity. We explore the theoretical design of the dual optical frequency comb, emphasizing key parameters in the system, and simulate the down-conversion of the optical signal to the radio frequency (RF) domain using the heterodyne detection technique, which ensures reliable signal processing. The analysis of simulated signals involves two signal processing techniques: short-time Fourier transform and down-conversion to baseband.

In terms of experimental work, we fabricate an array of SU-8 microring resonators using a cost-effective soft nanoimprinting technique, achieving a high-quality factor Q of $6 \times 10^4$, thereby enhancing ultrasound detection sensitivity. We construct acoustic and optical characterization setups to deduce the optical and acoustic performance characteristics of the fabricated devices. The fabricated devices show high sensitive acoustic response with a sensitivity $31\,mV/kPa$ and noise equivalent pressure of $161.3\,Pa$ with $-6\,dB$ bandwidth of $13\,MHz$ centered at $9\,MHz$ acoustic frequency. Finally, we establish an optical dual-comb frequency setup from scratch which, to the best of our knowledge, introduces a novel all-optical technique for simultaneous detection of the ultrasound-induced signal from the array of microring resonators with high sensitivity. This thesis opens new avenues for significant advancements in the field of ultrafast acoustic acquisition, ultrashort pulses photonics, and polymer microring resonators integration.

# TABLE OF CONTENTS

DEDICATION . . . . . iii

ACKNOWLEDGEMENTS . . . . . iv

RÉSUMÉ . . . . . vi

ABSTRACT . . . . . viii

TABLE OF CONTENTS . . . . . x

LIST OF TABLES . . . . . xiii

LIST OF FIGURES . . . . . xiv

LIST OF SYMBOLS AND ACRONYMS . . . . . xviii

CHAPTER 1 INTRODUCTION . . . . . 1
1.1 Context . . . . . 1
1.2 Problem statement and motivation . . . . . 3
1.3 Originality and Impact . . . . . 4
1.4 Dissertation objectives . . . . . 5
1.5 Dissertation overview . . . . . 6

CHAPTER 2 STATE OF THE ART . . . . . 7
2.1 General . . . . . 7
2.2 Ultrasound sensing parameters . . . . . 7
2.2.1 Central Frequency and bandwidth . . . . . 7
2.2.2 Size . . . . . 8
2.2.3 Limit of detection . . . . . 8
2.3 Ultrasound sensing with optical microresonators . . . . . 8
2.3.1 Fabry-Perot cavity . . . . . 9
2.3.2 Microring resonators . . . . . 10
2.4 Optical signal interrogation . . . . . 13
2.4.1 Power detection method . . . . . 13
2.4.2 Optical frequency combs . . . . . 14
2.5 Conclusion and Challenges . . . . . 16

CHAPTER 3 THEORETICAL BACKGROUND . . . . . 18
3.1 General . . . . . 18
3.2 Microring resonator . . . . . 18
3.2.1 Optical wave propagation modes in microring resonator . . . . . 18
3.2.2 Coupling of microring resonator with waveguide . . . . . 20
3.2.3 Microring resonator cavity parameters . . . . . 23
3.3 Ultrasonic detection mechanism . . . . . 24
3.3.1 Sensitivity . . . . . 26
3.3.2 Acoustic parameters . . . . . 26
3.4 Optical frequency combs . . . . . 27
3.4.1 Theory . . . . . 27
3.4.2 Balanced heterodyne detection . . . . . 28
3.5 Conclusion . . . . . 31

CHAPTER 4 DESIGN AND SIMULATION . . . . . 32
4.1 General . . . . . 32
4.2 Design and modeling of Microring array . . . . . 34
4.2.1 Material Overview . . . . . 34
4.2.2 Waveguide and Microring resonator design . . . . . 37
4.2.3 Microring array . . . . . 39
4.2.4 Ring radii choice . . . . . 39
4.3 Optical dual frequency comb parameters . . . . . 42
4.4 Conclusion . . . . . 45

CHAPTER 5 FABRICATION PROCESS AND EXPERIMENTAL METHODOLOGY 47
5.1 General . . . . . 47
5.2 Fabrication process . . . . . 47
5.2.1 Fabrication using soft nanoimprinting technique . . . . . 48
5.2.2 Fabrication using EBL direct writing . . . . . 52
5.3 Optical and acoustic characterization setups . . . . . 52
5.4 Resonance shift interrogation using dual optical frequency comb scheme . . . 54
5.5 Conclusion . . . . . 55

CHAPTER 6 RESULTS AND DISCUSSION . . . . . 56
6.1 General . . . . . 56
6.2 Fabricated devices . . . . . 56
6.3 Characterization of fabricated devices . . . . . 58

6.4 Parallel signal interrogation using OFCs . . . . . 60
6.5 General discussion . . . . . 64
6.5.1 Fabrication and packaging techniques . . . . . 64
6.5.2 Optical power and noise limitations in dual OFC setup . . . . . 66
6.6 Conclusion . . . . . 69

CHAPTER 7 CONCLUSION AND RECOMMENDATIONS . . . . . 71
7.1 Conclusion . . . . . 71
7.2 Recommendation and potential applications . . . . . 72

REFERENCES . . . . . 74

# LIST OF TABLES


| | | |
|---|---|---|
| Table 4.1 | Material properties of Polystyrene and SU-8 polymers . . . . . | 37 |
| Table 4.2 | Matlab script results of five rings' radii following the detection criterion | 41 |
| Table 6.1 | Optical characterization parameters of a fabricated array of five microrings . . . . . | 58 |
| Table 6.2 | Comparison of the state-of-the-art on-chip optical microring sensors and their parallel detection techniques. . . . . | 70 |

# LIST OF FIGURES


Figure 1.1 (a) Ultrafast imaging of a living mouse brain, (b) Conventional fetal ultrasound. . . . . 2

Figure 2.1 Fabry-Perot Cavities: (a) Schematic of common signal interrogation technique, (b) Fabry-Perot cavity on a fiber tip, (C) Fabry-Perot cavity by encapsulation of polymer drop,(d) Submicron Silicon waveguide etalon detector (SWED). . . . . 10

Figure 2.2 Microring resonators:(a) schematic of signal interrogation (b) Polymer microring resonators, (c) SOI Microring resonator on a membrane, (d) SOI microring resonator with a slab membrane. . . . . 11

Figure 2.3 (a) Nanoimprinting of polymer waveguides, (b) schematic of nanoimprinting fabrication technique with A) opaque mold, B) transparent mold. . . . . 13

Figure 2.4 Optical signal interrogation: (a) Power detection method, (b) Principle of optical frequency combs i) time domain representation, ii) frequency domain representation, iii) interrogation of an optical signal using OFC, (c) Multiplexer-demultiplexer detection configuration of an array of microring resonators. . . . . 15

Figure 3.1 (a) Microring resonator in cylindrical coordinates, (b) equivalent 2D representation of the microring resonators in different coordinates indicating the TE and TM modes. . . . . 19

Figure 3.2 (a) Schematic drawing of a single microring resonator attached to a single waveguide showing the different electric fields and coupling parameters, (b) The normalized transmission spectrum of the single ring showing its resonance parameters. . . . . 21

Figure 3.3 Illustration of coupling region between microring resonator and waveguide: (a) top view (y-z plane), (b) cross-section view at z=0 (y-x plane). 22

Figure 3.4 (a) Waveguide response to US waves (arrows indicate compression/stretching of the dimensions of the polymer under the application of US excitation), (b) Ultrasonic signal extraction of US-induced modulation of intensity transmission by measuring optical resonance shift. . . . . 25

Figure 3.5 (a) Frequency beating interference between a local oscillator and signal electric fields on a single photodiode (b) Frequency beating interference between a local oscillator and signal electric fields on a beam splitter with ratio $\varepsilon : 1 - \varepsilon$ detected by balanced heterodyne configuration. Red: optical signal, black: electrical signal . . . . . 28
Figure 3.6 (a) Optical frequency domain of optical dual-combs, red: local oscillator comb, blue: signal interrogation comb (b) RF domain down-converted beat frequencies between every two nearest pair of the dual-comb lines. . . . . 30
Figure 4.1 Schematic of the proposed US detection setup. US disturbance (echo from e.g. blood microvessels) is detected via a 2D array of optical microring resonators. . . . . 33
Figure 4.2 (a) example of a five-ring spectrum and OFC for power detection method, (b) Schematic of dual-comb interrogation experimental setup of microresonator linear array. OFC: optical frequency comb, EOM: electro-optic modulator, UST: ultrasound transducer, SG: signal generator, PC: polarization controller . . . . . 33
Figure 4.3 (a) 1D mode extraction of slab waveguide configuration using TMT method, (b) 2D mode extraction by beam propagation solvers. . . . 35
Figure 4.4 (a) Proposed waveguide cross-section, (b) TE propagation mode profile ($E_x$). Arrow: Electric field direction. . . . . 35
Figure 4.5 Dispersion curve of SU-8 and Polystyrene for IR band. . . . . 36
Figure 4.6 (a) Bending loss with various ring resonator radii, (b) Coupling coefficient $\kappa^2$ at different ring radii, . . . . . 36
Figure 4.7 (a) Extracted effective index of the polymer waveguide at different bending radii using RSoft Femsim. Color Bar: effective refractive index of the waveguide, (b) Scattering of the ring radii following the resonance condition for arbitrary azimuth index m. . . . . 40
Figure 4.8 Extracted effective refractive index for TE mode when exposed to ultrasound pressure. . . . . 40
Figure 4.9 (a) short-time Fourier transform (STFT) technique, (b) Down-conversion to baseband technique . . . . . 41
Figure 4.10 (a) Five OFCs probe the US disturbance signal from the microring resonator array, (b) Representation of the simulated US pulses assigned to each ring resonator. . . . . 44

Figure 4.11 (a) Time-domain simulated signal out of the heterodyne detection, (b) Fourier transform representation of the simulated signal. . . . . 45
Figure 4.12 (a) The amplitudes of carrier signals after DFT calculation from STFT method and the corresponding spline fit, (b) The filtered signal from all the carrier frequencies after applying down-conversion to baseband method. . . . . 46
Figure 5.1 MRRs microfabrication process flow. . . . . 48
Figure 5.2 SEM images of the Si mold: (a) two-rings configuration, (b) Separation gap between the waveguide and the microring resonator, (c) waveguide's wall verticality, (d) waveguide's wall roughness . . . . . 49
Figure 5.3 Silanization of Silicon Mold . . . . . 50
Figure 5.4 Microfabrication of MRRs using EBL direct writing . . . . . 53
Figure 5.5 Characterization setups: (a) optical, (b) acoustic (UST: ultrasound transducer, SG: signal generator). . . . . 53
Figure 5.6 Electro-Optic frequency dual comb generation and detection schemes. . . . . 54
Figure 6.1 (a) Fabricated array of five micro-ring resonators, (b)PDMS mold, (c) SU-8 microring device array of two microrings, (d) SEM of the ring and waveguide showing the gap separation. (e) Cross-section of the fabricated waveguide. . . . . 57
Figure 6.2 EBL direct written devices: (E) optical microscopy, (F) SEM showing the gap residuals and surface roughness . . . . . 58
Figure 6.3 Resonance spectrum of five-ring microresonator array (a) extended view, (b)close up view. . . . . 59
Figure 6.4 Fabricated MRR response to US pulse generated by (a) $5\,MHz$, (b) $10\,MHz$, (c) Normalized US frequency response. . . . . 61
Figure 6.5 The resonance spectrum of the two-rings array at $T_w = 21°C$ with the derivative of the transmission vs the optical wavelength . . . . 61
Figure 6.6 Acquired output signal from the balanced heterodyne detector by the Alazar digitizer: (a) Time domain, (b) Frequency domain by Fourier transform. . . . . 62
Figure 6.7 Carried signals on each carrier frequency after down conversion to baseband: (a) $65\,MHz$ carrier frequency, (b) $115\,MHz$ carrier frequency. . . . . 63

Figure 6.8 Retrived US signals from the MMRs after the bandpass filtration around the transmitter central frequency: (a) $65\,MHz$ carrier frequency, (b) $115\,MHz$ carrier frequency. . . . . 63
Figure 6.9 Retrived US response of the two MRRs in both (a) Normal transmission mode, (b) Inclined transmission mode. . . . . 64
Figure 6.10 SEM images of the fabricated devices showing (a) curvature deformation, (b) coupling edge, and microscopic images for (c) the dicing effect on polystyrene waveguides, (d) coupling fiber drifting after gluing. 65
Figure 6.11 Effect of variation of water temperature $T_w$, on the resonance parameters of two-rings array. . . . . 67
Figure 6.12 Welch PSD noise estimation of the OFC . . . . . 68

# LIST OF SYMBOLS AND ACRONYMS

## Symbols

| | |
|---|---|
| $Q_a$ | Absorbtion loss Quality factor |
| $D(\theta)$ | Acoustic angular sensitivity |
| $f_{acous}$ | Acoustic frequency |
| $h$ | Acoustic transducer thickness |
| $K$ | Acoustic wavenumber |
| $v$ | Acoustic wavespeed |
| $m$ | Azimuth Mode Number |
| $J_0$ | Bessel function of the first kind |
| $f_d$ | Difference between optical probing frequencies |
| $n_{eff}$ | Effective Refractive Index |
| $n_x$ | Elasto-optic refractive index in x- direction |
| $n_y$ | Elasto-optic refractive index in y- direction |
| $E$ | Electric field |
| $C1$ | First elasto-optic coefficient |
| $f_t$ | Geometry limited acoustic cut-off frequency |
| $n_g$ | Group index of optical wave |
| $H$ | Magnetic field strength |
| $\Delta f$ | Offset RF driving frequency shift between the two electrooptic modulators |
| $\omega$ | Optical angular frequency |
| $\delta f$ | Optical frequency shift induced by acousto-optic modulator |
| $f$ | Optical frequency |
| $\alpha_i$ | Optical Insertion Loss |
| $I$ | Optical Intensity |
| $f_0$ | Optical offset frequency tuning |
| $L$ | Optical path length |
| $\Re$ | Optical responsivity of photodiode |
| $f_r$ | Optical ultrashort pulses' repetition frequency |
| $\lambda$ | Optical Wavelength |
| $i_{PD}$ | Photodiode current |
| $\tau_p$ | Photon lifetime inside a resonator |

| | |
|---|---|
| $\Delta\Phi$ | Pulse-to-pulse phase shift |
| $f_p$ | Optical probing frequency |
| $\lambda_p$ | Optical probing wavelength |
| $Q$ | Quality factor |
| $Q_r$ | Radiation Loss Quality factor |
| $f_{cut}$ | Resonance limited acoustic cut-off frequency |
| $\lambda_r$ | Resonance Wavelength |
| $R$ | Ring Resonator radius |
| $Q_s$ | Scattering loss Quality factor |
| $C2$ | Second elasto-optic coefficient |
| $a$ | Single bus waveguide amplitude transmission |
| $\phi$ | Single-round trip accumulated phase in microring |
| $\sigma_x$ | Stress in x-direction |
| $\sigma_y$ | Stress in y-direction |
| $\sigma_z$ | Stress in z-direction |
| $n_0$ | Stress-free index of refraction |
| $V$ | Voltage |
| $\tau$ | Waveguide Amplitude Transmission Coefficient |
| $\kappa$ | Waveguide coupling coefficient |

**Acronyms**

| | |
|---|---|
| 2D | Two dimensions |
| 3D | Three dimensions |
| AOM | Acousto-optic modulator |
| BP | Band pass |
| BPM | Beam propagation method |
| BW | Bandwidth |
| CD | Critical dimension |
| ChG | chalcogenide glass |
| CW | Continuous wave |
| DFT | Discrete Fourier transform |
| DRIE | Deep reactive ion etching |
| EBL | Electron beam lithography |
| EM | Electromagnetic |
| EMI | Electromagnetic interference |
| EO | Electrooptic |
| EOM | Electro-optic modulator |
| FBG | Fiber Bragg grating |
| FDTD | Finite difference time domain |
| FEM | Finite element method |
| FFT | Fast Fourier transform |
| FOV | Field of view |
| FP | Fabry-Perot |
| FSR | Free spectral range |
| FWHM | Full-width half maximum |
| ICP | Induction coupled plasma |
| IR | Infrared |
| LED | light emitting diodes |
| LOD | Limit of detection |
| LP | Low pass |
| MEMS | Micro-Electro-Mechanical systems |
| MIMO | Multi input multi output |
| MLL | Mode-locked lasers |
| MRR | Microring resonator |
| NEP | Noise equivalent pressure |

| | |
|---|---|
| OFC | Optical frequency comb |
| OSA | Optical spectrum analyzer |
| PC | Polarization controller |
| PDMS | Polydimethylsiloxane |
| PIC | Photonic integrated circuit |
| PMMA | Polymethylmethacrylate |
| PS | Polystyrene |
| PSD | Power spectral density |
| PZT | Piezoelectric transducers |
| RF | Radio frequency |
| RI | Refractive index |
| RIE | Reactive ion etching |
| SEM | scanning electron microscope |
| SG | Signal generator |
| SISO | Single input single output |
| SMF | Single mode fiber |
| SNR | Signal to noise ratio |
| SOI | Silicon on insulator |
| STFT | Short-time Fourier transform |
| SWED | Submicron silicon waveguide etalon detector |
| TE | Transverse electric |
| TL | Tunable laser |
| TM | Transverse magnetic |
| TMT | Transfere matrix method |
| ULM | Ultrasound localization microscopy |
| US | Ultrasound |
| UV | Ultraviolet |
| VIS | Visible |
| WGM | Whispering gallery mode |

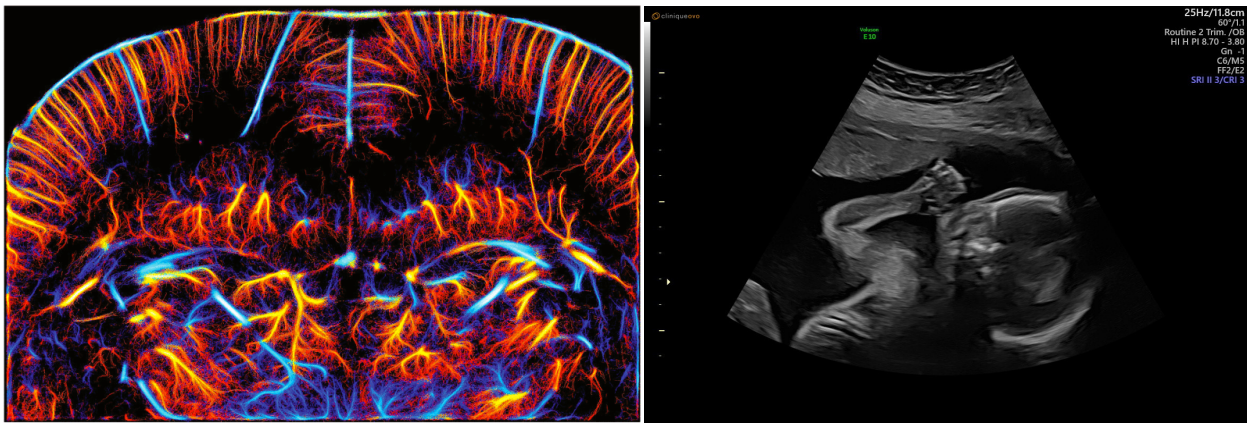
# CHAPTER 1 INTRODUCTION

## 1.1 Context

Diagnostic ultrasound imaging, also known as ultrasonography, has emerged as the predominant medical imaging technology since its introduction to the biomedical community in 1970. Its widespread adoption and utilization have led to significant growth in the ultrasound devices market, with North America alone witnessing a market value of USD 1.81 billion in 2022. Projections indicate further expansion, with an expected market value of USD 2.31 billion within the next five years [1]. This non-invasive diagnostic technique enables real-time visualization of internal structures and organs within the body through the utilization of high-frequency acoustic waves. Its significance lies in its ability to allow the diagnosis and monitoring of various medical conditions, including but not limited to pregnancy complications, cardiovascular ailments, liver and kidney disorders, and musculoskeletal injuries safely and avoiding any exposure to ionizing radiation. Moreover, it is often used for providing guidance during minimally invasive procedures, such as biopsies and needle aspirations, ensuring accuracy and reducing potential risks [2].

Ultrasound imaging employs an acoustic transducer array, commonly piezoelectric, to transmit ultrasound waves that deeply penetrate tissues. These waves subsequently rebound as echoes from various organs and tissues, carrying valuable information regarding their static and dynamic characteristics and their spatial locations. The same transducer array functions as a receiver, converting the echo waves into electrical signals, which are then processed to construct the detailed ultrasound image [3].

Different propagation patterns of sound waves are utilized for tissue imaging, such as the raster-focused beam and the plan-wave acoustic pulse. The raster-focused beam approach yields high-resolution sonographic images, along with limitations in terms of field of view and frame rates. In contrast, the plan-wave emission covers a wider field of view with a single acoustic transmission pulse, facilitating high-frame-rate imaging in this expanded area. However, the image quality and spatial resolution may suffer due to this high frame-rate imaging. In this context, a trade-off between resolution and high frame rate becomes a crucial consideration, dependent on the specific application. If the objective is to capture anatomic properties, a high resolution is essential, irrespective of the frame rate. Conversely, when the desired information relates to tissue dynamics, prioritizing a high frame rate becomes the preferable choice.



(a) (b)

Figure 1.1 (a) Ultrafast imaging of a living mouse brain [4],(b) Conventional fetal ultrasound.

Ultrafast ultrasound imaging is one of the promising techniques that utilize thousands of frame rates per second providing valuable information for tissue dynamic imaging [5–7] that helps real-time assessment of tissue motion, and visualizing rapid physiological events, such as 3D volumetric blood flow dynamics [8], cardiac function, and tissue elasticity [9, 10]. Figure 1.1a shows an example of blood movement inside rat's brain microvessels as constructed by ultrafast ultrasound microscopy in comparison to conventional ultrasound imaging (figure 1.1b). Furthermore, ultrafast ultrasound techniques have the potential to improve the detection and characterization of certain diseases, such as vascular disorders [11], cardiac abnormalities [12], and musculoskeletal conditions [13].

This technique utilizes high-frame rate plane-wave acoustic pulses to increase the capability of tracking 3D transient phenomena occurring in the millisecond range within a single ultrafast acquisition. In addition, the image spatial resolution of ultrafast imaging is significantly enhanced by increasing the number of individually connected piezoelectric transducers within the sensing array, which reached its limit due to the electronic readout circuit's complexity and requirement of extensive acquisition time. Furthermore, despite the widespread of US piezoelectric transducers, they suffer from some performance-limiting aspects, such as high acoustic coupling losses that require an acoustic matching layer, limited bandwidth around piezoelectric resonance frequencies, large device sizes [14].

In that manner, the simultaneous acquisition in space and time dramatically enlarges the size of the data sets required for an efficient ultrasound imaging system with complex sensing capabilities such as high sensitivity, high signal-to-noise ratio (SNR), a wide frequency bandwidth, and parallel signal interrogation [15]. The high sensitivity and signal-to-noise

ratio enable the detection of relatively low signals representing either low-reflection tissue parts or positions of deep tissue parts. Furthermore, some rapid acoustic phenomena require ultrafast detection techniques to be acquired. The parallel signal interrogation empowers simultaneous data readout from all the sensors within the imaging array, which is essential for high frame-rate imaging.

### 1.2 Problem statement and motivation

Piezoelectric transducers are widely acknowledged for their broad dynamic range and simple driving input, almost without power limitations [16]. However, the imaging capabilities of piezoelectric transducer arrays are constrained by various limitations. These include significant acoustic coupling loss necessitating the use of an acoustic matching layer, limited bandwidth around resonance frequencies, and large device sizes [14]. Moreover, piezoelectric transducers lack compactness, robustness, and immunity to electromagnetic interference (EMI) [17]. Moreover, for the best US imaging system, the ideal 2D piezoelectric array should contain at least $128 \times 128$ individual elements that add more complexity to the size of the electronic readout circuits and extensive acquisition time accompanied by an increasing cross-talk for compacted electrical connections. To overcome some of these limitations, alternative detection approaches have been explored, such as MEMS piezoelectric transducers [18, 19] and MEMS capacitive transducers [20–22]. However, these alternatives still face challenges related to complex readout circuits and cross-talk issues, making them unsuitable replacements for conventional piezoelectric transducers.

Several studies have investigated on-chip optical techniques for ultrasound (US) detection, including refractive, reflective, and interferometric methods. Among these techniques, optical microring resonators have emerged as a promising approach that enables miniaturization and integration in small-size applications. Polymer microresonators, in particular, have attracted significant interest due to their unique properties, such as high sensitivity and immunity to EMI noise. They exhibit a broad acoustic bandwidth response, compact footprint, and robust operation. Furthermore, they eliminate the need for an acoustic coupling medium during ultrasound detection. Finally, with appropriate modulation, optics-based sensors can achieve quantum-limited detection, only limited by the statistic noise resulting from photon-number fluctuations.

However, the parallel acquisition of ultrasound responses from the entire sensing array remains challenging. The standard optical signal interrogation method relies on probing at a linear part of the resonance spectrum using a single optical wavelength. As the number of sensors being detected simultaneously increases, multiple optical wavelength sources equal

to the total number of sensors in the array are required. These sources are combined using wavelength-division multiplexing and demultiplexing systems, resulting in a bulky and expensive setup [14, 23].

A promising technique to address these challenges is the use of optical frequency combs (OFC). OFC involves introducing a spectrum of mutually coherent, frequency-equidistant single-mode light emissions [24, 25]. This approach provides a stable and precise ruler in the optical frequency domain, potentially enabling massively parallelized and accurate detection of ultrasound variations. As such, the broad optical spectrum offered by OFC is advantageous for multidimensional ultrasound detection, particularly in ultrafast ultrasound microscopy applications. Additionally, the optical frequency dual-comb technique enables rapid and systematic measurement of the spectral response of the ring array, requiring only one photodetector [26]. Furthermore, it downsamples the optical signal into the radio frequency (RF) domain, allowing for sampling using conventional digitizing components. Overall, an array of optical microresonators can be interrogated on a sub-microsecond response time scale, which is suitable for ultrafast ultrasound imaging.

In conclusion, employing an all-optical receiver approach in ultrasound imaging offers several benefits, including enhanced sensitivity in ultrasound detection, immunity to electromagnetic wave interference, and the ability to handle wide bandwidth signals. The use of optical frequency combs enables parallel signal acquisition from an array of transducers in a single pulse, leading to a significant reduction in the complexity of the acquisition systems required.

However, it is important to note that the all-optical detection scheme operates in the transponder configuration, which necessitates the presence of ultrasound transmitter elements. This inclusion of transmitter elements introduces additional complexity to the system. On the other hand, employing a separate transmitter and receiver configuration provides greater flexibility in acquiring acoustic echoes from various angles, as opposed to being limited to the vertical direction as observed in the transceiver configuration.

### 1.3 Originality and Impact

Extensive research has been dedicated to US detection utilizing piezoelectric transducers, leading to significant advancements. However, some challenges in terms of complexity and imaging limitations have been encountered along the way. Recognizing the importance of achieving different designs and clinical compatibility, researchers are now exploring alternative technologies to support advancements in the ultrasonic imaging field. In that manner, we wish to investigate the development of nanoimprinting techniques in the fabrication of

an ultra-high Q optical microring array coupled to a single bus waveguide. We harness the significant advantages of OFCs technology in detection. The use of dual OFCs introduces a novelty in the detection of US multidimensional applications. We predict that using an array of MRRs interrogated by OFCs leads to a better capture of the US perturbations caused by the reflection of the acoustic plane wave scattered from the internal tissue. In addition, the single-input single-output (SISO) configuration of the MRRs will dramatically reduce the complexity and parasitic electronic cross-talk present in alternative multi-input multi-output (MIMO). Moreover, the response of all the MRRs in the array will be captured by a single laser pulse in a time range of sub-microseconds that introduces ultrafast imaging capabilities. Furthermore, the extraordinary stability and multiplexing of the optical frequency combs lead to highly sensitive and precise measurements of the optical variations that enable the novelty of deep US imaging with MRRs array. These achievements will rapidly advance state-of-the-art knowledge in many disciplines of research; ultrafast acoustic acquisition, ultrashort pulse photonics, and MRRs integration.

### 1.4 Dissertation objectives

This dissertation focuses mainly on investigating an all-optical approach for ultrasound detection, aiming to replace the receiver array and electronic acquisition system of piezoelectric transducers with an array of optical microring resonators (MRRs) that are interrogated in parallel using optical frequency dual-comb. Given that this readout technique represents a novel concept in detection, the main objective is to establish a proof of concept by successfully capturing ultrasound (US) signals from an array composed of a limited number of microring resonators. The proposed method demonstrates the potential for various applications, including ultrafast ultrasound imaging, where it is crucial to achieve superior performance compared to conventional ultrasound imaging techniques. This main objective leads to a set of specific objectives as follows:

1. Simulation and design of the array of microring resonators coupled to a single waveguide, operating within a specific narrow optical bandwidth defined by the optical frequency combs. The design is to be optimized for utilizing polymer optical materials for the resonators and taking into account the limitations presented by the existing developed and optimized microfabrication process.

2. Development and optimization of the fabrication process of the designed polymer microring resonators' array. In addition, all the optical and acoustic characterization steps are to be performed to ensure meeting the design specifications.

3. Implantation and optimization of an optical frequency dual-combs setup. This novel setup enables parallel interrogation of the signal changes observed in a fabricated microring resonator array when exposed to US disturbance.

## 1.5 Dissertation overview

In chapter 2, we will review the state of the art of optical microresonator-based microsensors and their related key sensing parameters to determine the most suitable design and configuration from our application point of view, mentioning their compatibility and properties. Moreover, we will review the fabrication techniques as well as the interrogation methods and their advantages and limitations.

In chapter 3, we detail the theoretical and mathematical models representing the MRR theory and the ultrasound detection mechanism. Optical frequency combs generation theory using an electro-optic modulator is also presented.

The optical design of the MRRs array and the choice of ring radii to comply with the optical frequency combs interrogation method is investigated in chapter 4. A simulated complete ultrasound signal interrogation by optical frequency combs is also proposed.

In chapter 5, we outline the processes and techniques utilized to fabricate the polymer MRR array required for our transducer. We provide an overview of the fabrication processes, materials, and equipment used. Additionally, we discuss the characterization techniques employed to assess the quality and functionality of the fabricated components. Finally, we detail the design and implementation of the optical characterization setup and the optical dual-comb frequency apparatus.

In chapter 6, we performed a geometrical assessment of the devices ensuring the successful fabrication. Additionally, we characterized optically and acoustically the fabricated devices as well as the parallel interrogation of the signal from the whole array at once showing the results. Finally, we address the general discussion that focuses on the performance of the proposed all-optical ultrasound detection system and its limitations.

Finally, Conclusions, potential applications, and future recommendations are discussed in chapter 7.

# CHAPTER 2 STATE OF THE ART

## 2.1 General

As we introduced in the previous chapter, we focus on miniaturized optical resonators for ultrasound detection due to their promising advantages in size, sensitivity, and integration. We will start with a review of the current state of the art of the sensing parameters of ultrasound imaging systems. Moreover, we will investigate the current technology in optical resonators from the detection theory, the acoustic performance, and the fabrication point of view. In addition, we will investigate the signal interrogation techniques of the sensors and the ability of array integration. Finally, we will compare the acoustic performance of these different resonators to conclude with our system's design requirements and characteristics.

## 2.2 Ultrasound sensing parameters

Ultrasound imaging transducers are characterized by essential parameters that play a crucial role in determining the quality and accuracy of ultrasound images such as center frequency, bandwidth, shape and size, aperture, and detection sensitivity. In order to enhance the detection in the ultrasound imaging system, all these critical parameters should be considered.

### 2.2.1 Central Frequency and bandwidth

Two parameters define ultrasound's working frequency: the central frequency $f_{acous}$ and the bandwidth $\Delta f_{acous}$. The central frequency determines the expected wave properties inside the tissue, like the attenuation and scattering that define the penetration depth and resolution. For the penetration depth, the attenuation is related to the frequency, which varies between the frequency $f$ and the square of the frequency $f^2$ [27], which means that a lower frequency is more suitable for deep imaging tissues. In contrast, the lateral resolution in the far field is linked to the diffraction limit that is proportional to half of the wavelength ($\lambda \, \alpha \, f^{-1}$) [28]. A trade-off between the resolution and the penetration should be considered in the choice of the central frequency. For conventional ultrasound applications, the central frequency is $2-15\,MHz$ with a penetration depth of $20-0.5\,cm$ and a lateral resolution of $70-200\mu m$ [4,15]. As per the bandwidth, it is related mainly to the ultrasound transducer. The higher the bandwidth, the more spectral capability and spatial resolution the sensor can detect without integrating multiple sensing traducers with different central frequencies and bandwidths in the imaging system. The relative bandwidth term is used to compare the other transducers and

is defined by the ratio between the bandwidth and the central frequency. The piezoelectric ultrasound transducers are known for their low relative bandwidth ($\Delta f_{acous}/f_{acous}$) $60\%-80\%$ while the optical ultrasound transducers have a relative bandwidth $> 200\%$. Zhang *et al.* introduced an optical microring resonator with an acoustic frequency response from dc to $-3dB$ bandwidth of $350\,MHz$ [29].

### 2.2.2 Size

In ultrasound arrays, the pitch between sensors determines the size of the whole array. By employing smaller-diameter sensors within the array, it becomes possible to achieve a minimal inter-sensor pitch while taking into consideration cross-talk margins. For efficient high-resolution acoustic imaging, a larger aperture of the sensing array is required while the pitch between every two elements is limited by the smallest acoustic wavelength in the imaging system. Furthermore, the size of the sensor element limits the acceptance angle, which is the sensitivity of the sensing element to a point source at an angle relative to its axis. For the same acoustic frequency, the smaller the element size, the larger the acceptance angle. For piezoelectric transducers, the sensitivity is massively affected when reducing the element's size, unlike optical resonators that can be miniaturized without losing sensitivity. Hao Li *et al.* investigated $60\mu m$ diameter polymer microring resonator that has a wide acceptance angle [30].

### 2.2.3 Limit of detection

The limit of detection (LOD) is the minimum ultrasound pressure the transducer can sense. For the acoustic transducers, the term noise equivalent pressure (NEP) is commonly used to express the lowest pressure level detected compared to the noise level. In order to image deeper tissue, NEP range of $1Pa$ or below is required. For the resonator-based transducers, the optical signal generated by the ultrasound variation is multiplied by the number of roundtrips light makes inside the cavity, increasing its sensitivity to high levels. For the Fabry-Perot cavity, NEP is $24Pa$ [31], while in the polymer microring resonator, it is $6.8Pa$ [32].

## 2.3 Ultrasound sensing with optical microresonators

In optical microresonator-based sensors, the light bounces in a microcavity following its physical boundary conditions. Due to the resonance condition, only given wavelengths are allowed inside the cavity. Any disturbance of the microcavity parameters is optically amplified by the number of trips the light bounces inside the cavity, making it a promising technique in

ultrasound detection compared to non-resonating techniques. When exposed to a disturbance generated by ultrasound pressure, mechanical deformation of the cavity dimensions alters the physical characteristics of light. It allows an accumulated optical change in both the reflected and transmitted optical signal that can be detected and demodulated to the original acoustic signal. The optical most widely used microresonators include Fabry-Perot cavities [33–37], and microring resonators [14, 17, 38, 39].

### 2.3.1 Fabry-Perot cavity

In the Fabry-Perot cavity, two parallel surfaces form the cavity. These two surfaces act as mirrors. The resonance wavelengths are defined based on the cavity's physical dimensions, such as the gap between the plates, the effective index of the media between the two mirrors, the reflectivity, and the transmission of the two mirrors. For ultrasound detection, as described in figure 2.1a, the highly reflective mirror is exposed to ultrasound disturbance. At the same time, the other mirror is used for light signal in-and-out coupling and detection. The acoustic pressure representing disturbance affects the distance between the cavity mirrors, causing a shift in the resonance wavelength. With the help of an optical circulator, the reflected signal is detected by a photodiode and data acquisition system, and then correlated to the original ultrasound signal. The sensitivity of the ultrasound signal is dependent on the cavity performance parameters, such as the quality factor. In order to achieve high-quality factor and sharp resonances, the reflectivity of the two mirrors should be as high as 99%.

A Fabry-Perot cavity can be fabricated on a fiber tip with either two gold mirrors and a polymer layer encapsulation [42] or a polymer drop of $30\mu m$ diameter on the tip of a gold coated fiber [40], figure 2.1b, offering good properties such as small size, and simple configuration and high reliability. Furthermore, another technique including polymer droplets on a substrate and encapsulation by another polymer material with a lower refractive index to form the mirrors [41], figure 2.1c, offers a massive number of sensor integration on-chip and could be suitable for high-resolution imaging. Another configuration can be fabricated by replacing the two mirrors with two Bragg reflectors or a combination between a single mirror and Bragg reflector. The Bragg reflectors can be carefully designed to achieve the optical stop bands that can be used for ultrasound detection. The cavity has tiny dimensions that allow dense arrays in a small area. Shnaiderman et al. [39] introduced a submicron silicon waveguide etalon detector (SWED) on SOI, figure 2.1d. It consists of four parts; Bragg grating, cavity, spacer, and Ag layer. This technique offers a tiny sensor ($200nm \times 500nm$) with high US bandwidth up to $230MHz$ and high sensitivity. This technique is limited to only a linear array because of the Bragg grating length. For array configuration, a fiber bundle can be

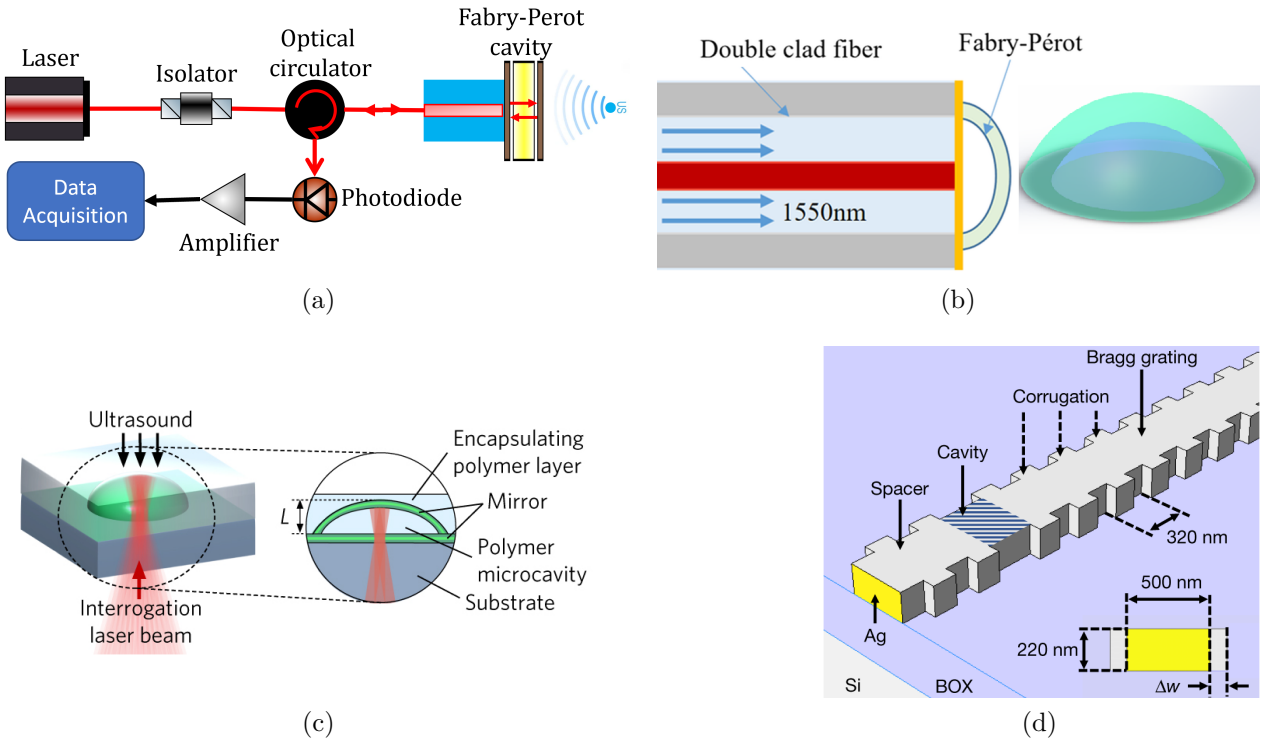



Figure 2.1 Fabry-Perot Cavities: (a) Schematic of common signal interrogation technique, (b) Fabry-Perot cavity on a fiber tip [40], (C) Fabry-Perot cavity by encapsulation of polymer drop [41], *reproduced with permission, Copyright 2017 Nature Photonics*, (d) Submicron Silicon waveguide etalon detector (SWED) [39], *reproduced with permission, Copyright 2020 Nature Photonics*.

used to acquire the signal from the array of cavities and therefore for simultaneous detection. However, detecting the signal from each Fabry-Perot channel collected individually through a laser source and optical circulator makes the interrogation system complex and bulky.

### 2.3.2 Microring resonators

Optical microring resonators (MRRs) based sensors, especially for US detection, received great attention in the last decade [23, 29, 30, 41, 43–45]. They have unique properties, such as high sensitivity and low noise-equivalent pressure. They have a wide acoustic bandwidth response, compact footprint, and robust operation. Microring resonators are a type of whispering gallery mode (WGM) resonator that consists of a ring-shaped waveguide critically coupled to a bus waveguide forming optical input and output [46, 47]. The gap controls the evanescent coupling between the waveguide and the ring. The resonance wavelengths are determined based on the ring's optical and dimensional parameters. The general idea for ultrasound detection is the same as for the Fabry-Perot cavity; the ultrasound pressure

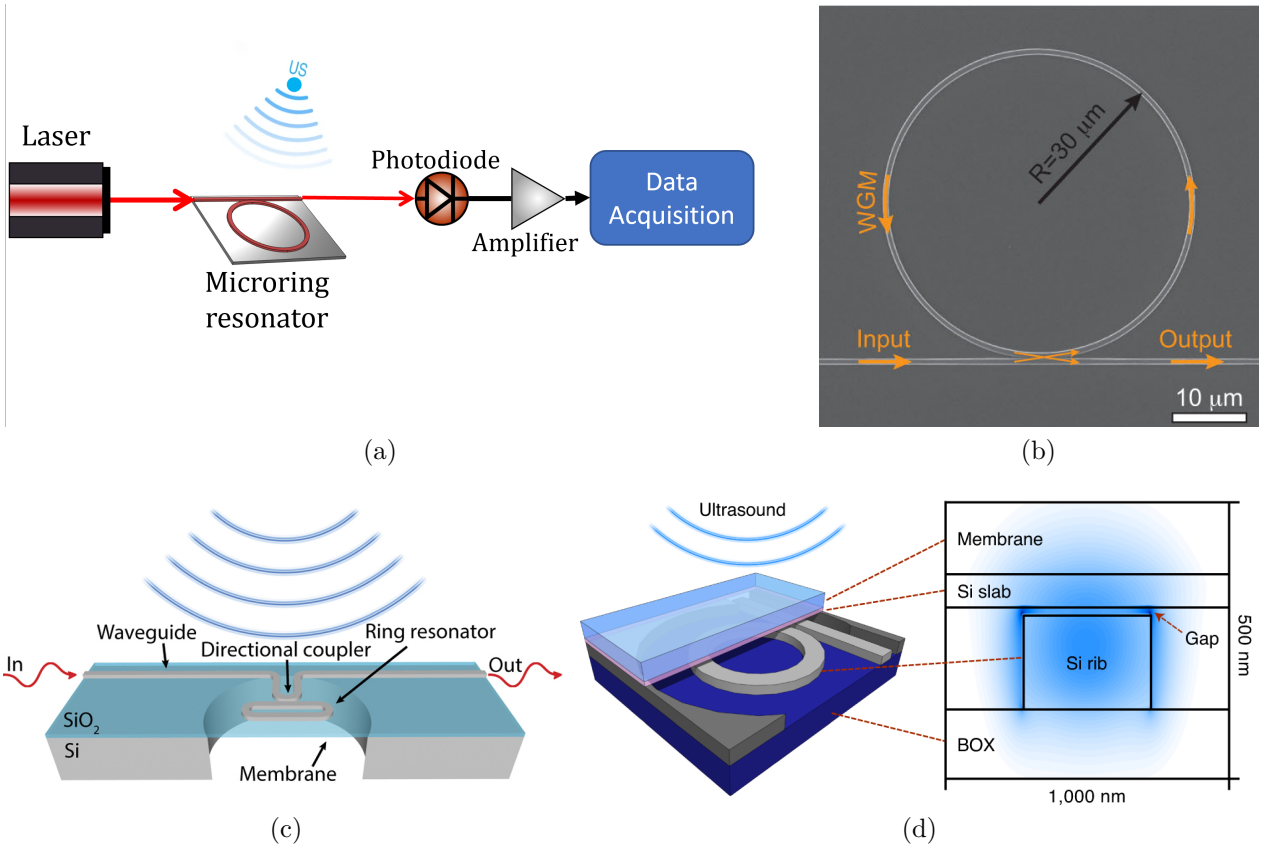



Figure 2.2 Microring resonators:(a) schematic of signal interrogation (b) Polymer microring resonators [32], (c) SOI Microring resonator on a membrane [43], (d) SOI microring resonator with a slab membrane [44], *reproduced with permission, Copyright 2021 Nature Photonics*.

disturbs the resonator parameters causing a shift in the resonance wavelength.

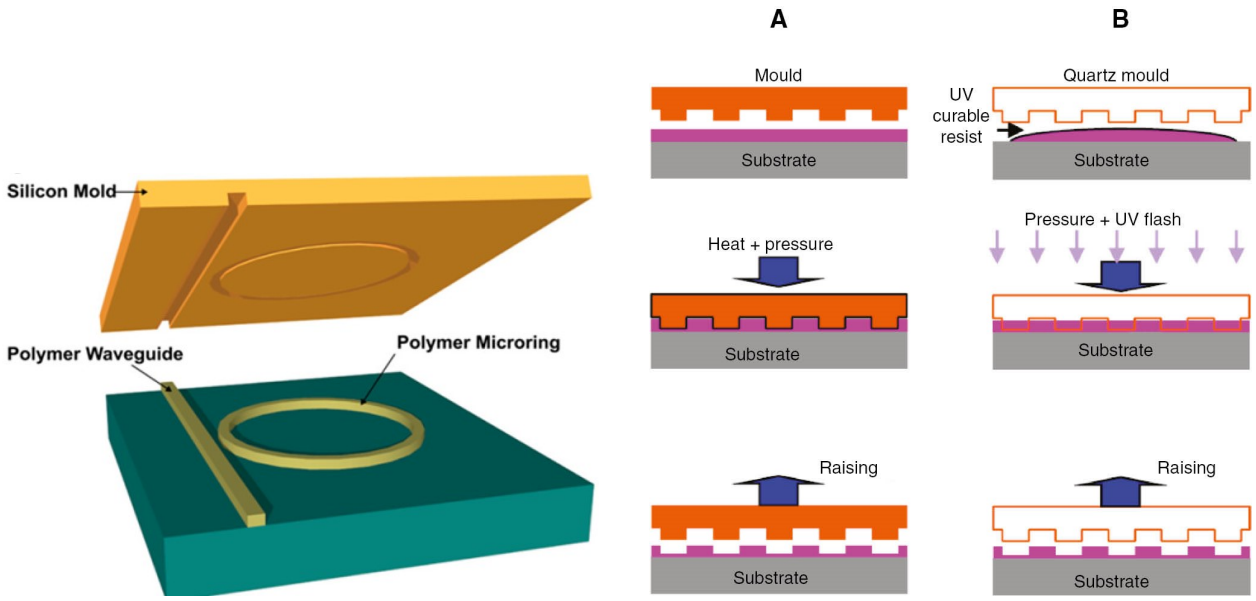
In the microring resonator, there are different ways to disturb the cavity parameters, either by direct or indirect cavity deformation. For direct deformation, the ring resonator is made from an elastic polymer material that is deformed by acoustic pressure. The deformation of the ring resonator affects the optical resonance in two ways: by changing the cross-section dimensions of the ring and by the elasto-optic effect [48]. The elasto-optic effect is the change in the material's refractive index when exposed to external stress. For the indirect deformation, a membrane is exposed to the ultrasound disturbance that mechanically deforms the microring resonator causing optical resonance perturbation [43, 44].

The microring resonator direct disturbance technique is limited to elastic materials, such as polymers. Polymers such as polystyrene (PS) [17], SU-8 [32], and polymethylmethacrylate (PMMA) [49, 50], have a low Young's modulus (around 2-5 GPa) and relatively low optical loss over visible (VIS) and infrared (IR) spectrum. Despite having low optical loss, excellent

acoustic sensitivity, and wide acoustic bandwidth up to $300MHz$, polymers have limited fabricated techniques with direct writing or nanoimprinting fabrication process. In addition, the low index of the polymer materials requires larger ring radii to avoid radiation loss which limits the angular-dependent acoustic sensitivity [32]. On the other hand, the indirect technique can use any other optical materials like silicon nitride [14], silicon dioxide [45], chalcogenide glass (ChG) [14], and silicon [43, 44] that can be fabricated using the current well-established microfabrication processes. It has relatively small ring radii compared to polymer microrings, enabling denser and high-resolution acoustic sensing. However, the mechanical membrane oscillation limits the acoustic bandwidth. Additionally, the sensor pitch is limited to the membrane radius, which is larger than the sensing element itself.

The easy, fast, scalable, and economical way of patterning polymer structures is through UV lithography. This technique can achieve resolutions down to $1\mu m$, which limits the achievable quality factor of the fabricated microrings [51, 52]. In order to overcome the resolution limitation of traditional UV lithography, electron beam lithography (EBL) was used to define polymer structures [32]. Instead of UV illumination through a mask, a direct, focused electron beam (a few nanometers in diameter) is used for direct writing. However, EBL takes much more time to scan all the features on the wafer than the UV method's single-shot exposure. Besides, using the method of direct polymer writing with EBL limits the aspect ratio [54] and generates higher surface roughness that increases the optical loss.

The nanoimprinting lithography technique offers a practical approach to achieve better quality, especially for polymers. It allows the fabrication of several types of polymers without the need to be photosensitive [55]. With this technique, a mold with predefined features is pressed into the polymeric material causing direct mechanical deformation of the polymer achieving structures of nano/micro-scale (complementary with the mold features), as described in figure 2.3. This process is done under certain curing conditions controlled by a nanoimprinting machine depending on the polymer material, either with curing temperature under casting pressure with opaque mold or UV irradiation under casting pressure with transparent mold. Many works used this method and reached high Q factors, and nanoscale features [17, 30, 38, 48, 50]. From the parallel sensing point of view, it is feasible to integrate an array of optical microresonators on the same bus waveguide enabling single input and single output (SISO) configuration for signal acquisition from the whole sensing array [38] making it the preferable approach for parallel sensing.




(a) (b)

Figure 2.3 (a) Nanoimprinting of polymer waveguides [17], (b) schematic of nanoimprinting fabrication technique with A) opaque mold, B) transparent mold [53], *reproduced with permission, Copyright 2015 Applied physics A.*

## 2.4 Optical signal interrogation

### 2.4.1 Power detection method

Interrogating the change of the cavity parameters is essential to extract the ultrasound information. The common technique for signal interrogation is the power detection method. In this method, the operating laser wavelength is set at the maximum slope of the cavity resonance spectrum, figure 2.4a. The response of the cavity to US variations is detected through US-induced resonance shift, in turn translating to a change in the transmitted/reflected optical power detected by a high-speed photodiode connected with a data acquisition system [56, 57]. While the technique has been widely used, it cannot interrogate a simultaneous readout signal from an array of MRRs without needing multiple laser sources and corresponding sensors, making the system bulky and expensive. In addition, sensitivity to background temperature variations poses another challenge when using this technique [23]. Furthermore, the time-dependent sweeping of the laser wavelength over a particular bandwidth will miss most US pulse information due to the transient nature of the pulse.

In the context of experimental parallel sensing state-of-the-art, Westerveld *et al.* introduced a detection array of 128 sensors that are interrogated using 4 optical 32-channel multiplexing

units to combine 128 narrow-band filtered LED lights to be used as input to the array system, figure 2.4c. For the output, the same number of demultiplexers, 128 photodetectors, and 128 digitizer channels were used [58]. Clearly, such an approach cannot be scaled for high-resolution US imaging, requiring an order of magnitude or more increase in the number of simultaneously detected channels. Lately, many works have introduced optical frequency combs (OFC) for signal interrogation in many optical applications due to their precise optical measurements [24, 25].

### 2.4.2 Optical frequency combs

The importance of OFC in detection arises from many developments in the stabilization of femtosecond OFC that improves the robustness [60]. Moreover, recent works investigated combs with ultra-low noise, only limited by the uncertainty principle of quantum physics [61]. Looking to the OFC in the time domain (figure 2.4b.i), a train of ultrashort pulses with a fixed pulse repetition rate $f_r$ is generated by a mode-locked laser or electro-optic modulators. This repetition period defines the inverse of the line spacing in the optical spectrum. The cavity parameters, such as length and group velocity, affect the period of the pulses' envelope. The dispersion inside the cavity introduces different velocities for the carrier wave and the envelope, resulting in a cyclic phase-slip $\Delta\phi$ between the two, observed at each consecutive pulse.

In addition, the difference in the intracavity phase and group velocities of the pulse introduces what is known as a carrier envelope offset frequency $f_0$. The spectrum is composed of a set of mutually coherent frequency-equidistant single-mode comb teeth in the frequency domain (figure 2.4b.ii). Knowledge about the absolute frequency of one comb tooth is used to determine the absolute frequency of other comb teeth [62]. This technique offers precise optical bandwidth measurements in a single pulse [59,63,64] as shown in figure2.4b.iii, by measuring the change of the intensity amplitudes and frequency shifts of the OFCs. This is done by measuring the beat notes between the reference frequency comb and the perturbed frequency comb. Some researchers introduced digital optical frequency combs (DOFC) spectroscopy in ultrasound detection with materials other than polymers [14, 64, 65], however, much research is needed including the integration of OFCs in ultrasound detection and development of cost-effective materials. Despite the full spectrum given by the DOFC in a certain optical bandwidth, the limited optical bandwidth and crosstalk during demodulation put more constraints on the performance of the microresonator arrays in these techniques [66].

Various techniques are available for generating optical frequency combs, including mode-locked lasers (MLL), Kerr combs [67], and electrooptical (E-O) combs. Among these tech-

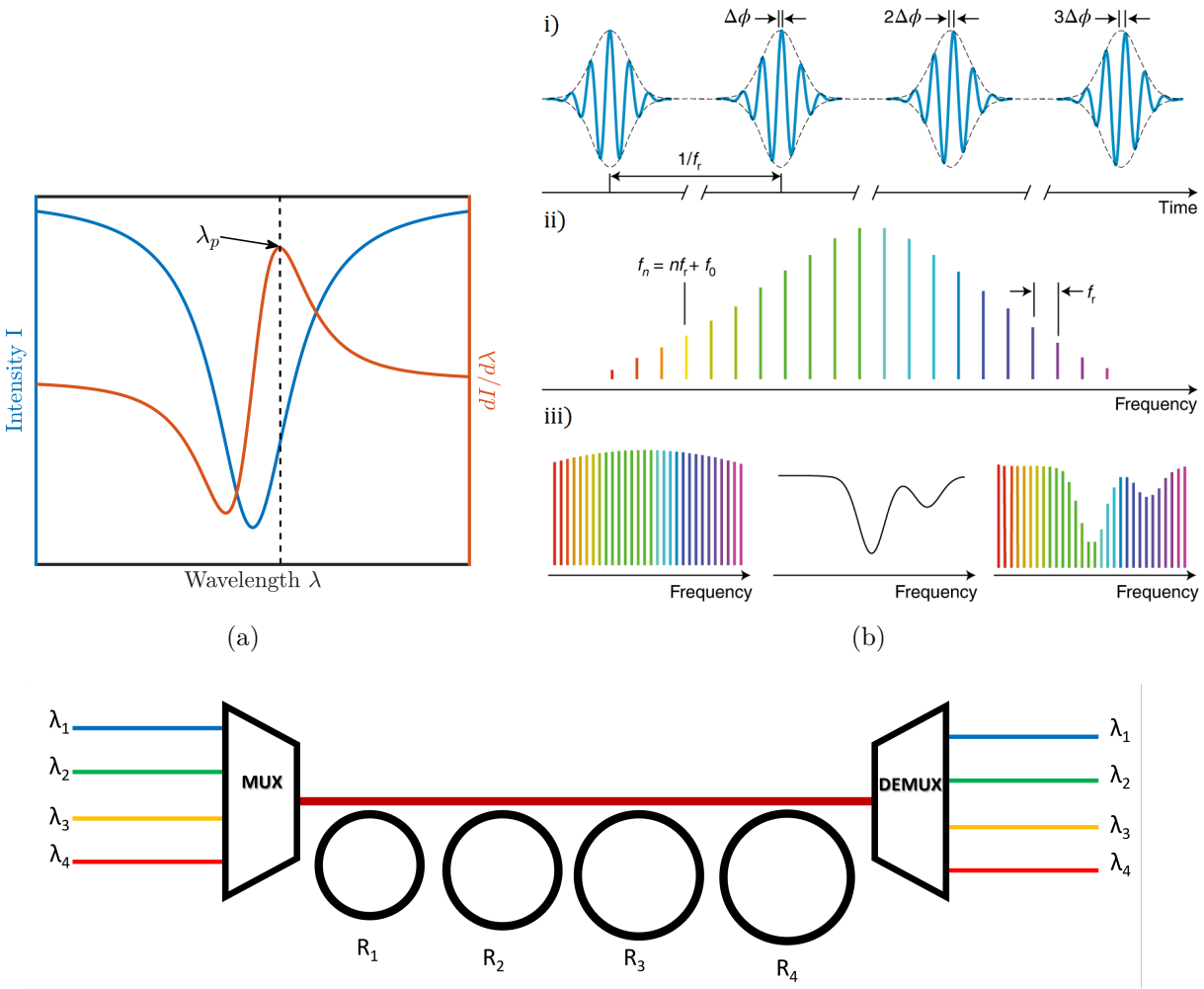



Figure 2.4 Optical signal interrogation: (a) Power detection method, (b) Principle of optical frequency combs i) time domain representation, ii) frequency domain representation, iii) interrogation of an optical signal using OFC [59],*reproduced with permission, Copyright 2019 Nature Photonics*, (c) Multiplexer-demultiplexer detection configuration of an array of microring resonators.

niques, E-O combs offer advantages in terms of integration with photonic devices [68]. E-O combs rely solely on the bandwidth of an RF source, providing greater flexibility in selecting the repetition rate. Additionally, E-O combs allow for precise control over comb parameters such as center frequency and amplitude flatness, which is not readily achievable with MLL and Kerr combs. However, the main drawback of the E-O generated combs is the amplification of the phase noise, which can be eliminated by the implementation of a feedback control loop on the RF generator [69].

## 2.5 Conclusion and Challenges

Optical microresonators offer an excellent replacement for piezoelectric transducers due to their performance and size properties. The Fabry-Perot offers tiny sensors with high sensitivity and the advantage of dense integration. However, the parallel sensing required for ULM acoustic imaging is challenging due to the need for an optical circulator and individual laser sources and detector for each sensor, making the system bulky and expensive. While the microring resonators offer an advantage in parallel sensing as it is compatible with the single input, single output configuration. However, state-of-the-art interrogation systems are still bulky and expensive. The polymer microring resonators are preferable over the silicon microresonators for their low-cost fabrication and their wide bandwidth. In contrast, silicon microresonators offer fewer fabrication variations and smaller sensors.

Because of working limitations in liquid environments for biomedical sensing, most of the published works use the near-infrared (NIR) band ($760nm \sim 780nm$) due to the lower water absorption at these wavelengths. However, the detection sensitivity of this band of wavelengths is limited due to the lack of appropriate/economic laser sources and optical amplifiers. [38]. Moreover, any contamination from the water medium may alter the ring's overall performance if it is present in the narrow gap between the MRR and the bus waveguide or on the MRR itself. Therefore, a cladding material should be considered regarding the acoustic impedance matching between the liquid medium and cladding. That impedance mismatching (if it exists) will reflect most of the acoustic wave and prevent it from reaching the MRRs sensing elements.

Notwithstanding these limitations, these considerations suggest using microring resonators for forming the array of ultrasound transducers; nonetheless, its relatively larger size is compatible with low acoustic frequency applications like ULM. The signal interrogation is proposed to be using the E-O combs techniques for its advantages in reducing the expense and the size of the overall interrogation system. However, considering the optical interrogation using E-O combs adds more constraints to the fabrication process to be performed with minimally acceptable uncertainties at critical dimensions of $50\,nm$, as the array of the polymer MRRs should have well-defined equal spectral spacing resonance wavelengths within a narrow optical bandwidth ($\Delta\lambda = 800fm$ to $125pm$), which is constrained by the available OFC generation bandwidth ($\Delta f = 100MHz$ to $15GHz$).

Moreover, to effectively interrogate the alteration in the resonance of each Micro-Ring Resonator (MRR), the spectral disparity between each resonance frequency must be equal to or greater than one full-width half-maximum (FWHM), a parameter predominantly governed by

the quality factor (Q). In summary, a higher Q value leads to improved signal interrogation and sensitivity, while parallel readout can be achieved by the optical frequency dual-comb.

# CHAPTER 3 THEORETICAL BACKGROUND

## 3.1 General

As we discussed in the previous chapter, we wish to investigate the design of an ultra-high Q optical microring array coupled to a single bus waveguide and interrogated using optical frequency combs. Before proceeding with the system design we need to investigate the theoretical background of the various parts of the system like the microring resonators, the ultrasound detection mechanism, the dual optical frequency combs, and the heterodyne detection mechanism.

## 3.2 Microring resonator

### 3.2.1 Optical wave propagation modes in microring resonator

Optical modes in a dielectric micro-ring resonator can be derived by solving Maxwell's equations in the cylindrical coordinates, described as

$$\begin{aligned} \nabla \times \vec{E} &= -\mu_0 \frac{\partial \vec{H}}{\partial t}, \quad \nabla \cdot (\epsilon_0 \epsilon_r \vec{E}) = 0 \\ \nabla \times \vec{H} &= \epsilon_0 \epsilon_r \frac{\partial \vec{E}}{\partial t}, \quad \nabla \cdot (\mu_0 \vec{H}) = 0 \end{aligned} \tag{3.1}$$

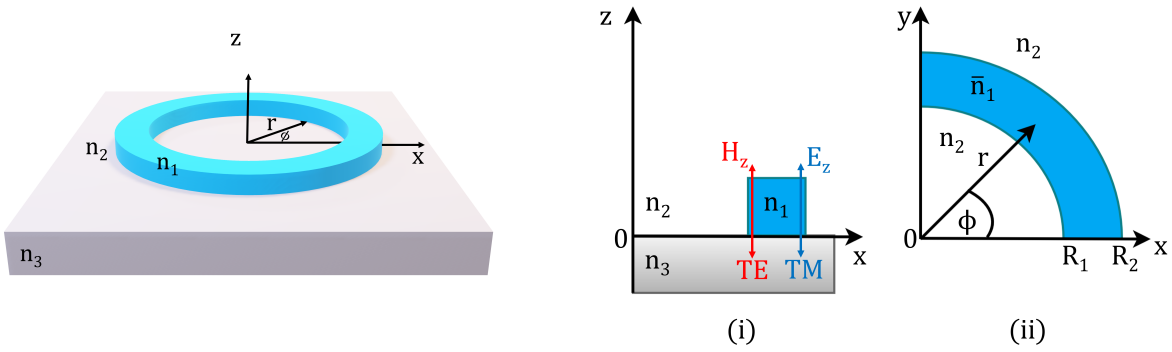
where $\epsilon_0$ is the permittivity of free space, $\epsilon_r$ is the relative permittivity of the medium (is related to the refractive index of the medium by $\epsilon_r = n^2$), and $\mu_0$ is the permeability of free space. The electric $\vec{E}$ and magnetic $\vec{H}$ fields in cylindrical coordinates are expressed by

$$\vec{E}(r, \phi, z, t) = E(r, \phi, z)e^{-i\omega t}, \quad \vec{H}(r, \phi, z, t) = H(r, \phi, z)e^{-i\omega t} \tag{3.2}$$

Consider a microring resonator that has inner and outer radii of $R_1$ and $R_2$. Considering the distribution of the index of refraction in $r - \phi$ plan, shown in figure 3.1a, the index of refraction is only a function of $r$ described as

$$n(r) = \begin{cases} n_1, & R_1 \leq r \leq R_2 \\ n_2, & r < R_1 \, and \, r > R_2 \end{cases} \tag{3.3}$$

The Helmholtz wave equation derived from Maxwell's equations for the WGM resonators in




(a) (b)

Figure 3.1 (a) Microring resonator in cylindrical coordinates, (b) equivalent 2D representation of the microring resonators in different coordinates indicating the TE and TM modes.

cylindrical coordinates is expressed as [70, 71]

$$\left[\frac{\partial^2}{\partial r^2}+\frac{1}{r}\frac{\partial}{\partial r}+\frac{1}{r^2}\frac{\partial^2}{\partial \phi^2}+k^2n^2(r)\right]F(r,\phi)=0 \tag{3.4}$$

where $k=\omega/c$ and $F(r,\phi)$ can be either $H_z$ in quasi-TE mode, or $E_z$ in quasi-TM mode, as shown in figure 3.1b. Applying the method of separation of variables to solve equation 3.4 and supposing that $F(r,\phi)=R(r)\Phi(\phi)$ leads to the following two equations

$$\frac{\partial^2 R}{\partial r^2}+\frac{1}{r}\frac{\partial R}{\partial r}+\left(k^2n^2(r)-\frac{m^2}{r^2}\right)R=0 \tag{3.5}$$

$$\frac{\partial^2 \Phi}{\partial \phi^2}+m^2\Phi=0 \tag{3.6}$$

The solution to equation 3.6 is subjected to a periodic boundary condition and can be expressed as $\Phi_m(\phi)=e^{\pm im\phi}$, where $m$ is an integer number representing the azimuthal number of the resonant mode.

The solution of equation 3.5 can be expressed as

$$R(r)=\begin{cases} C_1 I_m\left(n_2 kr\right), & r<R_1, \\ C_2 J_m\left(n_1 kr\right)+C_3 Y_m\left(n_1 kr\right), & R_1\le r\le R_2, \\ C_4 H_m^{(1)}\left(n_2 kr\right), & r>R_2, \end{cases} \tag{3.7}$$

Besides, the field continuity conditions must be applied at all the interfaces $r=R_1$ and $r=R_2$ such as: $R(r)$ must be continuous at all fields, $E_\phi \propto (1/n^2)dR/dr$ must be continuous

for TE-mode, and $H_\phi \propto dR/dr$ must be continuous for TM mode that yields finally to the characteristic equation of microring resonator as follows

$$\begin{aligned}&\frac{nI'_m(n_2kR_1)J_m(n_1kR_1) - I_m(n_2kR_1)J'_m(n_1kR_1)}{sH_m^{(1)}(n_2kR_2)J_m(n_1kR_2) - H_m^{(1)}(n_2kR_2)J'_m(n_1kR_2)}\\&= \frac{nI'_m(n_2kR_1)Y_m(n_1kR_1) - I_m(n_2kR_1)Y'_m(n_1kR_1)}{sH_m^{(1)'}(n_2kR_2)Y_m(n_1kR_2) - H_m^{(1)}(n_2kR_2)Y'_m(n_1kR_2)},\end{aligned} \tag{3.8}$$

where $n = n_1/n_2$ for TE modes and $n = n_2/n_1$ for TM modes. $J_m$ and $I_m$ are the Bessel function, modified Bessel function describing the propagation mode inside the ring resonator, while $Y_m$ and $H_m^{(1)}$ are Neumann function and Henkel function of the first type describing the leakage of the mode in the cladding.

### 3.2.2 Coupling of microring resonator with waveguide

The input and output electric fields (E1 and E3) in the bus waveguide, figure 3.2a, are related by coupled-mode equations with the circulating optical fields in the microring as follows:

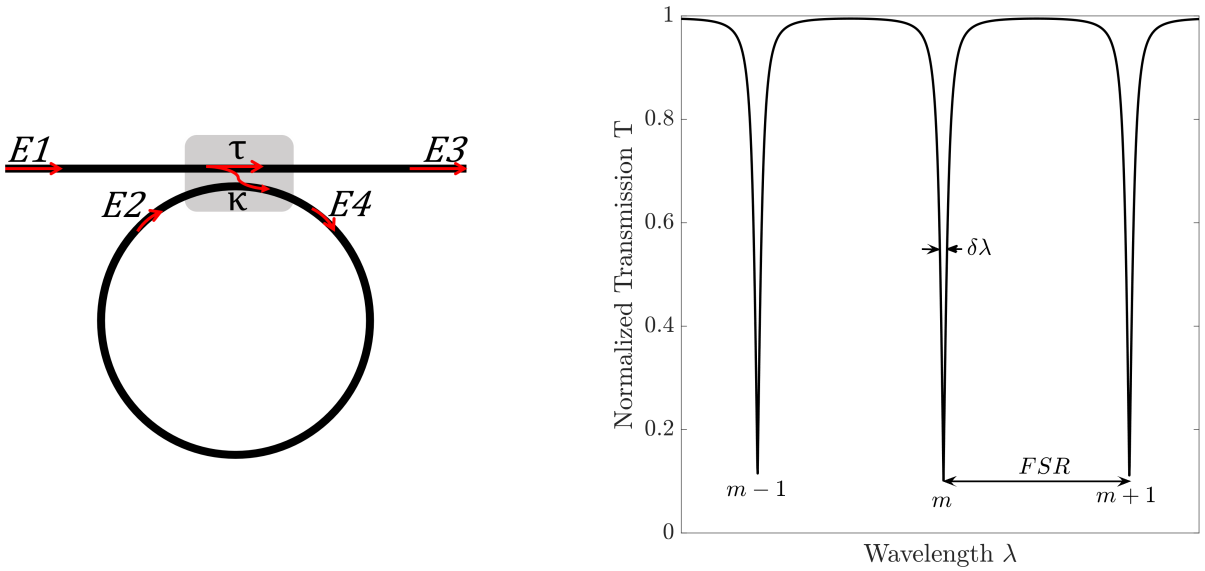
$$\begin{pmatrix}E_3\\E_4\end{pmatrix} = \alpha_i \begin{pmatrix}\tau & j\kappa\\ j\kappa & \tau\end{pmatrix}\begin{pmatrix}E_1\\E_2\end{pmatrix} \tag{3.9}$$

Where $\tau$ and $\kappa$ are the amplitude transmission and resonator-waveguide coupling ratios, respectively, and $\alpha_i$ is the insertion loss caused by a waveguide mode mismatch in the coupling region. The gap between the waveguide and the ring controls the coupling coefficient. In the microring waveguide, the circulating fields are related to each other by

$$E_2 = ae^{j\phi}E_4, \quad a = e^{-2\pi R\alpha}, \quad \phi = 2\pi n_{eff}L/\lambda \tag{3.10}$$

Where $a$ is the single-round amplitude transmission, $\phi$ is the single-round trip accumulated phase, $\alpha$ is the attenuation constant, $n_{eff}$ is the effective index of refraction of the ring resonator, $L = 2\pi R$ is the optical path length which is the circumference of the ring, $R$ is the ring radius, and $\lambda$ is the optical wavelength. The ratio between the transmitted to input optical intensity of the bus waveguide gives the transmission coefficient, figure 3.2b, as follows

$$T = \frac{I_t}{I_i} = \left|\frac{E_3}{E_1}\right|^2 = \alpha_i^2\frac{(\tau-\alpha_i a)^2 + 4\tau\alpha_i a\sin^2\frac{\phi}{2}}{(1-\tau\alpha_i a)^2 + 4\tau\alpha_i a\sin^2\frac{\phi}{2}} \tag{3.11}$$




(a) (b)

Figure 3.2 (a) Schematic drawing of a single microring resonator attached to a single waveguide showing the different electric fields and coupling parameters, (b) The normalized transmission spectrum of the single ring showing its resonance parameters.

### Coupling coefficient and gap dependence

The determination of gap separation ($g$) and hence coupling ratio ($|\kappa^2|$) is crucial for the design of the ultra-high quality factor microring resonator. One of the analytical techniques that give an overview of the coupling coefficient is the Marcatili method [72, 73]. Figure 3.3 shows an illustration of the geometrical parameters and the refractive index parameters that will be used in the calculation. Due to the curvature of the ring, the gap separation is variable and is given by the relation [52]

$$y(z) = g + R(1 - \cos(\theta)) \tag{3.12}$$

where $g$ is the minimum gap between the waveguide and the ring resonator, $R$ is the ring's outer radius, and $\theta$ is varying from $-\pi/2\, to\, \pi/2$.

As the TE mode has higher quality factors than TM modes, we will focus on the TE mode equations [74]. The localized coupling coefficient $C_{TE}(z)$ as a function of the z-axis for TE

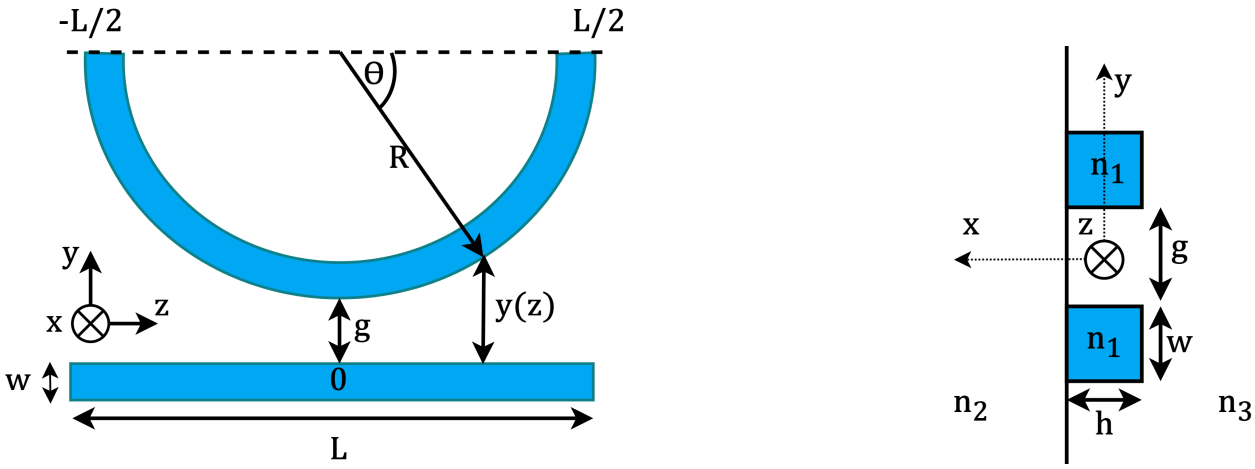



Figure 3.3 Illustration of coupling region between microring resonator and waveguide: (a) top view (y-z plane), (b) cross-section view at z=0 (y-x plane) [52].

mode as given by the Maracatili method is described by [72]

$$\begin{aligned} |C_{TE}(z)| =& 2\left(\frac{k_x A_3}{\pi}\right)^2 \frac{k_1}{k_z} \frac{\left(1-\left(\frac{n_3}{n_1}\right)^2\right)^{\frac{1}{2}}}{w} \\ & \times \left(1-\left(\frac{k_x A_3}{\pi}\right)^2\right)^{\frac{1}{2}} \exp\left[-\pi \frac{y(z)}{A_3}\left(1-\left(\frac{k_x A_3}{\pi}\right)^2\right)^{\frac{1}{2}}\right] \end{aligned} \tag{3.13}$$

The total coupling coefficient is then given by integrating equation 3.13 over the whole coupling length as follows

$$C_w = \int_{-\frac{L}{2}}^{\frac{L}{2}} C_{TE}(z)dz \tag{3.14}$$

Furthermore, the coupling ratio ($|\kappa^2|$) is calculated by the relation

$$\kappa^2 = 1 - (\cos(C_w))^2 \tag{3.15}$$

The parameters of the localized coupling coefficient, equation 3.13, are determined by the core waveguide cross-section dimensions width $w$ and height $h$, the propagation constants in all axial $k_z$ and transverse directions $k_x$ and $k_y$ which are related to the refractive indices of

the core and cladding. All of these parameters are described as follows [72]

$$\begin{cases} k_z = \left(k_1^2 - k_x^2 - k_y^2\right)^{\frac{1}{2}} \\ k_x = \frac{\pi}{w}\left(1 + \frac{2n_3^2 A_3}{\pi n_1^2 w}\right)^{-1} \\ k_y = \frac{\pi}{h}\left(1 + \frac{A_2 + A_3}{\pi h}\right)^{-1} \\ k_i = \frac{2\pi}{\lambda} n_i, \qquad i = 1, 2, 3 \\ A_i = \frac{\pi}{\left(k_1^2 - k_i^2\right)^{\frac{1}{2}}}, \qquad i = 2, 3 \end{cases} \tag{3.16}$$

Finally, the relationship between the coupling ratio and the quality factor is as follows [75]

$$Q = \frac{2Rn_{eff}\pi^2}{\lambda} \frac{\left(\sqrt{1 - |\kappa|^2}\right) \exp(-\alpha L/2)}{1 - (1 - |\kappa|^2) \exp(-\alpha L)} \tag{3.17}$$

### 3.2.3 Microring resonator cavity parameters

#### Resonance

Suppose a wideband laser source signal is input into a resonator-coupled waveguide. In that case, there are output intensity resonance dips (output intensity is minimum) that occur in the transmission spectrum when the phase accumulation of the round trip equals multiple of $2\pi$. These dips represent the resonance wavelength $\lambda_r$ of the WGM resonator, figure 3.2b, that depends mainly on the geometry and waveguide optical parameters and can be given as [71]

$$m\lambda_r = 2\pi R\, n_{eff}(\lambda_r, R) \tag{3.18}$$

where $m$ is the azimuth mode number.

#### Quality factor

The total quality factor $Q_t$ of the MRR is determined by two main components, the intrinsic quality factor $Q_i$ and the coupling quality factor $Q_c$ as follows

$$\frac{1}{Q_t} = \frac{1}{Q_i} + \frac{1}{Q_c} = \frac{1}{Q_r} + \frac{1}{Q_s} + \frac{1}{Q_a} + \frac{1}{Q_c}, \tag{3.19}$$

$$Q_i = \frac{4\pi^2 R n_{eff}}{|2 \ln a| \lambda_r} \tag{3.20}$$

The intrinsic quality factor is affected by various optical loss mechanisms in the cavity such as scattering loss, radiation loss, and material absorption loss, where $Q_s$ is the quality factor due

to the scattering loss, $Q_a$ is the quality factor due to material absorption loss, and $Q_r$ is the quality factor due to radiation loss which can be obtained by solving the eigenvalue problem of the microring resonator and extraction of the complex eigenfrequency $Q_r = R(\omega)/2I(\omega)$.

**Free Spectral Range**

The free spectral range defines the wavelength separation between two consecutive resonance modes, figure3.2b, and is given as

$$FSR = \frac{\lambda_r^2}{2\pi R n_g} \tag{3.21}$$

where $n_g$ is defined as the group index inside the ring resonator and can be expressed as a function of effective RI and wavelength as follows

$$n_g(\lambda) = n_{eff}(\lambda) - \lambda \frac{dn_{eff}}{d\lambda} \tag{3.22}$$

**Photon life time**

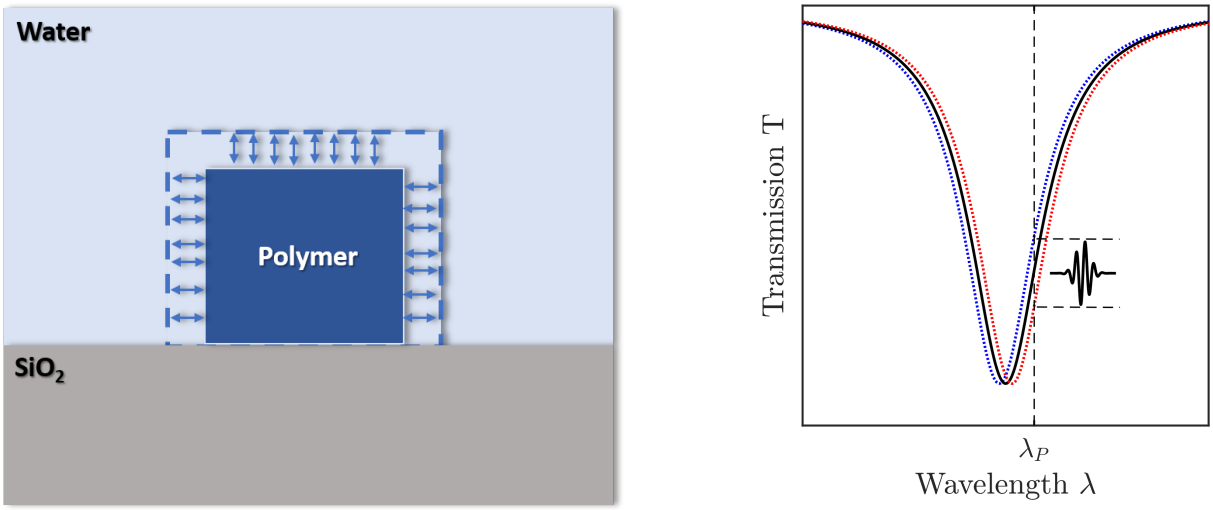
For any kind of WGM resonator, the energy inside the resonator is gradually accumulated until a steady state is reached. The time required to reach the steady state is called the effective photon lifetime and is given by

$$\tau_p = \frac{Q}{\omega} \tag{3.23}$$

This timescale sets the characteristic response time of the resonator and has to be sufficiently shorter than the half-cycle duration of the US field in order to provide the time resolution of the US field through the transmission change of the cavity resonance.

## 3.3 Ultrasonic detection mechanism

The microring responds to the US waves in two manners. First, the ring waveguide is deformed by acoustic pressure that changes the shape and optical field distribution. This deformation of the waveguide is remarkable in elastic materials having low Young's moduli such as polymers [32], figure 3.4a. Second, the optical RI of the material itself is perturbed with a strain induced by acoustic pressure linked to elasto-optic effect in the material [76]. Taking into consideration the elasto-optic effect, the refractive indices of the two main x and




(a) (b)

Figure 3.4 (a) Waveguide response to US waves (arrows indicate compression/stretching of the dimensions of the polymer under the application of US excitation), (b) Ultrasonic signal extraction of US-induced modulation of intensity transmission by measuring optical resonance shift.

y polarizations are expressed as [48]

$$\begin{aligned} n_x &\approx n_o - C_1\sigma_x - C_2(\sigma_y + \sigma_z) \\ n_y &\approx n_o - C_1\sigma_y - C_2(\sigma_z + \sigma_x) \end{aligned} \tag{3.24}$$

where $n_o$ is the stress free refractive index, $(C_1, C_2)$ are the elastooptic constants, and $(\sigma_x, \sigma_y, \sigma_z)$ are the stress in the $(x, y, z)$ directions. Both of these changes affect the shift of the resonant wavelength, in the same way, making them beneficial for US detection via transmission/reflection tracking of the resonator. As shown in figure 3.4b, the interrogation wavelength $\lambda_p$ is chosen at one of the side maximum transmission slopes around $\lambda_r$. When the US perturbation occurs, a time-dependent detectable shift in $\lambda_r$ can be measured and is given by [77]

$$\frac{\Delta\lambda_r}{\lambda_r} = \frac{\Delta l}{l} + \frac{\Delta n}{n} \tag{3.25}$$

### 3.3.1 Sensitivity

The sensitivity of the US sensor is given by the change of optical transmission $T$ resulting from the applied acoustic pressure amplitude $P$ and is given by [48, 78]

$$S = \frac{dT}{dP} = \frac{dn_{eff}}{dP}\frac{d\lambda_r}{dn_{eff}}\frac{dT}{d\lambda_r} \tag{3.26}$$

The first term $dn_{eff}/dP$ represents the change of the refractive index in the polymer waveguide induced by applied pressure considering factors such as Young's modulus, the elasto-optic coefficients of the polymer, and the waveguide's cross-sectional shape. $dT/d\lambda_r$ is the change in transmission associated with $\lambda_r$ that can be defined as the slope of linear region obtained at the rising or falling edge of the resonance dip, which can be approximated as linearly proportional to the quality factor Q and $d\lambda_r/dn_{eff}$ is the shift in $\lambda_r$ to the change of the effective RI that can be given as [32]

$$\frac{d\lambda_r}{dn_{eff}} = \frac{2\pi R}{m} = \frac{\lambda_r}{n_{eff}} \tag{3.27}$$

The detected signal's sensitivity depends on Q and the waveguide design parameter defined by the material's properties and the guided mode profile.

### 3.3.2 Acoustic parameters

**Acoustic angular sensitivity $D(\theta)$**

As we introduced in section 2.2.2, the size of the sensor and the ultrasound wavelength determines the angular sensitivity of the sensor. Based on the ring piston shape derivation, the angular sensitivity is defined by a Bessel function of the first order and is expressed as [79]

$$D(\theta) = J_0(KR\sin\theta) \tag{3.28}$$

where $K$ is the acoustic wavenumber, and $R$ is the ring radius.

**Geometry limited cut-off frequency $f_t$**

The acoustic bandwidth is limited by the thickness of the sensor with the formula [48]

$$f_t = \frac{\nu}{2h} \tag{3.29}$$

where $\nu$ is the acoustic wave speed, and $h$ is the sensor thickness.

**Resonance limited cut-off frequency** $f_{cut}$

It is related to the effective photon lifetime inside the optical cavity. In order to keep measuring a pressure signal due to the ultrasound, the microring resonator needs to reach the resonance steady state after instantaneous ultrasound disturbance to be ready for the next measurement. This acoustic cut-off frequency is given by [80]

$$f_{cut} = \frac{1}{\tau_p} = \frac{\omega}{Q} \tag{3.30}$$

Where $\tau_p$ is the effective photon lifetime, described by equation 3.23, $\omega$ is the optical angular frequency.

## 3.4 Optical frequency combs

### 3.4.1 Theory

Let us consider an electrooptic phase modulator of $\pi$ optical phase shift voltage of $V_\pi$; a CW laser feeds that at an optical frequency $f_o$ and electric field amplitude of $E_o$. The modulator is electrically driven by a sinusoidal waveform using an RF signal generator at a frequency $f_m$. The voltage is given by $[V(t) = V_o \sin(2\pi f_m t)]$ where $V_o$ is the peak voltage. At the modulator's output, the optical field experiences a phase shift $[\Delta\varphi = \pi V(t)/V_\pi = \phi_0 \sin(\omega_m t)]$, that controls the output optical field $E(t)$ in the time domain [81],

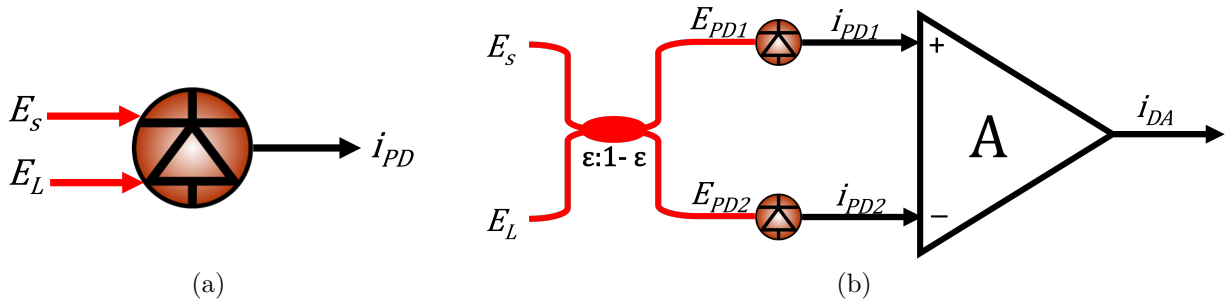
$$E_m(t) = E_0 e^{i\omega_0 t} e^{i\Delta\varphi} = E_0 e^{i\omega_0 t} e^{i\phi_0 \sin(\omega_m t)} \tag{3.31}$$

The frequency domain representation is given by Fourier transformation as follows,

$$\tilde{E}(\omega) = \mathrm{FT}(E(t)) = E_0 \delta(\omega - \omega_0) * \left( \int_{-\infty}^{\infty} e^{i\phi_0 \sin(\omega_m t)} e^{-i\omega t} \mathrm{d}t \right). \tag{3.32}$$

Using the Jacobi–Anger expansion, the phase-modulated optical signal can be expressed as

$$\begin{aligned} \tilde{E}(\omega) &= E_0 \delta(\omega - \omega_0) * \left( \int_{-\infty}^{\infty} \sum_{p=-\infty}^{\infty} J_p(\phi_0) e^{i(p\omega_m - \omega)t} \mathrm{d}t \right) \\ &= E_0 \sum_{p=-\infty}^{\infty} J_p(\phi_0) \delta(\omega_0 + p\omega_m), \end{aligned} \tag{3.33}$$




(a) (b)

Figure 3.5 (a) Frequency beating interference between a local oscillator and signal electric fields on a single photodiode (b) Frequency beating interference between a local oscillator and signal electric fields on a beam splitter with ratio $\varepsilon : 1 - \varepsilon$ detected by balanced heterodyne configuration. Red: optical signal, black: electrical signal

### 3.4.2 Balanced heterodyne detection

Balanced heterodyne detection is a highly effective method employed to detect weak signals at the quantum limit. It involves the combination of a weak input signal and a strong local oscillator signal within an optical beam splitter/combiner, resulting in a signal that is directly proportional to the product of the two signals' amplitudes. The resulting signal's frequency is a combination of sums and differences between the frequencies contained in the weak signal and the local oscillator signal. This technique is of great significance due to its ability to amplify signal amplitudes through multiplication, without the need for optical amplification, and its capability to suppress noise through balanced detection [82–84].

let us consider the electric field component of two optical signals. The first one is representing the signal branch $E_s$, while the other is representing local oscillator $E_L$, figure 3.5a. Before proceeding with the balanced heterodyne detection configuration, we will investigate first the frequency-beating interference resultant components of these two signals on a single photodetector. The two reference and local oscillator electric fields can be expressed as

$$\begin{aligned} E_s(t) &= E_{s0} \cdot e^{i\omega_s t} \\ E_L(t) &= E_{L0} \cdot e^{-i\omega_L t} \end{aligned} \tag{3.34}$$

The photodiode current is responding to the optical signal intensity that is related to the product of the sum of the electric field signals and their complex conjugate as follows [85]

$$I = \left(E_{s0} \cdot e^{i\omega_s t} + E_{L0} \cdot e^{-i\omega_L t}\right) \cdot \left(E_{s0} \cdot e^{-i\omega_s t} + E_{L0} \cdot e^{i\omega_L t}\right) \tag{3.35}$$

The simplified mathematical representation of the optical intensity at the photodiode is

expressed as

$$I = E_{s0}^2 + E_{L0}^2 + E_{s0}E_{L0}\cos\left(\omega_s + \omega_L\right)t + E_{s0}E_{L0}\cos\left(\omega_s - \omega_L\right)t \tag{3.36}$$

Due to the photodiode's limited bandwidth, it responds only to the resultant DC component and the beating frequency components with the $\Re$ transfer function

$$i_{PD} = \Re\left\{E_{s0}^2 + E_{L0}^2 + E_{s0}E_{L0}\cos\left(\omega_s + \omega_L\right)t + E_{s0}E_{L0}\cos\left(\omega_s - \omega_L\right)t\right\} + n_o(t) \tag{3.37}$$

where $n_0(t)$ represents the noise function in the output current.

Moving to the heterodyne detection, if we consider that the two electric fields, described before in equation 3.34, are combined with $2 \times 2$ optical beam splitter with a splitting ratio $\varepsilon : 1 - \varepsilon$ to generating two complementary signals at the output branch, figure 3.5b. The total input intensity on each of the photodiodes is expressed as

$$\begin{aligned} I_{PD1} &= \left(\sqrt{1-\varepsilon}E_{s0}\cdot e^{i\omega_s t} + \sqrt{\varepsilon}E_{L0}\cdot e^{-i\omega_L t}\right)\cdot\left(\sqrt{1-\varepsilon}E_{s0}\cdot e^{-i\omega_s t} + \sqrt{\varepsilon}E_{L0}\cdot e^{i\omega_L t}\right) \\ I_{PD2} &= \left(\sqrt{\varepsilon}E_{s0}\cdot e^{-i\omega_s t} + \sqrt{1-\varepsilon}E_{L0}\cdot e^{i\omega_L t}\right)\cdot\left(\sqrt{\varepsilon}E_{s0}\cdot e^{i\omega_s t} + \sqrt{1-\varepsilon}E_{L0}\cdot e^{-i\omega_L t}\right) \end{aligned} \tag{3.38}$$

Applying the photodiode responses, $\Re_1, \Re_2$, in equation 3.37, introduced before, then the photodiode currents are then expressed as taking into consideration

$$\begin{aligned} i_{PD1} &= \Re_1\left\{(1-\varepsilon)E_{s0}^2 + \varepsilon E_{L0}^2 + \sqrt{1-\varepsilon}\sqrt{\varepsilon}E_{s0}E_{L0}\cos\left(\omega_s - \omega_L\right)t\right\} + n_{o1}(t) \\ i_{PD2} &= \Re_2\left\{\varepsilon E_{s0}^2 + (1-\varepsilon)E_{L0}^2 - \sqrt{1-\varepsilon}\sqrt{\varepsilon}E_{s0}E_{L0}\cos\left(\omega_s - \omega_L\right)t\right\} + n_{o2}(t) \end{aligned} \tag{3.39}$$

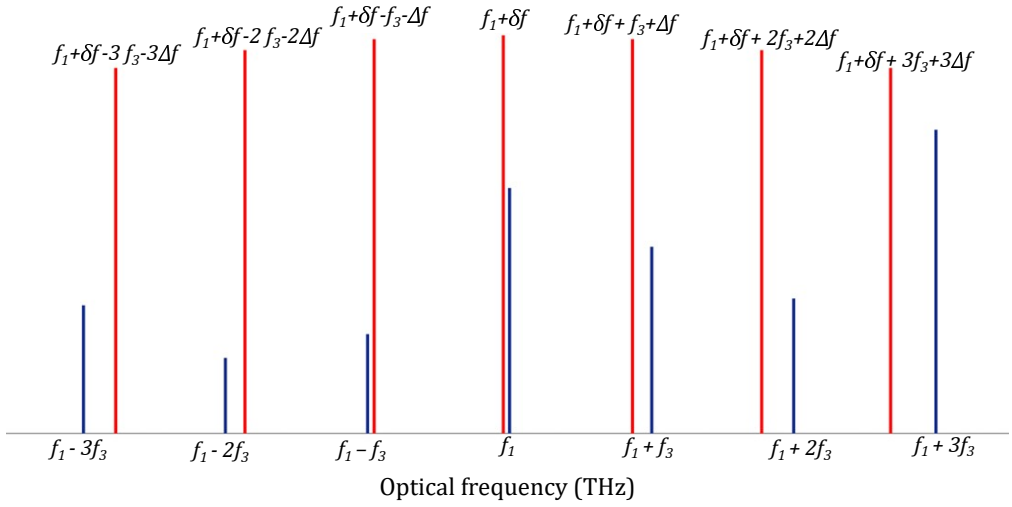
Finally, the two currents are differentially amplified with an amplifier gain of $A$, so the final output current of the heterodyne detection configuration is defined as

$$\begin{aligned} i_{DA} = i_{PD1} - i_{PD2} = A\{&\left[(1-\varepsilon)\Re_1 - \varepsilon\Re_2\right]E_{s0}^2 + \left[\varepsilon\Re_1 - (1-\varepsilon)\Re_2\right]E_{L0}^2 \\ &+ \left(\Re_1 + \Re_2\right)\sqrt{1-\varepsilon}\sqrt{\varepsilon}E_{s0}E_{L0}\cos\left(\omega_s - \omega_L\right)t\} + \left(n_{o1}(t) - n_{o2}(t)\right) \end{aligned} \tag{3.40}$$

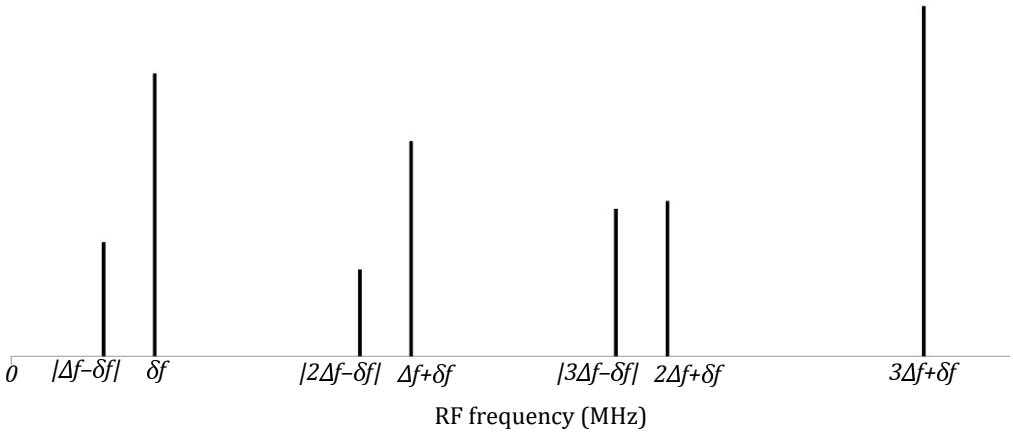
Considering the case that the two photodetectors are identical and the splitting ratio in the optical beam splitter is $0.5 : 0.5$, then equation 3.40 can be reduced to

$$i_{DA} = A\Re E_{s0}E_{L0}\cos\left(\omega_s - \omega_L\right)t + \left\{n_{o1}(t) - n_{o2}(t)\right\} \tag{3.41}$$

Following the same introduced sequence, if we consider having two comb modes that have the central frequencies that are slightly shifted in frequency by $\Delta f$, and the sideband frequencies are shifted by $\delta f$. These shifts allow for parallel signal interrogation by using dual optical




(a)




(b)

Figure 3.6 (a) Optical frequency domain of optical dual-combs, red: local oscillator comb, blue: signal interrogation comb (b) RF domain down-converted beat frequencies between every two nearest pair of the dual-comb lines.

frequency combs that introduce simultaneous signal capturing from all the rings. The first comb is considered the signal branch while the other is the reference signal (or the local oscillator), then the real term of equation 3.33 for both combs considering that we have an odd number of combs (P+1) is

$$\begin{aligned}\tilde{E}_1(t) &= E_{01} \sum_{p=-P/2}^{P/2} J_p(\phi_{01}) \cos((\omega_1 + p\omega_{m1})t), \\ \tilde{E}_2(t) &= E_{02} \sum_{p=-P/2}^{P/2} J_p(\phi_{02}) \cos((\omega_2 + p\omega_{m2})t).\end{aligned} \tag{3.42}$$

Finally, the output current of the differential amplifier with gain $A$ due to the heterodyne detection configuration as described before is given by

$$\begin{aligned} i_{DA} &= A\Re E_{01}E_{02}\sum_{p=-N/2}^{N/2} J_p(\phi_{01})J_p(\phi_{02})\cos((\omega_1 + p\omega_{m1} - \omega_2 - p\omega_{m2})t) \\ &= A\Re E_{01}E_{02}\sum_{p=-N/2}^{N/2} J_p(\phi_{01})J_p(\phi_{02})\cos(2\pi|p\Delta f \pm \delta f|t) \end{aligned} \tag{3.43}$$

## 3.5 Conclusion

In this chapter, we have provided a comprehensive theoretical breakdown of the different components incorporated in our system's design and experimental setup. We have presented an overview of the theory and design principles associated with microring resonators, covering key elements and characterization parameters. Additionally, we have explored the theory underlying ultrasound detection utilizing microring resonators, taking into account the angular and acoustic limitations, as well as sensitivity parameters. Furthermore, we have introduced the theory of optical frequency combs (OFCs) and the detection scheme of balanced heterodyne, which works as a fundamental component of our parallel interrogation setup. These theoretical overviews have equipped us with the necessary knowledge to advance toward the subsequent phase of our research, which involves the detailed design and simulation, where the careful selection and exploration of parameters will be undertaken in greater depth.

# CHAPTER 4 DESIGN AND SIMULATION

## 4.1 General

As discussed in the preceding chapters, the primary objective of this project is to develop a polymer microring resonator array capable of simultaneously detecting ultrafast ultrasound echo signal information across all rings with high sensitivity. Figure 4.1 illustrates the system design, where blood microvessels are exposed to an external ultrasound planewave source. The ultrasonic echo from the tissue modulates the transmitted light through each spectrally distinct resonator, taking advantage of the light-sound interaction. The 2D array is made of identical linear array branches. Each linear array branch is interrogated with an equally power-split input optical signal through optical fibers and is coupled to an individual photodiode for signal detection. This design facilitates an independent and symmetric array design; hence, only a linear array design is introduced in this work that can be replicated afterward to generate the 2D array.

The signal interrogation will be done using a dual optical frequency comb that introduces simultaneous signal capturing from all the rings. Dual-comb detection configuration allows a spectral response of the ring array to be measured on a comb-by-comb basis rapidly and without any systematic limitations of conventional techniques [26]. As in figure 4.2a, let us consider five-ring resonators with different radii ($R_1, R_2, R_3, R_4, R_5$), each exhibiting transmission spectra. The conventional approach for US signal interrogation from a single ring resonator is the power detection method [86]. In this technique, an optical probing wavelength is adjusted at one of the quasi-linear parts around the resonance wavelength. The shift in the spectrum due to the ultrasound perturbation causes variation in the laser power amplitude that can be detected. However, in the case of an array of microring resonators, simultaneous signal interrogation necessitates the availability of an array of optical wavelengths. This requirement can be fulfilled by utilizing optical frequency combs, which generate a set of frequency-equidistant single-mode lasers that are capable of operating simultaneously.

As shown in figure 4.2b, two coherent laser beams that have slightly different optical frequencies ($f_1, f_1 + \delta f$) are fed into two separate identical electro-optic phase modulators (EOMs). EOMs are driven by two RF signals that have a slight frequency shift ($f_3, f_3 + \Delta f$) and are generated by a two-tone phase-stabilized RF generator. One of these two combs will act as a reference signal (we could name it a local oscillator), while the other will be used for signal interrogation of the ring array configuration. To detect the variation in the optical signal due to the ultrasound perturbation, a balanced heterodyne detection scheme is used. In this

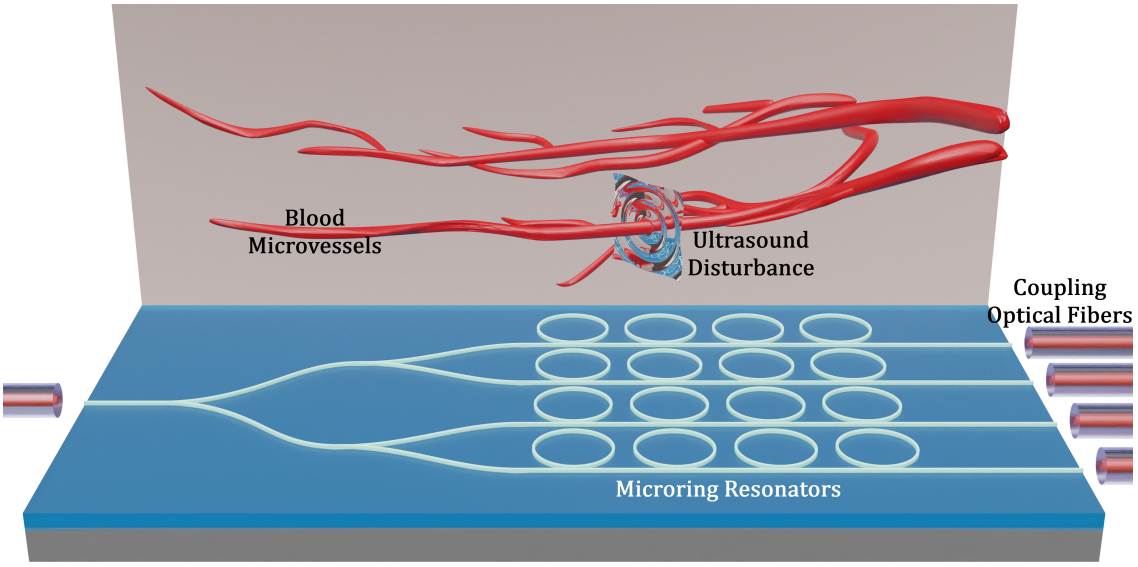



Figure 4.1 Schematic of the proposed US detection setup. US disturbance (echo from e.g. blood microvessels) is detected via a 2D array of optical microring resonators.

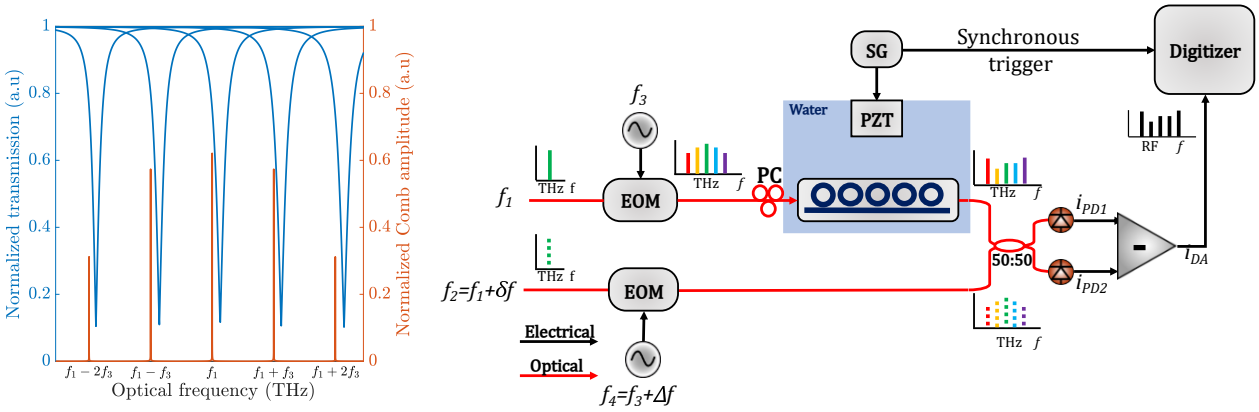



Figure 4.2 (a) example of a five-ring spectrum and OFC for power detection method, (b) Schematic of dual-comb interrogation experimental setup of microresonator linear array. OFC: optical frequency comb, EOM: electro-optic modulator, UST: ultrasound transducer, SG: signal generator, PC: polarization controller

technique, the interrogated signal is mixed with the reference signal (acts as a local oscillator) through a (50:50) fiber beam splitter/combiner. Then, the two photodiode currents are differentially amplified to minimize random errors. This scheme provides a strong amplified signal at the beat frequency between each interrogation comb and its corresponding reference comb. Besides, this detection scheme down-converts the signal from optical frequencies into a combination of the main design RF frequencies $(\Delta f, \delta f)$, which can be acquired easily using

common electronics.

The design process begins by considering the selection of the rings' array design and corresponding parameters, with a particular focus on exploring the anticipated sensitivity to US signals. The ensuing investigation leads to the determination of parameters for the optical frequency dual-combs. Finally, a thorough signal analysis is conducted, utilizing simultaneous simulated US signals across the entire array, enabling the extraction of individual ring signal.

## 4.2 Design and modeling of Microring array

### 4.2.1 Material Overview

We use a C-band tunable laser source and electro-optic modulators around 1550 nm, rather than the 780 nm commonly used for underwater applications, which enables the use of a variety of commercial electro-optic modulators in this band. Using this optical wavelength band leads to a challenge because of water absorption, which we circumvent with a thin layer of PDMS as a top cladding of the fabricated polymer waveguide. The bottom cladding material is a $5\mu m$ silicon wet thermal oxide layer which guarantees minimal propagation loss in the waveguide. The utilization of a PDMS top thin layer offers several advantages. Firstly, PDMS serves as a cladding material for the waveguide, enabling the propagation of C-band laser light without significant water absorption. Secondly, PDMS exhibits a RI of approximately 1.39 [99], which closely matches the RI of silicon oxide ($\approx$ 1.444) [30]. This close match facilitates near-symmetric optical mode confinement within the waveguide. Thirdly, PDMS acts as a barrier, preventing water contaminants from filling the gap between the ring and the waveguide, which may alter the quality factor of the system. Lastly, the acoustic impedance of PDMS matches that of water, effectively minimizing acoustic reflection losses [100].

Polymer material is chosen as a core material for its lower cost, simple fabrication, and elastic properties. We have two candidate polymer materials: SU-8 and Polystyrene. SU-8 is an epoxy-based, with eight epoxy groups, negative photoresist that was designed mainly for micromachining and microelectronics applications that required thick, high-aspect ratio, and stable material [90, 101]. SU-8 is sensitive to both ultraviolet and electron beams, making it suitable for direct writing fabrication, besides its suitability for nanoimprinting. Additionally, it has excellent optical properties, and high chemical, thermal, and mechanical stability after exposure and post-exposure bake [102]. The cross-linked SU-8 films are also known for their good resistance to acids, bases, and solvents. SU-8 was used as a primary material in

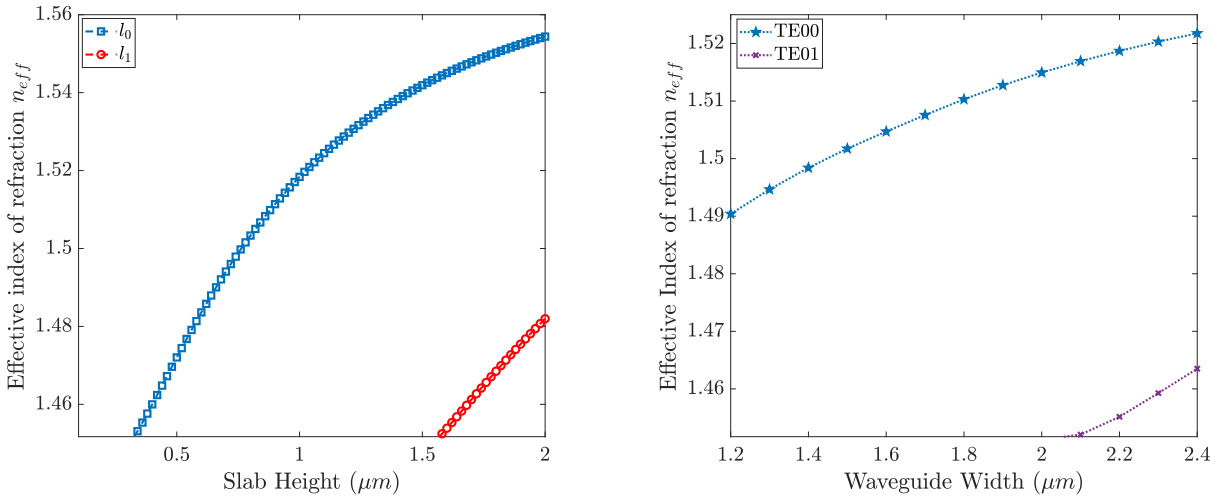



Figure 4.3 (a) 1D mode extraction of slab waveguide configuration using TMT method, (b) 2D mode extraction by beam propagation solvers.

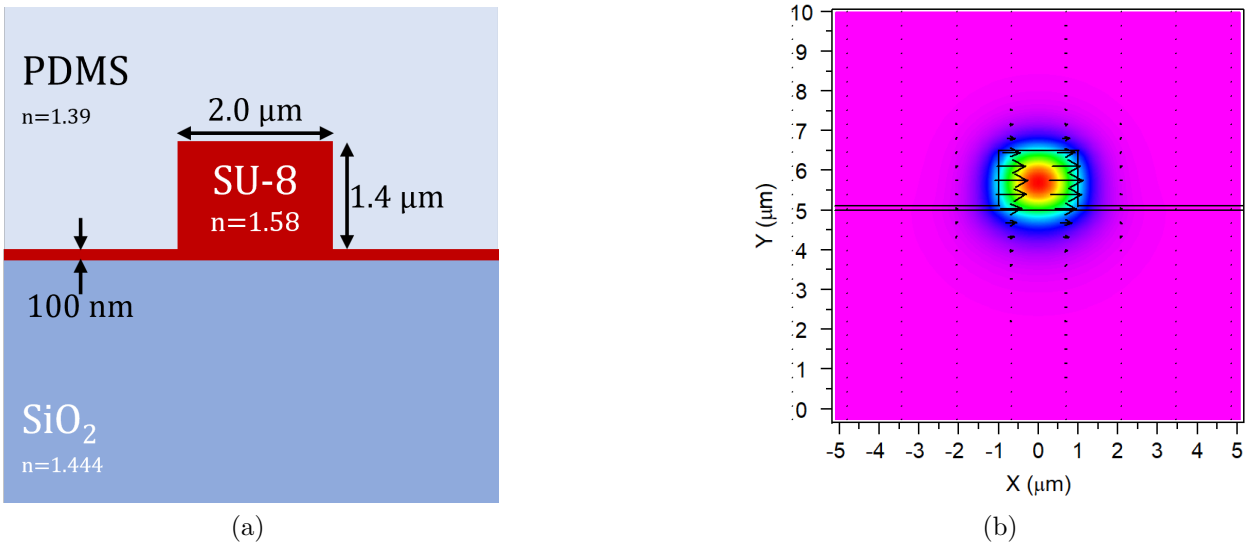



Figure 4.4 (a) Proposed waveguide cross-section, (b) TE propagation mode profile ($E_x$). Arrow: Electric field direction.

optical-based ultrasound sensors [32, 103].

Polystyrene, on the other hand, is more elastic than SU-8, so it is more sensitive to ultrasound disturbances and has also excellent optical properties in the c-band. However, it is insensitive to UV exposure or electron beam, so it can only be fabricated with nanoimprinting. Polystyrene was also used extensively in optical-based ultrasound sensors [29, 48, 50].

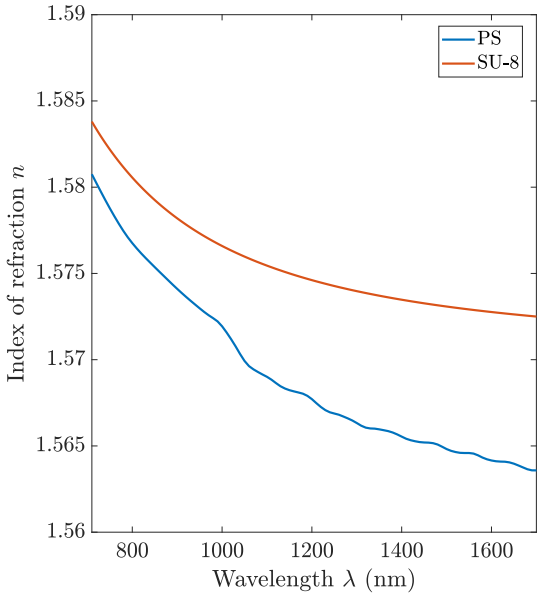



Figure 4.5 Dispersion curve of SU-8 [87] and Polystyrene [88] for IR band,

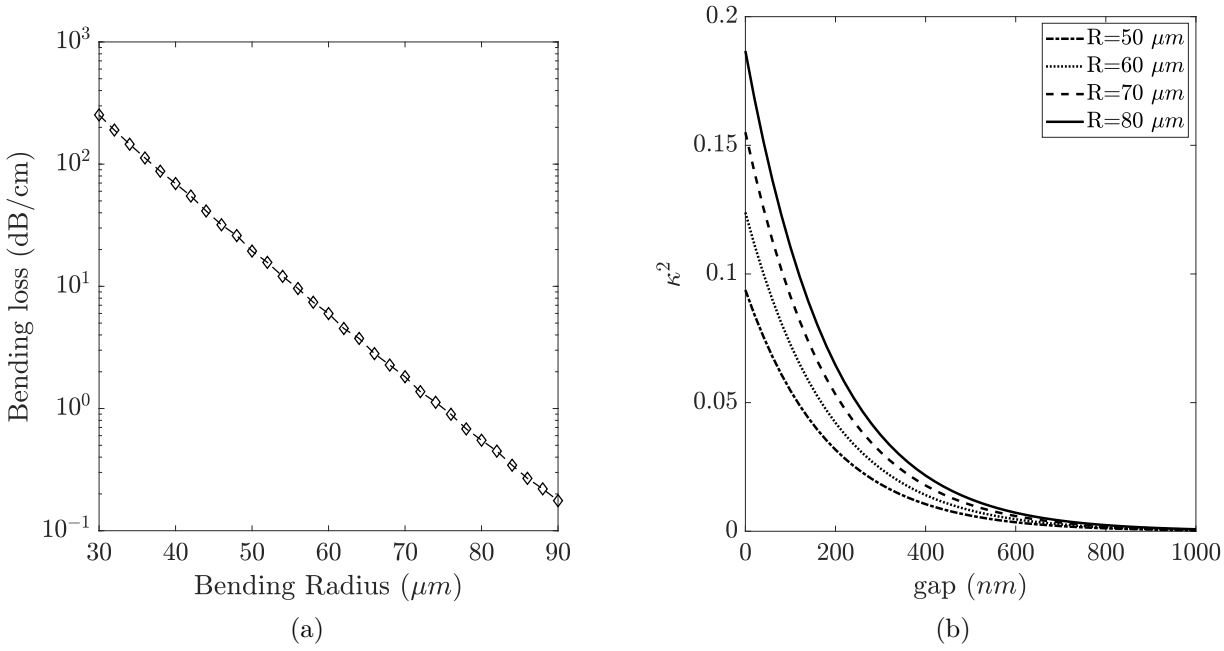



Figure 4.6 (a) Bending loss with various ring resonator radii, (b) Coupling coefficient $\kappa^2$ at different ring radii,

The mechanical and optical properties of SU-8 and PS are listed in table 4.1. The dispersion curves of both SU-8 and Polystyrene are shown in figure 4.5, illustrating that both materials

Table 4.1 Material properties of Polystyrene and SU-8 polymers

| Property | SU-8 | Polystyrene |
|---|---|---|
| Young Modulus $E(GPa)$ | $3.48 - 4.95$ [89–92] | 0.3 [93, 94] |
| Poisson ratio $\nu$ | 0.22 [95] | 0.33 [93] |
| First Elasto-optic coefficient $C_1$ | $30.07 \pm 1.49 \times 10^{-12}$ [96] | $^{*}48 \pm 3 \times 10^{-12}$ [93] |
| Second Elasto-optic coefficient $C_2$ | N/A | $^{*}29 \pm 3 \times 10^{-12}$ [93] |
| Glass transition temperature $T_g(^{\circ}C)$ | 60 [97] | 100 [98] |
| RI ($@\lambda = 1550nm$) $n$ | 1.577 | 1.565 |

$^{*}$ at $\lambda = 632.8nm$

have approximately the same index of refraction at the working wavelength. To sum up, PS is the best candidate for US sensitivity due to its lower young modulus by a factor of ten, while SU-8 is better from the fabrication point of view as it has a lower glass transition temperature, high mechanical and chemical stability after curing, and can survive in the latter packaging processes like dicing. In addition, the lake of elasto-optic coefficients of SU-8 makes the acoustic simulation of SU-8 unreliable. In that manner, for acoustic simulation purposes, we are going to take PS as the device material, while later in the fabrication process, SU-8 will be the device material supported by the fact that the change in the refractive indices of both materials is $< 0.8\%$ making no major difference in the optical simulations and the radii choice.

### 4.2.2 Waveguide and Microring resonator design

From an acoustic point of view, the microring resonator is modeled as a ring-shaped piston where the induced pressure response is correlated to the cross-section of the ring. The larger the cross-section the better the sensitivity but at the expense of the bandwidth that we previously described in equation 3.29. Optically, the cross-section of the ring, which is the same as the waveguide, controls the supported optical propagation modes within the waveguide, so the design of our bus waveguide primarily relies on single-mode operation, which is recommended over multimode operation for several reasons. Firstly, in single-mode operation, only a single resonant frequency is excited, resulting in a sharper and narrower resonance peak. This characteristic enhances the accuracy of detection and simplifies the subsequent analysis. Conversely, in multimode operation, the simultaneous excitation of multiple resonant frequencies leads to overlapping resonance peaks and potential interferences. Consequently, the resulting spectrum becomes less clear and more complex, posing challenges in discerning and analyzing the response to ultrasonic perturbations. Secondly, single-mode operation of-

fers a higher sensitivity to US perturbations compared to multimode operation. This larger sensitivity arises from the focused excitation at a specific resonant frequency, facilitating a more efficient coupling of US-induced changes to the optical properties of the resonator.

With the help of Matlab solvers using the Transfer Matrix Method (TMT), the solution of the propagation equation for TE-mode in slab waveguide was performed to determine the boundary thickness of single-mode operation for 1550nm. Figure 4.3a represents the first and second TE modes as a function of SU-8 slab height. It is found that $1.5\,\mu m$ thick waveguide is valid for the single-mode operation that is also suitable for higher US sensitivity. Calculation of the 2D mode profile with beam propagation solvers versus the change of waveguide width that gives the single mode cutoff width to be $2.05\,\mu m$, as shown in figure 4.3b, for the same wavelength. In that manner, the proposed design waveguide cross-section is a rectangle of $1.4\mu m \times 2.0\mu m$, shown in figure 4.4a, and guarantees single-mode operation at the working wavelength taking into consideration a thin $100nm$ residual layer of SU-8 arising from the proposed nanoimprinting fabrication technique. The extracted TE mode of the proposed waveguide is shown in figure 4.4b, which will be the main mode of propagation in all of the next simulations.

The microring resonator cross-section will have the same width and height as the bus waveguide. Due to the low contrast between the core polymer and cladding material ($\approx 0.14$), the optical mode spreads in the cladding material. Besides, the bending loss limits the use of small-radius ring resonators. Figure 4.6a, shows the bending loss as a function of the ring radii that limit the minimum radius to be $60\mu m$ that corresponds to a bending loss of $0.05\,dB/m$. While a larger radius is limited by the central acoustic frequency $f_{acous}$, as the imaging resolution is limited to half of the acoustic wavelength. As we are aiming for higher penetration imaging, low acoustic frequencies up to $8MHz$ will be used ($\lambda/2 = 187.5\mu m$). This sets the upper limit of ring radii in our design to $80\mu m$ taking into consideration the prevention of optical cross-talk between the MRRs [104]. The coupling coefficient of the ring with the waveguide is also studied, as calculated from equation 3.15. As seen in figure 4.6b, the coupling coefficient varies for different ring radii at the same gap separation between the waveguide and the bus waveguide, so the determination of optimum gap separation will be done on a ring-by-ring basis after the determination of the optimum radii in the array. The coupling coefficient $|\kappa^2|$ is to be chosen for critical coupling condition taking into consideration equation 3.17, to reach high quality factors.

### 4.2.3 Microring array

For optimum detection of an acoustic perturbation described before, the spacing between the MRRs' centers should be kept as small as possible, below one acoustic wavelength $\lambda_a$, to achieve a high filling factor [105]. In addition, the angular sensitivity of the MRR sensors is dependent on the radius as discussed in section 3.3.2. The design and modeling of the MRR array should go through two steps. The first step is to use an extracted 2D RI of the waveguide at different bending radii and sweep all our possible ring radii using equation 3.18. We should be able to get an array of MRR that has equally spaced resonance frequencies of $\approx 10 - 12GHz$ optical spectral spacing, which is $80 - 100pm$ in optical wavelength, due to the limited 3dB bandwidth of commercial EOMs.

### 4.2.4 Ring radii choice

The effective RI of the waveguide optical mode is affected by the bending of the waveguide and the wavelength dispersion. Using the finite element method (FEM), the 2D effective refractive index of the rings for TE mode for the ring radii was extracted as a function of both the bending radius and the wavelength dispersion as shown in figure 4.7a. Before choosing the right radii for the array, the ring radius should follow the resonator resonance condition, described by equation 3.18. Figure 4.7b shows a scattering of the ring radii that follows the resonance condition for a particular arbitrary integer azimuthal index $m$. As we introduced before, we use each comb laser mode and assign it to one of the side slopes for each microring resonator's spectrum. This condition challenged the choice of the ring resonances to have equal spectral spacing by $\Delta f_2$ and a high-quality factor that guarantees at least a resonance bandwidth of $\Delta f_2/2$. In addition, the optical resonance 3dB bandwidth (FWHM) should be smaller than half of the frequency spacing between the comb lines, i.e., (FWHM$\leq f_m/2$), to comply with the power detection method limitations [86]. Reducing FWHM requires achieving high-quality factor (Q) resonances that can be achieved by reaching the critical mode coupling condition along with controlling the surface roughness in nanoimprinting mold fabrication [17, 30, 38, 50, 106, 107].

Considering the resonance condition (equation 3.18), there are multiple dependent variables that we need to choose carefully to achieve these resonances. A Matlab algorithm was used to optimize all the parameters in the resonance equation to extract the ring radii that have the exact spectral spacing in the resonance frequencies. Table 4.2 gives an example of 5 rings with a $\approx 9.4GHz$ resonance spectral spacing taking into account the fabrication process limitation ($50nm$ critical dimensions) of the nanoimprinting mold while using the electron beam lithography technique. Given the small marginal variance in the radii of the extracted

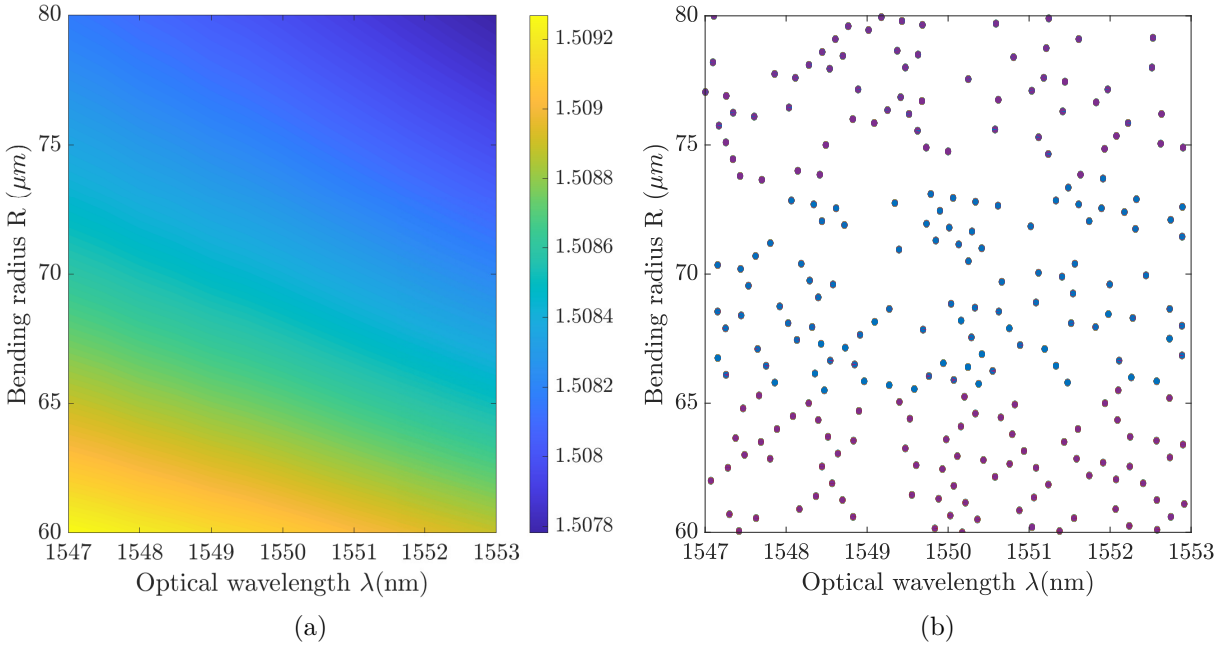



Figure 4.7 (a) Extracted effective index of the polymer waveguide at different bending radii using RSoft Femsim. Color Bar: effective refractive index of the waveguide, (b) Scattering of the ring radii following the resonance condition for arbitrary azimuth index m.

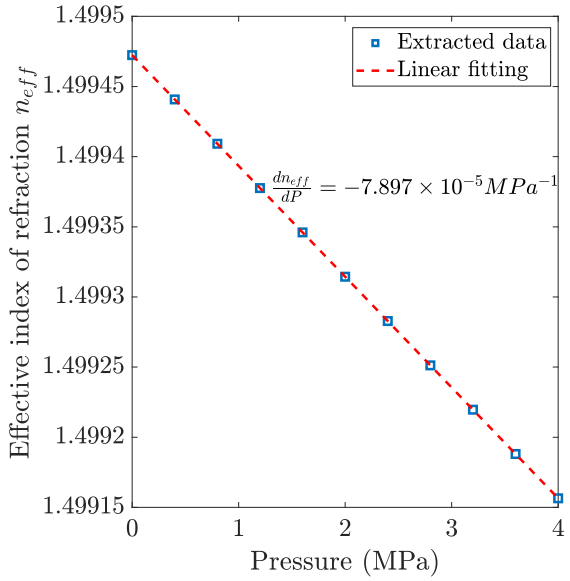
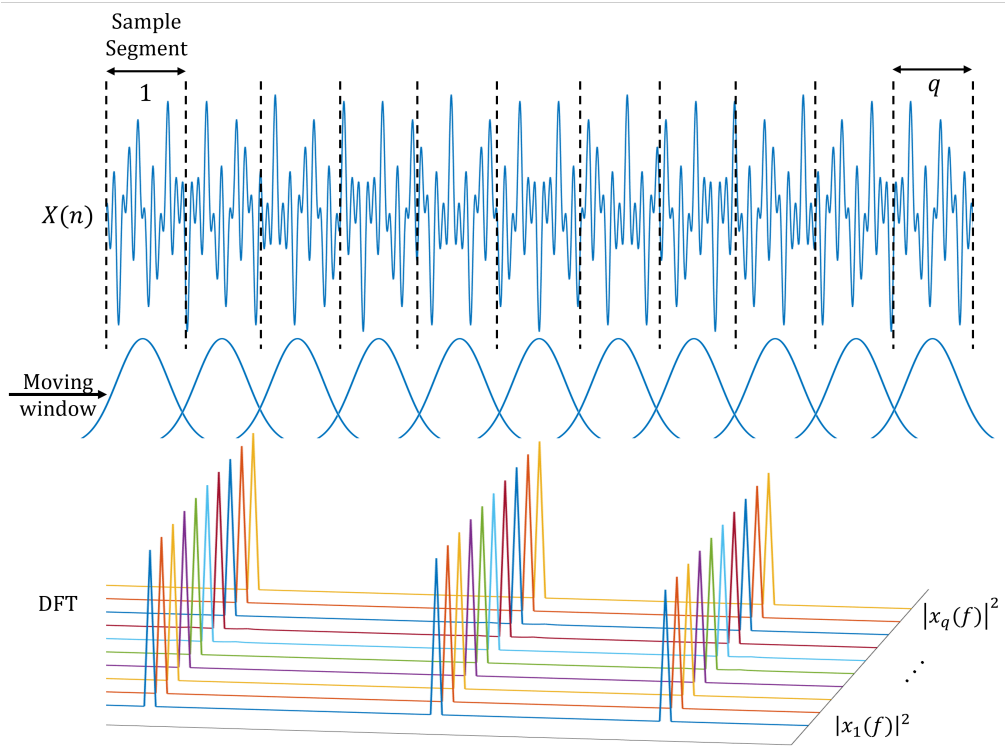


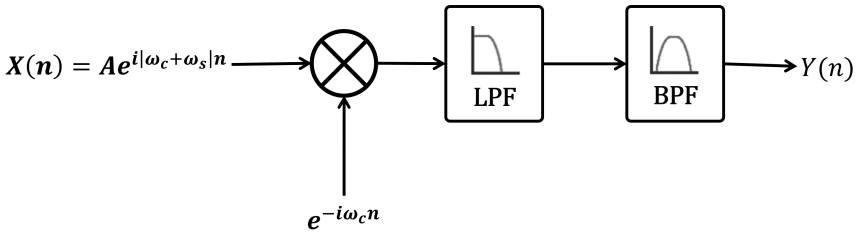

Figure 4.8 Extracted effective refractive index for TE mode when exposed to ultrasound pressure.

Table 4.2 Matlab script results of five rings' radii following the detection criterion

| R ($\mu m$) | Azimuthal index m | Resonance Frequency ($THz$) | $\Delta f$ ($GHz$) |
|---|---|---|---|
| 70.50 | 431 | 193.5194268 | |
| 71.15 | 435 | 193.5288987 | 9.43 |
| 71.80 | 439 | 193.5383687 | 9.47 |
| 72.45 | 443 | 193.5478021 | 9.43 |
| 73.10 | 447 | 193.5571883 | 9.39 |




(a)




(b)

Figure 4.9 (a) short-time Fourier transform (STFT) technique, (b) Down-conversion to base-band technique

rings, we can use the median radius value to determine the quality factor parameters and calculate the optimized gap. The value of the absorption loss can be taken from the literature which has the dominant effect on the quality factor, so $\alpha = 4-5dB/cm$ [108] for the proposed material can be substituted in equation 3.20 to get the intrinsic quality factor, which results in $Q_i = 5.3 - 6.63 \times 10^4$. Applying now the quality factor equation 3.17, the critical coupling coefficient $|\kappa^2| = 0.0193 - 0.026$ corresponds to a separation gap of $g = 400 - 445\,nm$.

To have an overview of the sensor sensitivity described in equation 3.26, the first two terms can be either simulated or calculated to estimate the sensitivity. COMSOL multi-physics simulation is used to extract the first term $dn_{eff}/dP$ by measuring the effective index of refraction for various applied mechanical pressure representing the US perturbation. Figure 4.8 shows the extracted data and the linear fit that gives this term to be $dn_{eff}/dP = -7.897 \times 10^{-5} MPa^{-1}$. As per the second term $d\lambda_r/dn_{eff}$, it can be derived from the resonance equation and is given by $2\pi R/m = \lambda_r/n_{eff} \approx 1.032\mu m$, for the first ring as an example. So with the current design parameters, the spectral sensitivity is calculated as $d\lambda_r/dP = (-79 \times 10^{-6} MPa^{-1}) \times (1.032\mu m) \approx -81.53 pm/MPa$. Finally, $dT/d\lambda_r$, the change in transmission associated with $\lambda_r$, can be defined as the slope of the linear region obtained at the rising or falling edge of the resonance dip, which is proportional to the quality factor.

### 4.3 Optical dual frequency comb parameters

The electro-optic modulators can be adjusted based on the exact spacing between the ring resonators and within their bandwidth. As shown in table 4.2, the average spectral spacing between the rings' resonances is 9.43 GHz which defines $f_m$. Figure 4.10a shows five optical frequency combs that work as probing frequencies for the five microring array resonators showing the simulated US disturbances $G_p(t)$ on each ring. The difference between the undisturbed amplitudes of the combs is controlled through $V_\pi$ property of the EOM by a Bessel function of the first kind $J_p$ with different orders. Adjusting $V_\pi$ controls the amount of optical power that is transferred from the central frequency to the sideband frequencies.

As outlined in section 3.4.1, following the process of down-converting optical frequencies using a dual-comb setup, radio frequency (RF) combs are produced through the frequency beating of adjacent optical combs from both the probing comb and the local oscillator comb. Each down-converted RF frequency retains the acoustic signal information from its corresponding original optical comb, allowing us to treat them as carrier frequencies for further analysis and processing.

These carrier frequencies are related to the combination of $\Delta f, \delta f$ which are to be chosen to be 90 MHz and 20 MHz respectively, that provide an electrical frequency spacing of at least 40 MHz between combs in the RF space. $\delta f$ is constrained by the operating frequency of the AOM, while $\Delta f$ is tuned to prevent overlap between the detected acoustic signals and potential interference with the harmonic frequencies of the $\delta f$. In that manner, the first five RF carrier frequencies corresponding to these parameters are 20 MHz, 70 MHz, 110 MHz, 160 MHz, and 200 MHz. The photodiodes within the balanced heterodyne detection scheme are chosen to have a detection bandwidth of 500 MHz, and a sampling rate of $1GS/s$ is offered by the digitizer. Figure 4.11a investigates the simulated time-domain signal of the down-converted carrier frequencies as acquired by the digitizer. The analysis of the dual-comb down-converted signal is performed using two different signal analysis techniques: short-time Fourier transform (STFT) [109] and down-conversion to baseband [110]. In the STFT method, as shown in figure 4.9a, the acquired time-domain sampled signal is divided into segments by a moving Gaussian temporal window function defined by segment length and segments' overlap. The discreet Fourier transform (DFT) is calculated for each segment individually and is accumulated over the vector length. The change of the frequency amplitude in the accumulated DFT returns the carried ultrasound signal at each down-sampled carrier frequency. This technique is straightforward, but the segment length controls both the resolution of the frequency vector and the sampling rate of the carried acoustic signal.

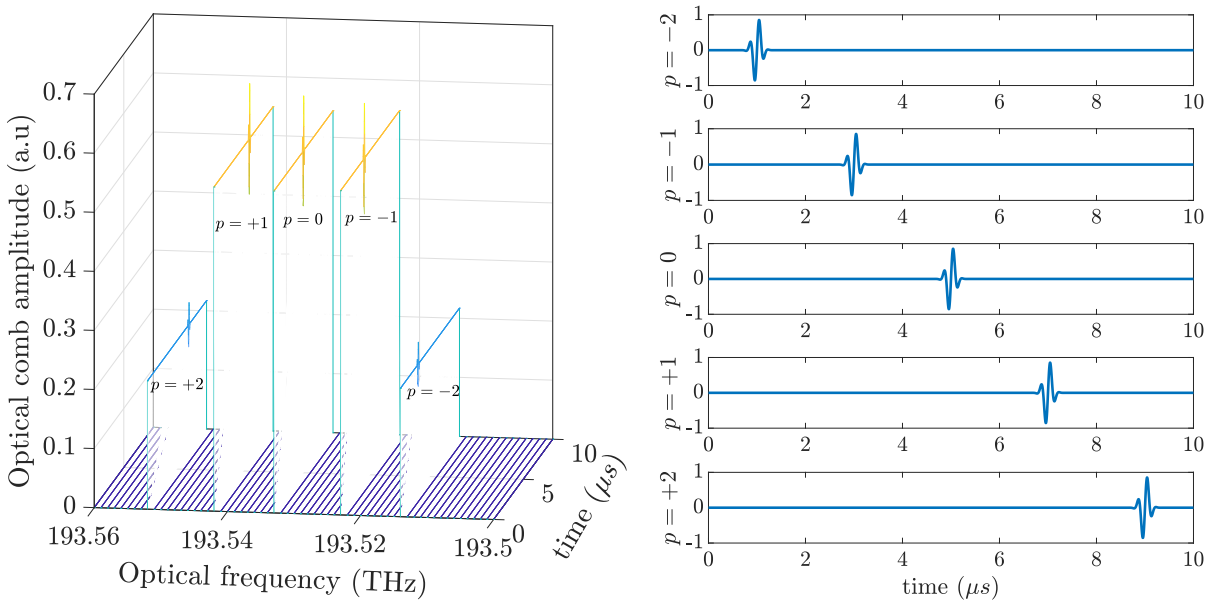
On the other hand, in the down-conversion to baseband method, shown in figure 4.9b, the acquired time-domain sampled signal is shifted every time by $e^{-i2\pi|p\Delta f \pm \delta f|t}$ with different $p$, so each time a different comb tooth with index $p$ is centered at zero frequency. Analysis of one comb tooth with index $p = 0$ is being introduced and it is the same analysis technique for the rest of the comb teeth. Then, the shifted voltage signal is expressed as

$$v_{DA}(t) = C\, G_0(t) J_0(\phi_{01}) J_0(\phi_{02}) \; + C \sum_{p=-N}^{N, N\neq 0} G_p(t) J_p(\phi_{01}) J_p(\phi_{02}) \cos\left(2\pi|p\Delta f \pm 2\delta f|t\right) \quad (4.1)$$

where $C$ is a constant combining the constant terms including the load resistance $R$. Applying low pass (LP) filter, set to match the acoustic bandwidth, will remove the higher frequency terms which are given by the summation term in equation 4.1. The acoustic signal $\tilde{G}_0(t)$ of this carrier frequency can then be expressed as

$$\tilde{G}_0(t) = \frac{\tilde{v_{DA}}(t)}{C\, J_0(\phi_{01}) J_0(\phi_{02})} \quad (4.2)$$

Where $\tilde{v_{DA}}(t)$ is the filtered measured signal. A bandpass (BP) filter can be used to narrow the detection acoustic bandwidth and eliminate the noise. Careful design of these frequency




(a) (b)

Figure 4.10 (a) Five OFCs probe the US disturbance signal from the microring resonator array, (b) Representation of the simulated US pulses assigned to each ring resonator.

filters is considered to avoid ringing and transient effects.

If we considered the same simulated time domain signal shown in figure 4.11a similar to the signal that should by measured by the digitizer, and its Fourier transform 4.11b, then we apply the described STFT method as follows. A Hann window with a time interval of $100\,ns$, exactly 100 samples, is chosen to provide enough signal samples for a stable STFT spectrum along with $10\,ns$ overlap region. Each window interval will give a single point on the ultrasound response spectrum for each of the carrier frequencies. The $100\,ns$ window interval also constrains the ultrasound bandwidth frequency by the Nyquist condition to 5 MHz, and the frequency resolution in the frequency domain to 10 MHz. The DFT signals for each carrier individually and its spline fit are shown in figure 4.12a.

Applying the down-conversion to the baseband method, we extracted each US disturbance signal from its corresponding carrier frequency by shifting the whole frequency spectrum to the baseband of each carrier frequency. The signal is then extracted by applying a Butterworth low pass filter with order 5 and bandwidth of 15 MHz. A bandpass IIR filter is used to reduce any noise coming from any sources out of the acoustic transmitter bandwidth. The bandwidth is as narrow as the ultrasound transducers, which is in the range of $\pm 2$ MHz. The

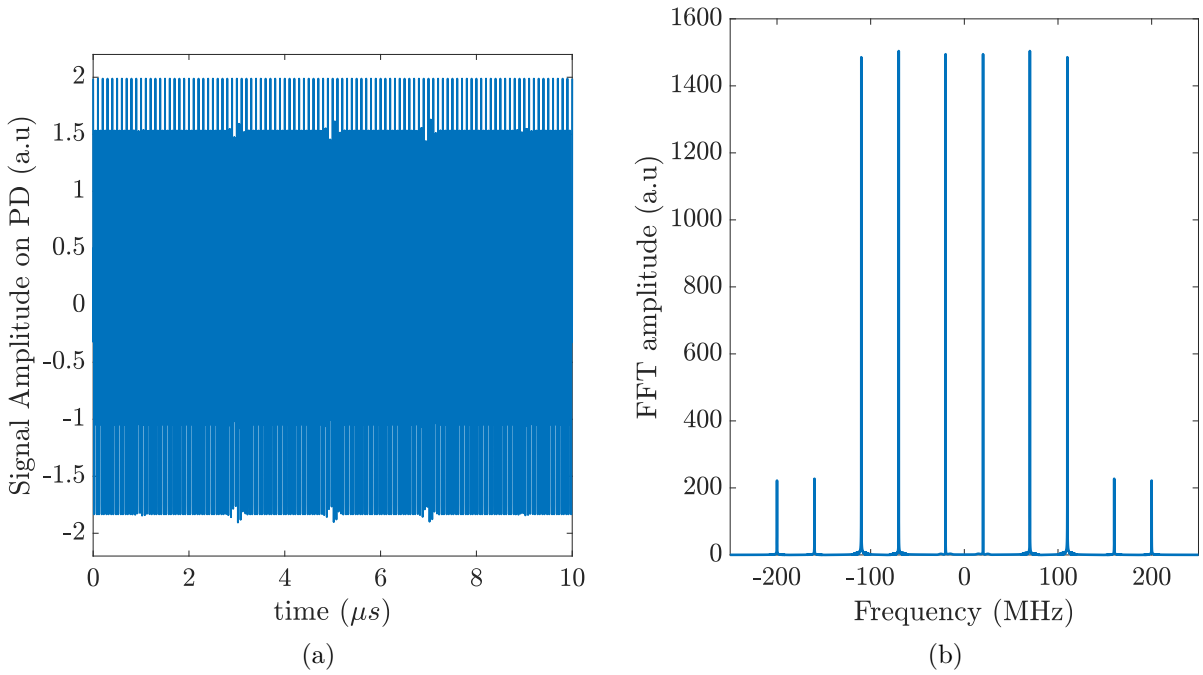
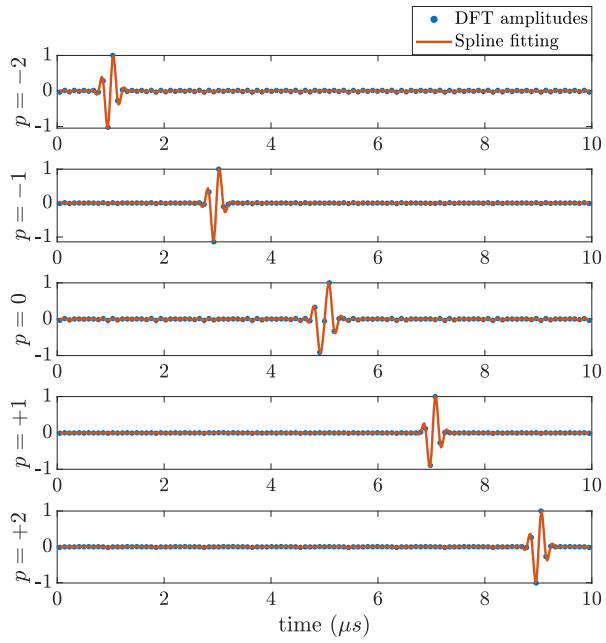



Figure 4.11 (a) Time-domain simulated signal out of the heterodyne detection, (b) Fourier transform representation of the simulated signal.

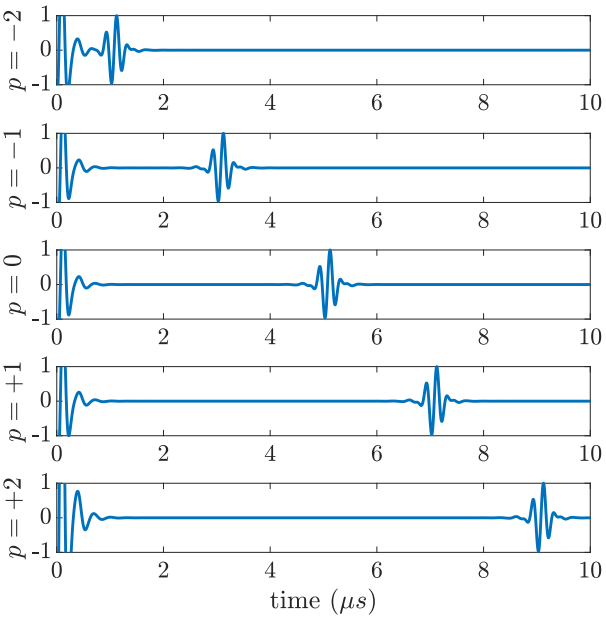
filtered signal is shown in figure 4.12b, showing the effect of the transients of the filter at the signal beginning, but it can be avoided as it is in the very beginning of the signal vector away from our effective measurements. However, the signal is still detectable, and there is no limitation on the detected ultrasound frequency except for the sampling limitations.

## 4.4 Conclusion

In conclusion, we investigated in this chapter the main design aspects of our system starting from the primary elements and components. We investigated the design and simulation of a single microring resonator and its key properties, including the expected sensitivity to US, that match the proposed design criteria and the choice of the ring array parameters. A careful choice of both the ring radii and the frequency comb parameters was introduced to comply with the power detection method of the array simultaneously. Finally, a simulated signal was introduced similar to the expected measured signal, and analyzed with two different signal processing techniques that lead to parallel signal detection. In the subsequent chapter, we are investigating the fabrication process, the experimental techniques for optical and ultrasound characterization, and a detailed experimental setup for the dual OFC.




(a)




(b)

Figure 4.12 (a) The amplitudes of carrier signals after DFT calculation from STFT method and the corresponding spline fit, (b) The filtered signal from all the carrier frequencies after applying down-conversion to baseband method.

# CHAPTER 5 FABRICATION PROCESS AND EXPERIMENTAL METHODOLOGY

## 5.1 General

In this chapter, we describe the detailed fabrication process of the designed polymer MRRs array that will be carried out in a cleanroom facility through a developed microfabrication process. We are also going to investigate the post-fabrication steps, such as dicing, optical fiber coupling, and optical resonance characterization setup. Fabricated samples are carefully packaged and affixed to coupling optical fibers, preparing them for underwater ultrasound characterization. Finally, we construct and utilize a signal interrogation setup based on the optical frequency combs for parallel sampling the ultrasound signal response from the MRRs array.

## 5.2 Fabrication process

As discussed in section 2.3.2, two main fabrication techniques are used for the polymer MRRs array; direct exposure and nanoimprinting. For the direct exposure, we chose electron beam lithography (EBL) instead of UV lithography for its superior resolution advantages despite its cost and long writing times. While in the nanoimprinting technique, we used the soft nanoimprinting technique [111]. In this technique, a hard mold is fabricated once with the required design, and then a soft mold, usually made of PDMS, can be reproduced using the same hard mold. In addition, the soft mold can be used a few times before it is discarded and replaced. In addition, in this approach, only a hotplate is needed to complete the fabrication process. Consequently, this approach offers significant cost reduction in the fabrication process eliminating the need for a conventional nanoimprinting machine. Moreover, the soft nanoimprinting technique is compatible with various types of polymers, regardless of their sensitivity to UV radiation or electron beam exposure.

The characterization of the fabricated devices is crucial in each critical step for assessing the process. Starting with the silicon mold, we aim to evaluate the quality of the etching process, including the etch rate and surface roughness. Profilometry is used to investigate the thickness and depth of the defined structures, followed by scanning electron microscopy (SEM) to provide more details on the measured parameters. After peeling the PDMS soft mold, other characterization steps are required to ensure that the pattern is transferred successfully to the polymer layer. Optical microscopy can be used to give a general overview, followed by

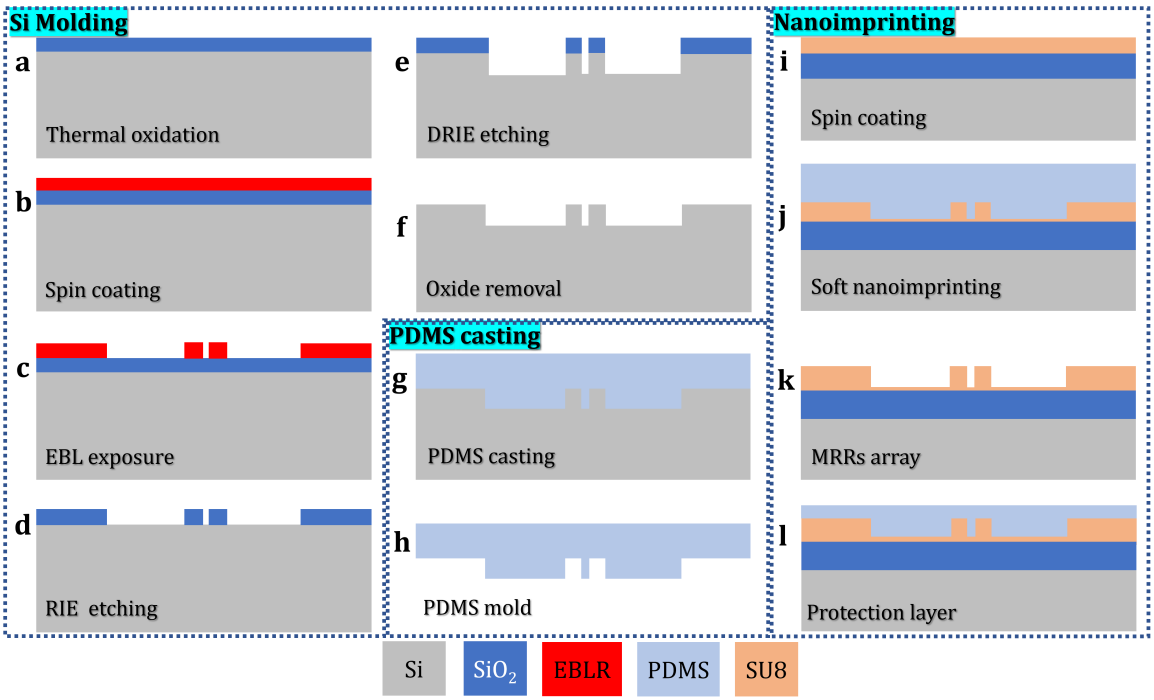



Figure 5.1 MRRs microfabrication process flow.

SEM imaging to have detailed topography information on our final device. Furthermore, the thickness of the PDMS protection layer is measured using a refractometer profiler, which helps estimate the acoustic attenuation loss.

### 5.2.1 Fabrication using soft nanoimprinting technique

Fabrication using soft nanoimprinting has the following major steps [112]: a hard mold made of Silicon, a soft mold made of PDMS, imprinting the polymer layer with the soft PDMS mold under curing conditions, and coating the device with a PDMS protection layer. Figure 5.1 shows the detailed steps of the whole fabrication process, as we will detail it in the following subsections.

#### Fabrication of Silicon mold

A 2-inch bare silicon wafer (P-type, B doped, $1-10\Omega\cdot cm, \langle 100\rangle$) is prepared and cleaned, then a $120nm$ layer of $SiO_2$ is either deposited by e-beam evaporation (ebeam Thermionics, $8\times10^{-6}\,Torr,\ 2\text{Å}/s$) or is grown using dry thermal oxidation ($6\,h$ @$950°C$), figure5.1a. The oxide layer will be used as a hard mask for the silicon deep reactive ion etching (DRIE) step. A CSAR6200.09 positive EBL resist was spin coated, figure 5.1b, (Brewer, $60s$ @$4000\,rpm$) over

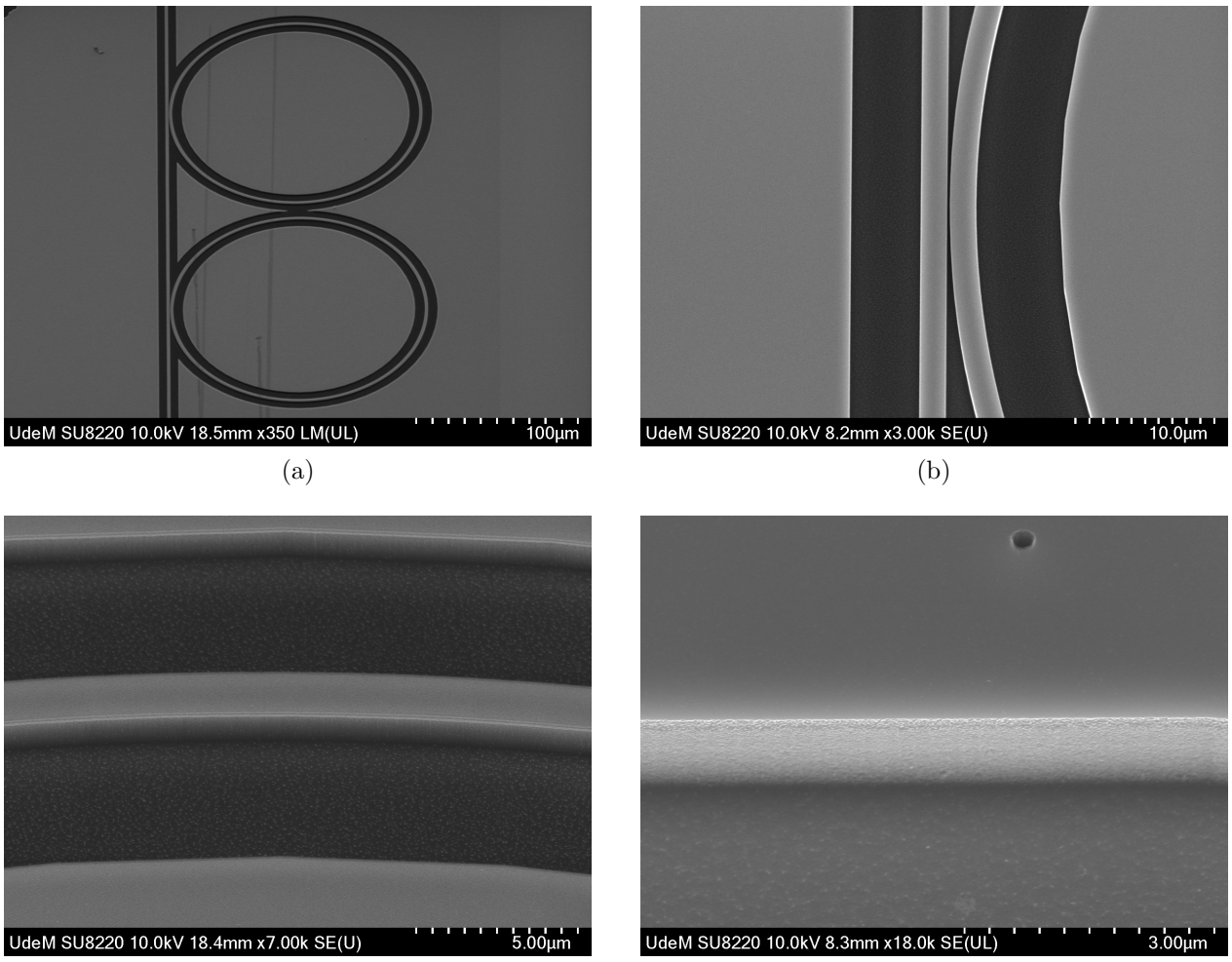
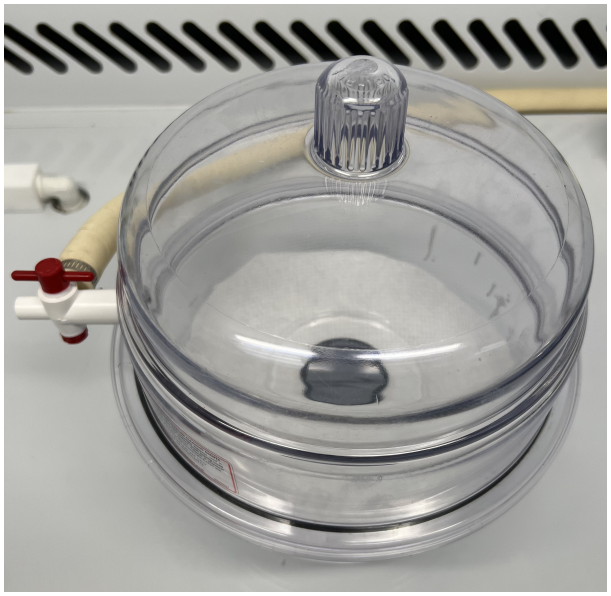
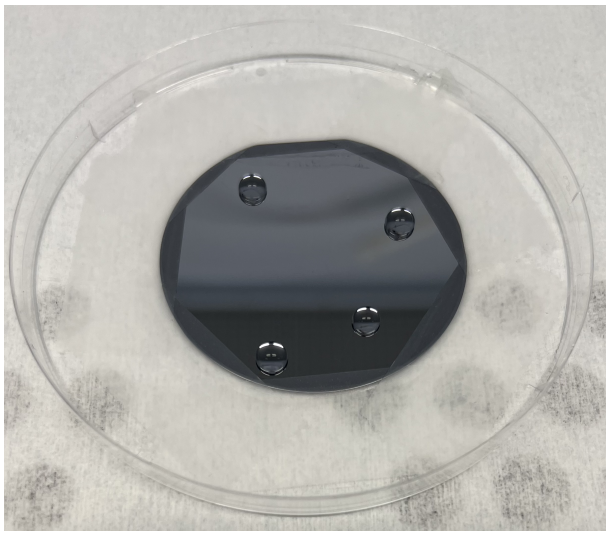



Figure 5.2 SEM images of the Si mold: (a) two-rings configuration, (b) Separation gap between the waveguide and the microring resonator, (c) waveguide's wall verticality, (d) waveguide's wall roughness

the wafer forming $200nm$ layer, and soft baked on a hot plate ($60s$ @$150°C$). The resist was exposed (dose $225\mu C/cm^2$, $100kV$) using Raith EBPG 5200 (3iT, Sherbrooke University), which provides large write fileds, high-speed patterning and critical dimensions down to $10nm$. The resist is then developed using O-Xylene for $60s$, rinsed with IPA for $60s$, figure 5.1c. PMMA EBL positive resist was used for fabricating another Si mold. A PMMA 950K A4 was spin-coated (Brewer, $30s$ @$2000\,rpm$) over the wafer forming $270nm$ layer, and soft baked on a hot plate ($180s$ @$180°C$). The resist was exposed (dose $100\mu C/cm^2$, $10kV$) using Raith 150 (GCM, Polytechnique Montreal) with critical dimensions down to $30nm$. The PMMA is then developed using immersion in $7:3$ IPA:water for $45s$, immersion in IPA for $45s$, and rinsed with water. The $7:3$ IPA:water mixture offers a cheaper and high contrast



(a)



(b)

Figure 5.3 Silanization of Silicon Mold

developer over the conventional 1:3 MIBK/IPA developer [113, 114]. An important step for eliminating the edge and sidewalls roughness after the following etching steps is the reflow of PMMA after development for ($90s$ @$115°C$) [50].

Silicon etching was done in two steps, the first step is to transfer the resist pattern to the $SiO_2$ layer using reactive ion etching (RIE) ($2min$, $200mTorr$, $2sccm\,O_2$ : $12sccm\,CHF_3$, 200 W). The $SiO_2$ etching rate was $58nm/min$ with a selectivity of 1 : 1.5 to the CSAR resist. Plasma asher ($O_2$, $3min$, $500W$) or acetone was used to remove the remaining resist out of the $SiO_2$ layer after patterning, figure 5.1d. The second etching step is the DRIE-ICP (inductively coupled plasma) etching of the silicon using the pseudo-Bosh process recipe (Oxford Plasmalab system 100, $33sccm\,SF_6$ : $55sccm\,C_4F_8$, $20°C$, 20mTorr, ICP 1200W, RF 20W). This process offers Silicon anisotropic etching with high wall verticality and less surface roughness for relatively low etching depth as in the case of our design $1.4\mu m$. The etching rate in this recipe is $720nm/min$ with a Silicon selectivity of 13 : 1 to $SiO_2$, figure 5.1e. After the Si DRIE-ICP etching, the remaining oxide layer will be removed by buffered hydrofluoric acid (BHF) etching, figure 5.1f. Another crucial step is required to reduce the sidewall roughness; a thermal dry oxidation of $50nm$ layer is grown ($3h$, @$950°C$) and removed by BHF. Figure 5.2 represents the SEM images of the fabricated Silicon mold after the DRIE step showing minimal surface roughness controlled by the pseudo-Bosh process as well as the gap separation between the waveguide and the ring resonator.

**Fabrication of PDMS soft mold**

PDMS is known to be a silicon-rich material that, in return, will make an adhesive bonding to glass or Silicon [115]. Consequently, the surface of the silicon mold was silanized with Trichloro(1H,1H,2H,2H-tridecafluoro-n-octyl)silane vapor to make the silicon surface hydrophobic and to prevent any PDMS adhesion to the mold. The Si mold is placed in a petri dish in a vacuum desiccator along with another small vial containing one drop of the aforementioned silanization agent. The desiccator was pumped down and left for 30 min to allow the deposition of an atomic layer of the silane vapor over the Si mold [116]. The wafer was rinsed with IPA and was baked ($10min$, @$110°C$) to remove any excess silane. The Si mold was tested afterward with some water droplets to ensure the success of the process. Uncured PDMS (10:1, Sylgard 184) precursor is poured on top of the silanized silicon mold, figure 5.1g. After thermal curing of PDMS mold ($2.5h$, @$80°C$) [117], it can be peeled off the master silicon mold, figure 5.1h.

**Soft nanoimprinting of SU-8**

As per device wafer preparation, a $5\,\mu m$ thick silicon thermal oxide wafer (P-type, B doped, $20\Omega \cdot cm, \langle 100 \rangle$) was prepared and cleaned. Spin coating of $1.4\,\mu m$ thick SU8.2001 layer (Laurell, two-step spin coating, Step 1: $5s$, @$500\,rpm$ with acceleration 114 $rpm/s$, Step 2: $35sec$, @$1200rpm$ with acceleration $342rpm/s$) followed by pre-exposure bake($60s$ @$65°C$, then $60s$ @$95°C$), figure 5.1i. UV curing step at a low dose ($30mJ/cm^2$) was done before thermal nanoimprinting to initiate cross-links in the SU-8 to be completed by thermal curing [97]. Following this step, the PDMS soft mold was put on top of the SU-8 layer and hand-squeezed to remove air between it and the device wafer. Under thermal treatment on a hot plate over the glass-transition temperature ($30min$ @$65°C$), the SU-8 layer will fill in the gaps of the mold by capillary force, figure 5.1j. Once the wafer cooled down to room temperature, UV flood exposure for $30s$ was performed to ensure that SU-8 was fully cured and the PDMS mold would be peeled off, figure 5.1k.

**Dicing and device encapsulation**

Applying the PDMS soft mold manually makes it hard to follow the orientation of the silicon wafer with respect to the optical waveguide, so cleaving the Si wafer is not an option. We used a dicing saw instead to split the wafers into chips which produced vertical facets reducing the insertion loss for edge optical coupling. A thick protection layer of AZ900MIR resist was spin-coated (Brewer: $60\,s$ @$1000\,rpm$, softbake: $60\,s$, @$900°C$) to prevent contaminating dicing

dust from sticking to the device layer. After dicing (ADT 7100 Provectus, blade: RESIN-00777-8003-006-QUP, $30\,krpm$, feeding speed $1mm/s$), the resist layer was removed using acetone. To be ready for underwater measurements, the wafer is encapsulated with a top layer of PDMS. To ensure good adhesion between the PDMS and the SU-8, oxygen plasma (Asher, $O_2$, $60s$, $200W$ step is used to introduce O-H groups on the SU-8 surface. Finally, uncured PDMS (15:1, Sylgard 184) precursor is then spin-coated on the device wafer (Brewer, $5min$ @$4000\,rpm$) to have a PDMS layer of $5\mu m$ and thermally cured ($30min$, @$80°C$), figure 5.1l.

### 5.2.2 Fabrication using EBL direct writing

This technique is straightforward and has only a few steps. It started with preparing and cleaning the device wafer (P-type, B doped, $20\Omega \cdot cm, \langle 100 \rangle$)) with a $5\,\mu m$ thick silicon thermal oxide, figure 5.4a. Secondly, spin coating of $1.4\,\mu m$ thick SU8.2001 layer was done (Laurell, two-step spin coating, Step 1: $5s$, @$500\,rpm$ with acceleration $114\,rpm/s$, Step 2: $35sec$, @$1200\,rpm$ with acceleration $342\,rpm/s$) followed by pre-exposure bake ($60s$ @$65°C$, then $60s$ @$95°C$), figure 5.4b. The exposure was done using Raith 150 (GCM, Polytechnique Montreal) at exposure parameters (dose $1.2\mu C/cm^2$, $30KV$, working field $200\mu m$) after several dose tests that were done to achieve the optimized exposure parameters minimizing electrons backscattering effect, and less surface roughness on written structures. After exposure, a post-exposure bake ($60s$ @$65°C$, then $2min$ @$95°C$) is required. The development of the exposed SU-8 was done using the SU-8 developer at room temperature for $2min$, and then immersed in a fresh SU-8 developer for another $2min$, and rinsed at the end with IPA only, figure 5.4c. The final step is the dicing and sample encapsulation similar as described in section 5.2.1, figure 5.4d.

## 5.3 Optical and acoustic characterization setups

Figure 5.5a illustrates the optical characterization setup for the MRRs array. A sweep of optical wavelengths from a tunable laser (Keysight N7776C) with a narrow optical bandwidth of $100kHz$ in the C-band is coupled with a single-mode (SM) fiber to the bus waveguide. The transmission spectrum of the MRRs is then captured by a single channel on a synchronized power meter (Keysight N7745C) through SM collection fiber. Alignment of input and output SM fibers with the waveguide facet is done with the 5-axis stage assisted with a microscopic camera system. The signal captured is then analyzed to get the resonance parameters such as quality factor Q and resonance wavelength $\lambda_r$. The setup was designed for edge coupling for waveguides that have a right angle between the input and output coupling fibers. UV-cured

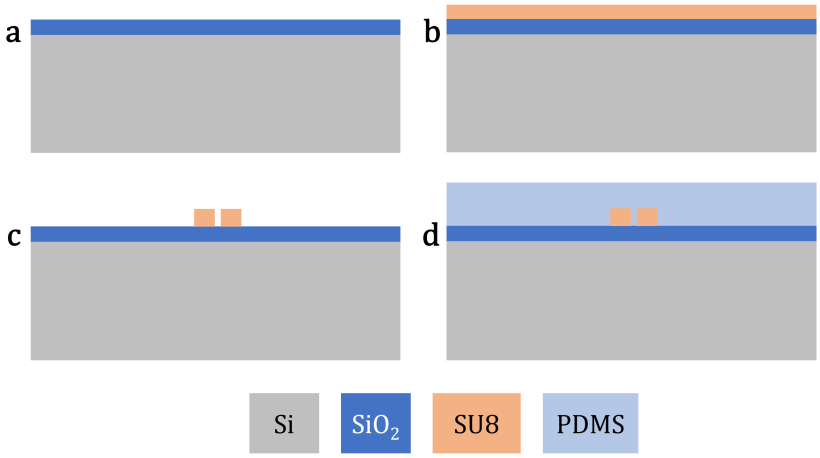



Figure 5.4 Microfabrication of MRRs using EBL direct writing

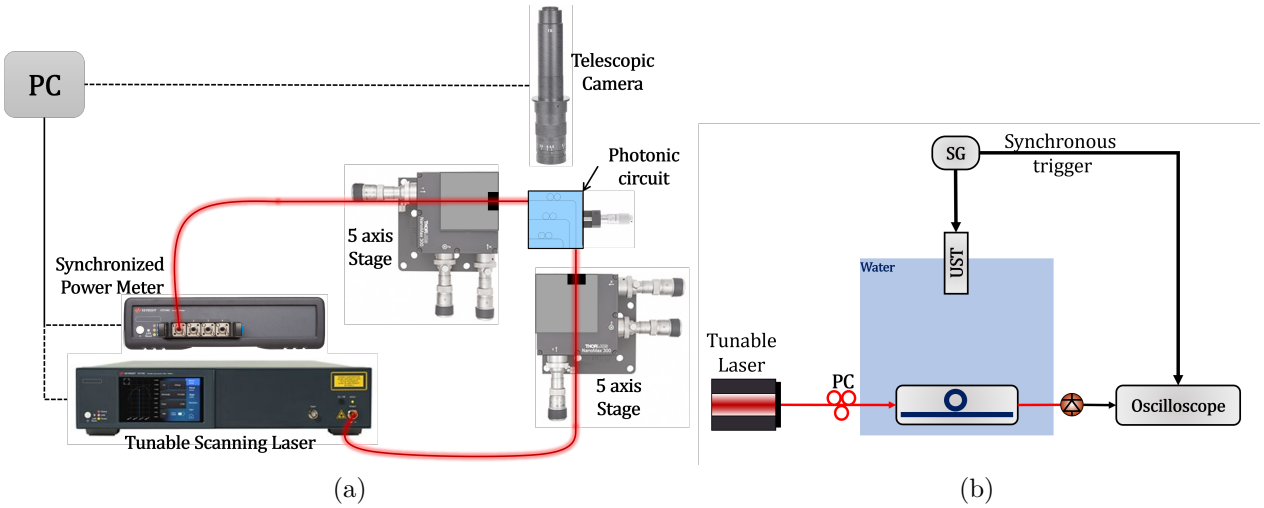



Figure 5.5 Characterization setups: (a) optical, (b) acoustic (UST: ultrasound transducer, SG: signal generator).

optical low-strain glue (Thorlabs, NOA65) provides permanent packaging after reaching the maximum possible coupling efficiency between the fiber and the bus waveguide [118]. It makes the device portaged for the latter underwater experiments.

As per the acoustic characterization, figure 5.5b, an ultrasound piezoelectric transducer UST (Olympus Parametrics NDT, $5MHz$, $10MHz$), which is controlled by a signal generator SG (Agilent 33220A, 20MHZ), or an ultrasound pulser/receiver (UTEX UT340), was used to provide the ultrasound excitation to the MRR in a water tank. A tunable laser (Keysight N7776C) was adjusted around a resonance of a single ring in one of the maximum slope regions in the optical transmission curve. The response of the MMR to the ultrasound pulse

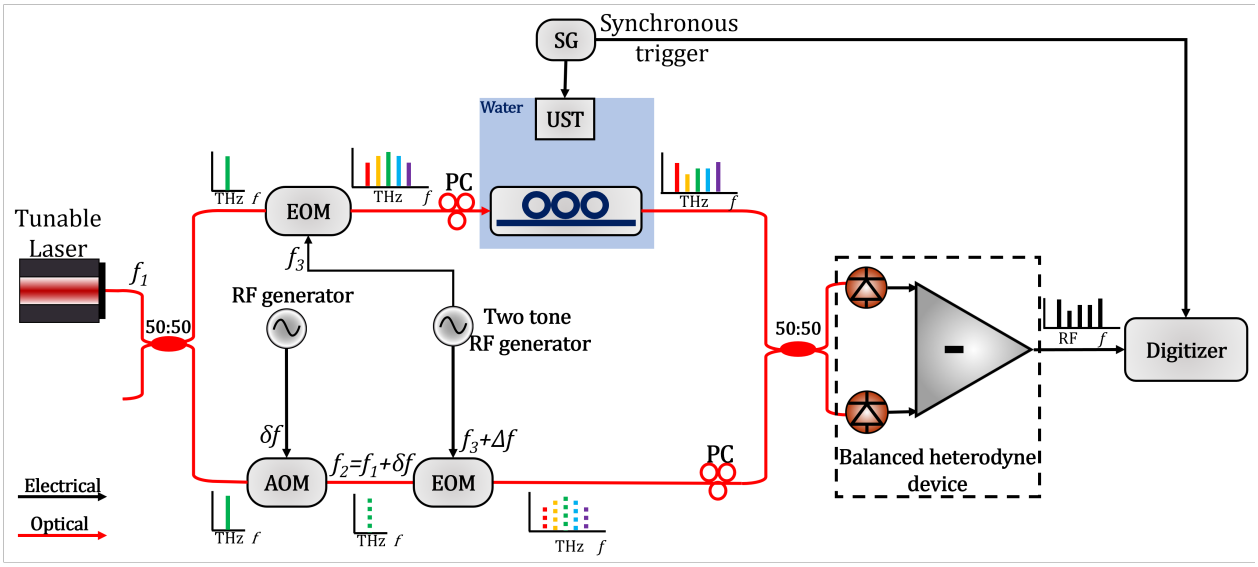



Figure 5.6 Electro-Optic frequency dual comb generation and detection schemes.

is detected by an amplified photodiode detector (Thorlabs, FPD610-FC-NIR, InGaAs PIN) on an oscilloscope (PicoScope 5244D 200 MHz) for further analysis. The US transducer was also characterized by sending the same US pulse on a metal plate target and the echo signal was captured for acoustic referencing.

## 5.4 Resonance shift interrogation using dual optical frequency comb scheme

As we introduced in section 4.3, we use the OFCs to measure the shift induced by the US perturbation in the resonance frequency using dual comb configuration. As shown in figure 5.6, the output from the c-band tunable laser (Keysight N7711A) acting as the central carrier frequency $f_1$ is split into two branches. The upper branch is the signal interrogation branch while the lower branch is acting as the local oscillator branch by a fiber splitter/combiner (OZ optics, FUSED-22-1550-9/125-50/50) with a splitting ratio of (50 : 50). The local oscillator branch is optically frequency shifted by $\delta f = 25MHz$ controlled by an acousto-optic frequency shifter (Brimrose, AMF-25-1550-2FP+) driven by $25MHz$ signal generator and high power RF amplifier (ZX60-100VH+). The two optical branches with slightly different optical frequencies are fed into two separate electro-optic phase modulators (Thorlabs LN65S-FC). Two-tone RF generator (Windfreak technologies, SynthHD v2) generates two-phase stabilized RF signals with a frequency shift of $\Delta f = 90MHz$ to drive the electro-optical modulator generating the OFCs. The generated optical frequency comb is then fed to the MRRs array through a polarization controller (OZ optics, PFPC-11-1300/1550-S-9/125). The same US

transducer (Olympus Parametrics NDT) controlled by a signal generator is used to provide the ultrasound signal excitation to the MRRs array in the water tank. The optically interrogated signal under US perturbation is frequency beaten with the local oscillator branch signal, after adjustment of the polarization to avoid optical mixing of two orthogonal polarized signals, with (50 : 50) fiber beam splitter/combiner (OZ optics, FUSED-22-1550-9/125-50/50) in a comb-to-comb manner. The two signals in the output branches are fed to two balanced amplified photodiodes in a heterodyne detection configuration (Thorlabs, PDB835C-AC). The beat note signal out of this photodiode configuration is down-sampled to the MHz signal regime ($< 300MHz$) and is acquired by the digitizer (AlazarTech, ATS9373, 12 bit, 4 GS/s).

## 5.5 Conclusion

To summarize, this chapter provided a comprehensive overview of the fabrication process, including a detailed description of each step and the corresponding equipment used. Moreover, the acoustic and optical characterization setups were described, highlighting their main components. Additionally, the design of the dual optical frequency comb (OFC) interrogation setup was explored, encompassing all the essential components and parameters. In the subsequent chapter, the acquired data and results obtained using these setups and systems will be presented and discussed.

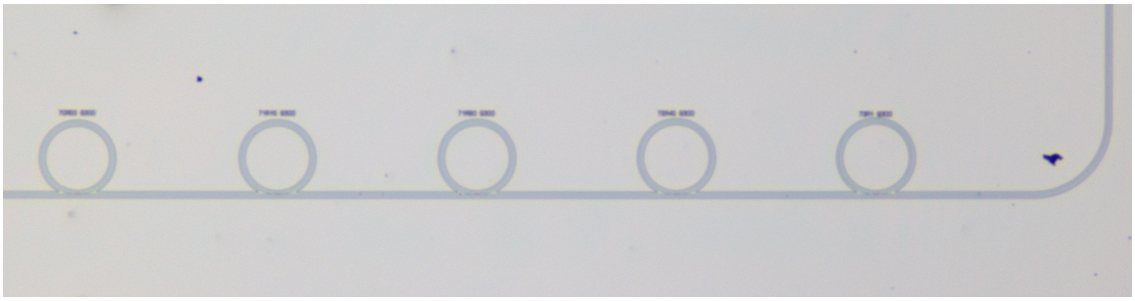
# CHAPTER 6 RESULTS AND DISCUSSION

## 6.1 General

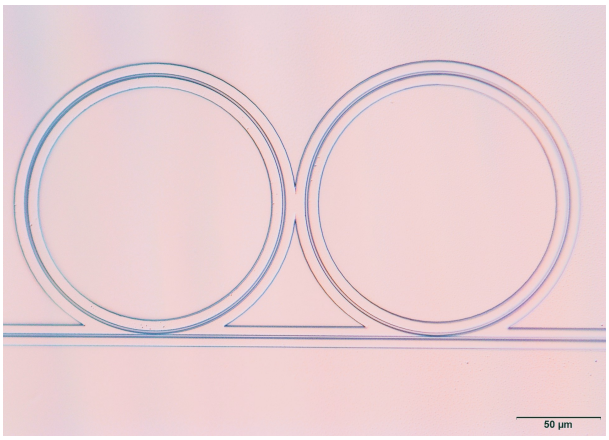
In this chapter, we will show all the experimental results including the geometrical, optical, and acoustic characterization of the fabricated devices. The ultrasound performance of the sensors is also discussed. Furthermore, the fabricated array performance of the rings is also presented followed by the parallel interrogation of ultrasound disturbance on 2 rings array configuration. Finally, we will have a general discussion section.

## 6.2 Fabricated devices

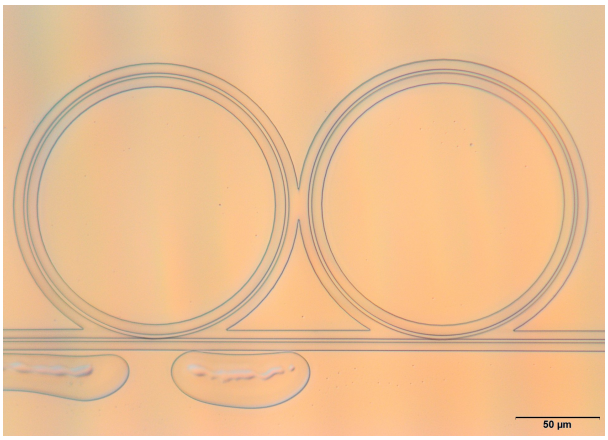
In order to assist in the successful fabrication of the devices, a visual and dimensional assessment is performed using optical microscopy and scanning electron microscopy. The fabrication of the five-ring array resonators with the ring radii indicated in table 4.2 was successful as shown in figure 6.1a. In the same chip that we fabricated, we have different configurations of ring array, two rings, three rings, and 4 rings so we will show the two rings configuration to demonstrate the successful fabrication steps. For the first technique of fabrication, the soft nanoimprinting, figure 6.1b shows optical microscopy images of the PDMS mold. The fabricated device shown in figure 6.1c visually demonstrates that the replica process was successful. Some places show the migration of the SU-8 polymer material while doing the molding, but it is away from the sensitive regions of our design. Further SEM imaging was required, figures 6.1d, 6.1e, to assess the gap separation and cleaved waveguide cross-section, a gap $g = 450\,nm$ was achieved. As the technique we are using for the mold relies on the capillary force to fill the mold with the liquid polymer, a trench of $5\,\mu m$ wide is considered around the waveguide to reduce the pressure force required for soft molding by reducing the amount of polymer that needs to be pressed and reduced the residual layer that is measured to be $109\,nm$. As per the direct writing technique, the scattering of the electron beam during exposure causes remaining resist residues so the gap was not clearly separated and the cavity performance is affected. The SEM images of the waveguide show high surface roughness that limits the performance of the EBL fabricated devices. Additionally, using the EBL with a thick SU-8 layer ($1.4\,\mu m$) using the available e-beam tool was a challenge for the resolution due to the ultimate low exposure dose and corresponding high e-beam scanning speeds that in return decreased the positioning accuracy and increased the distortion in the written structures.



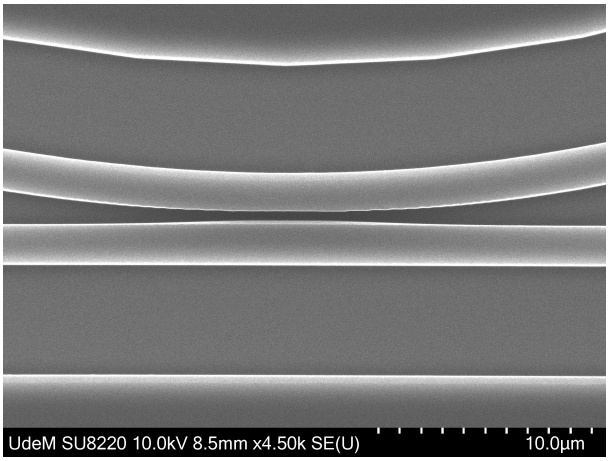
(a)



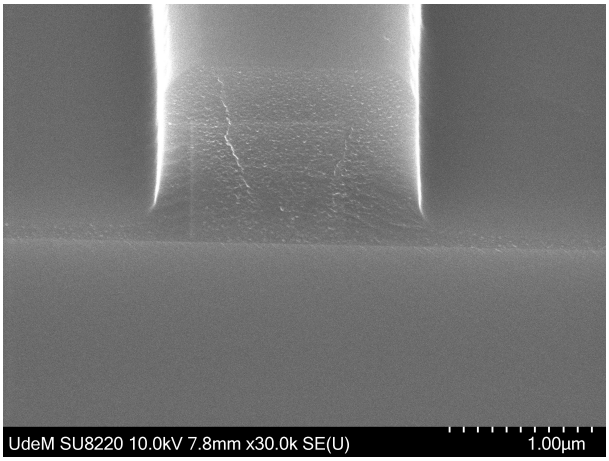

(b)




(c)

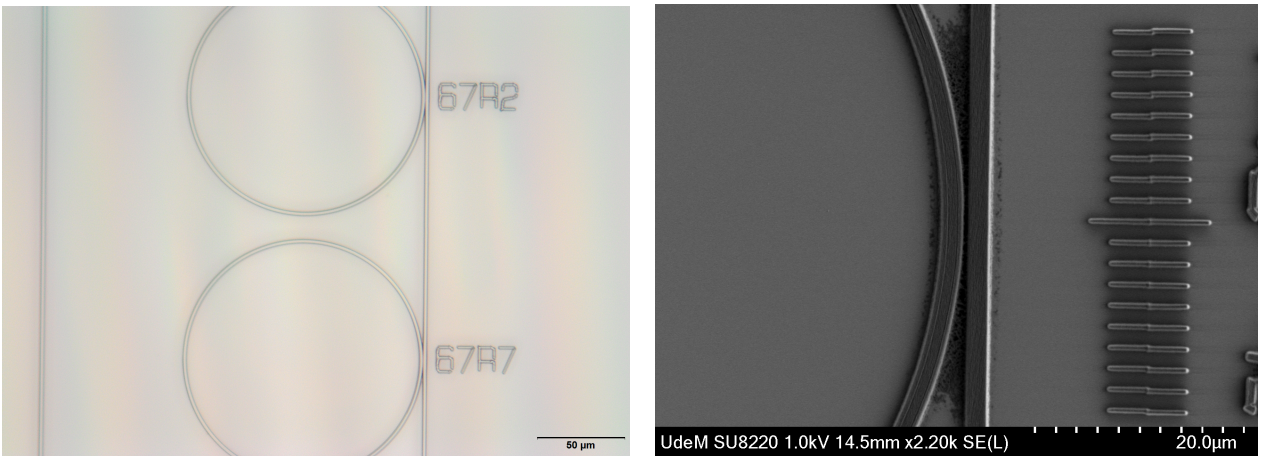



(d)




(e)

Figure 6.1 (a) Fabricated array of five micro-ring resonators, (b)PDMS mold, (c) SU-8 microring device array of two microrings, (d) SEM of the ring and waveguide showing the gap separation. (e) Cross-section of the fabricated waveguide.




(a) (b)

Figure 6.2 EBL direct written devices: (E) optical microscopy, (F) SEM showing the gap residuals and surface roughness

Table 6.1 Optical characterization parameters of a fabricated array of five microrings

| R ($\mu m$) | $\lambda_r$ ($nm$) | $\Delta\lambda$ ($pm$) | FWHM ($pm$) | Q | FSR ($nm$) |
|---|---|---|---|---|---|
| 70.50 | 1551.602 | | 23 | $6.8\times10^4$ | 3.364 |
| 71.15 | 1551.446 | 165 | 19 | $8.0\times10^4$ | 3.341 |
| 71.80 | 1551.281 | 165 | 26 | $6.0\times10^4$ | 3.289 |
| 72.45 | 1551.222 | 60 | 45 | $3.5\times10^4$ | 3.284 |
| 73.10 | 1551.100 | 122 | 38 | $4.0\times10^4$ | 3.231 |

## 6.3 Characterization of fabricated devices

For the optical resonance characterization, The normalized measured optical resonance of the five microring resonators array, listed in table 4.2, using the technique discussed in section 5.3, is shown in figure 6.3a. The achieved FWHM of the resonance of each ring along with its corresponding resonance wavelength and quality factors is listed in table 6.1, as extracted from figure 6.3b. These results show that the ring radii choice criteria discussed in 4.2.4, succeed in having multiple ring resonances in $500\,pm$ spectral bandwidth. However, the fabrication uncertainties lead to some variations in the quality factors as well as the positions of the resonance wavelengths. As per the acoustic characterization, as configured in section 3.3.2, an MRR was characterized by transmitting $20\,ns$ rectangular pulse with $100\,V_{p-p}$ amplitude and a repetition period of $90\,\mu s$ through two different US transducers with central frequencies of $5\,MHz$ and $10\,MHz$. The transducers were characterized first by

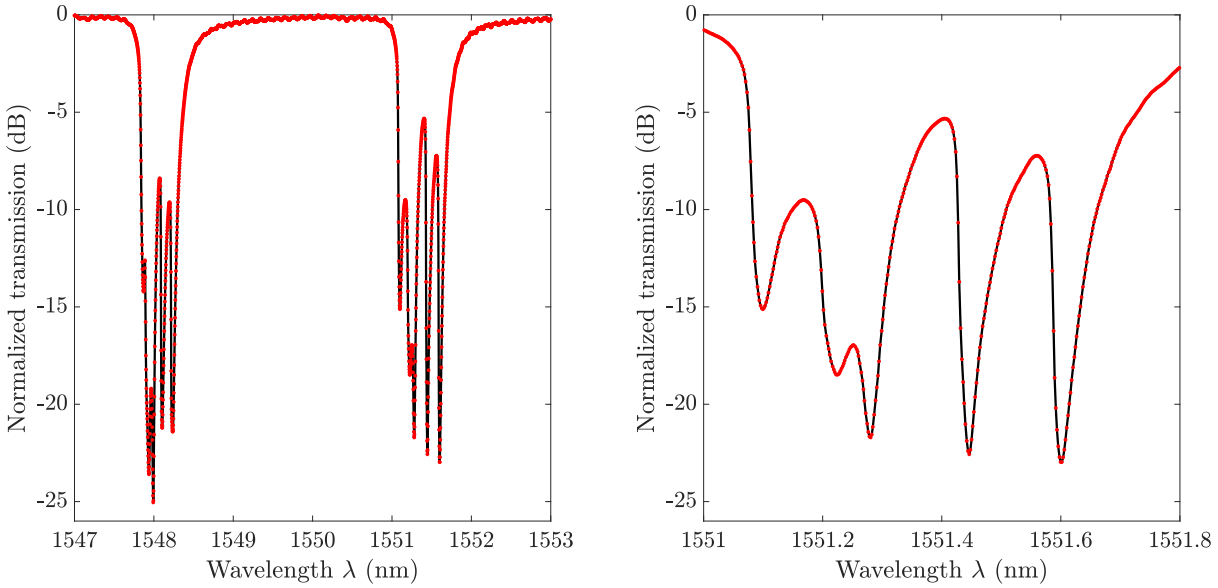



Figure 6.3 Resonance spectrum of five-ring microresonator array (a) extended view, (b)close up view.

targeting a metallic plate and the reflection was captured on the oscilloscope. The measured reflected signal was analyzed to have the acoustic transmission frequency spectrum out of the US transducers. Replacing the metallic target with our MRR, we measured the variation in the optical signal due to the US perturbance. Figures 6.4a and 6.4b show the measured pulse response to the $5\,MHz$ and the $10\,MHz$ transducers, respectively. The extracted normalized frequency response of the MRR is shown in figure 6.4c which has peak frequency response at $9\,MHz$ with a $-3dB$ bandwidth of $8\,MHz$ and $-6dB$ bandwidth of $13\,MHz$. As the MRR is known for its wideband frequency response, the given frequency response is limited to the bandwidth of the used US transducers, so the response to other frequencies is possible if a wideband US transducer or multiple US transducers with different central frequencies are used.

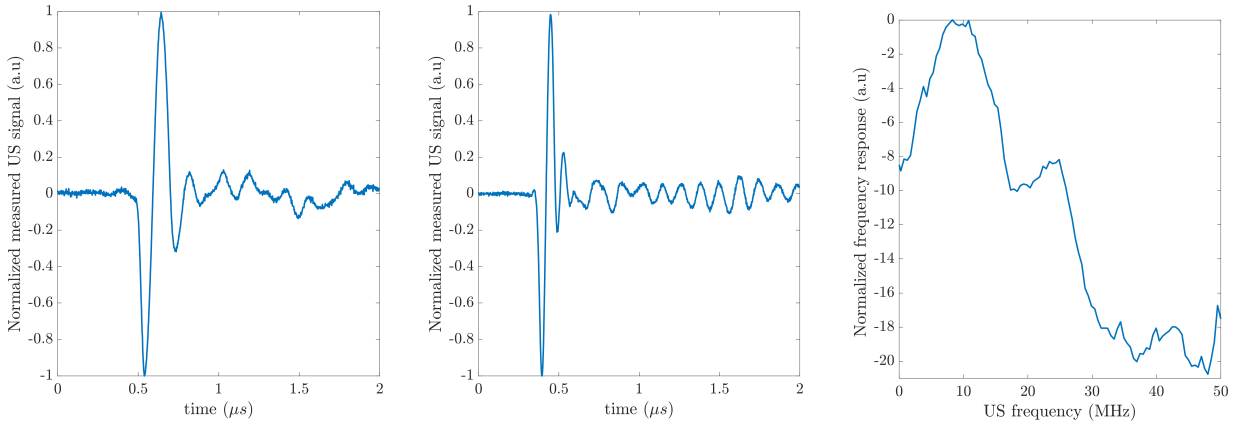
In order to measure the sensitivity of the MRR, the wavelength of the laser source is set at the probing wavelength, then a single cycle of $10\,MHz$ sinusoidal wave with a peak-to-peak voltage of $5\,V$ is fed to the $10\,MHz$ ultrasound transmitter that corresponds to output peak pressure of $15\,kPa$ [56]. Using the amplified photodiode attached to an external amplifier with a gain of $28\,dB$, the measured amplitude of the signal is $476\,mV$, so the sensitivity is $31\,mV/kPa$. In order to calculate the NEP, it is the sensitivity over the root mean square of the noise of the photodiode configuration which is measured to be $5mV$, so the NEP is

161.3 $Pa$ over 1-20MHZ bandwidth.

### 6.4 Parallel signal interrogation using OFCs

As discussed in section 6.3, due to the fabrication uncertainty, the fabricated five-ring array are close to each other but not enough to be within the bandwidth of the EOMs as suggested by the technique described in section 5.4. In that manner and to prove the concept of the interrogation using dual optical frequency combs, we interrogated a two-ring array of combs which was designed using the same fabrication process and parameters of the five-ring array. A design of a two-ring radii array with $R1 = 77.6\,\mu m$,$R1 = 78.9\,\mu m$ was considered. The spectrum of the two-ring array was measured at a water temperature of $21°C$ and shown in figure 6.5, left axis. The quality factors are $Q \approx 5.98 \times 10^4$ at $\lambda_r = 1550.730\,nm$, $Q \approx 5.99 \times 10^4$ at $\lambda_r = 1550.912\,nm$, respectively. In the same figure, right axis, the acoustic sensitivity term $dT/d\lambda$ was calculated and shows the probing wavelengths that are to be set using the optical frequency combs to measure the acoustic signal from each individual ring simultaneously. As our measurements were all performed underwater, the water was kept at a constant temperature of $21°C$ using a temperature controller to $0.1°C$ variations. In order to detect the US disturbances signal from both rings together, we assigned an optical probing wavelength for each ring that was generated by the OFC. The probing wavelengths are $\lambda_{p1} = 1550.742\,nm$ and $\lambda_{p2} = 1550.901\,nm$. At this stage, we are turning from expressing the optical parameters from wavelength to frequency so we can have a common terminology with the EOM parameters. So the first optical probing frequency was $f_{p1} = 193321.94\,GHz$ and $f_{p2} = 193302.12\,GHz$. The laser central frequency was set in exactly the center between the two frequencies at $f_1 = 193312.03\,GHz$ which will be the center frequency for the first EOM. For the second EOM, the center frequency was shifted by $\delta f = 25\,MHz$ modulated by AOM to be $f_1 + \delta f = 193337.03\,GHz$. The difference between the probing frequencies was $f_d = 19.82\,GHz$, so the frequency adjustment for the first EOM was set to $f_3 = f_d/2 = 9.91\,GHz$ out from the RF generator channel 1 and the second EOM was set to $f_3 + \Delta f = 10.00\,GHz$ out from the same RF generator channel 2. $\Delta f$ was set to $90\,MHz$ to avoid the overlap with $\delta f$ harmonics in the down-conversion between the optical domain and the RF domain. The down-converted frequencies are then $25\,MHz$ which represents the central frequencies of the two combs $p = 0$, $65\,MHz$ corresponds to the first right-hand side-loop $p = +1$, $115\,MHz$ corresponds to left-hand side-loop $p = -1$.

The same pulsed electrical signal ($100\,V_{p-p}$, $20\,ns$ rectangular, repetition period $90\,\mu s$) was fed to the $5\,MHz$ US transducer which was set in two positions, one was in the normal direction to the rings array and the other was inclined by an angle relative to the normal. The signal




(a) (b) (c)

Figure 6.4 Fabricated MRR response to US pulse generated by (a) $5\,MHz$, (b) $10\,MHz$, (c) Normalized US frequency response.

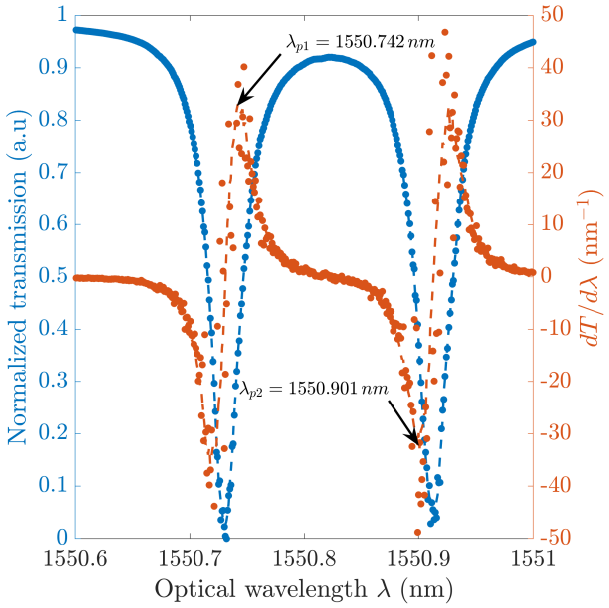



Figure 6.5 The resonance spectrum of the two-rings array at $T_w = 21°C$ with the derivative of the transmission vs the optical wavelength

analysis was done using the signal processing technique of down-conversion to the baseband described before in section 4.3. The time domain output signal from the balanced heterodyne detector as acquired by the Alazar digitizer over a time period of $800\,\mu s$ is shown in figure 6.6a, with its Fourier transform shown in figure 6.6b indicating the three main down-converted frequencies ($25\,MHz$, $65\,MHz$, $115\,MHz$). Our optical probing frequencies are represented

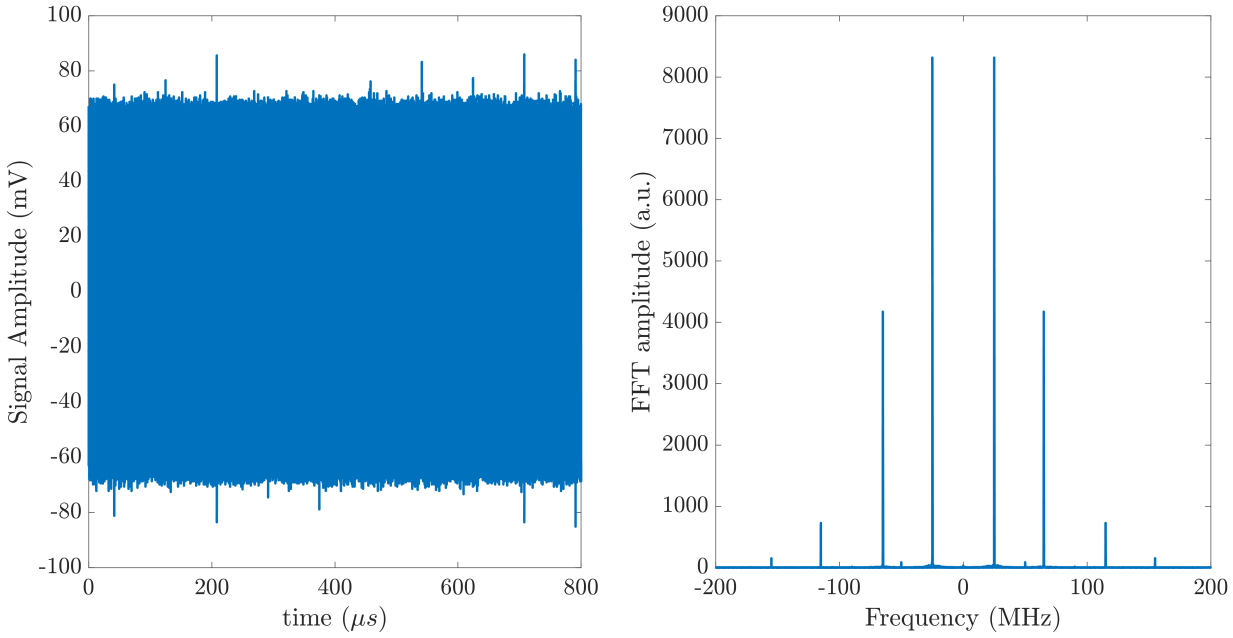



Figure 6.6 Acquired output signal from the balanced heterodyne detector by the Alazar digitizer: (a) Time domain, (b) Frequency domain by Fourier transform.

by the side loop down-converted RF frequencies which are $65\,MHz$ and $115\,MHz$. In that manner, analyzing the carried signals on each of these frequencies individually gave the corresponding US disturbance signal on its corresponding MRR.

The carried signal on the $65\,MHz$, $115\,MHz$ carrier frequencies is shown in figure 6.7a and 6.7b, respectively, after shifting these carrier frequencies one by one to zero-frequency and performing the low pass filter with $20\,MHz$ cut-off frequency. The high variations in the amplitudes correspond to the imperfect symmetry in the optical path length of the two optical branches in between the two optical beam splitters as seen by two different optical frequencies. The bandpass filtration of these signals around the central frequency of the acoustic transmitter $5 \pm 2.5\,MHz$ retrieves the ultrasound signal from both MRRs as shown in figures 6.8a and 6.8b. Zooming in on one pulse showing the response from both rings together is shown in figure 6.9a for the normal transmission and figure 6.9b for the inclined transmitter. The time delay between the responses is in the ns regime ($\approx 70\,ns$) as the distance between the two rings in the array is $150\,\mu m$.

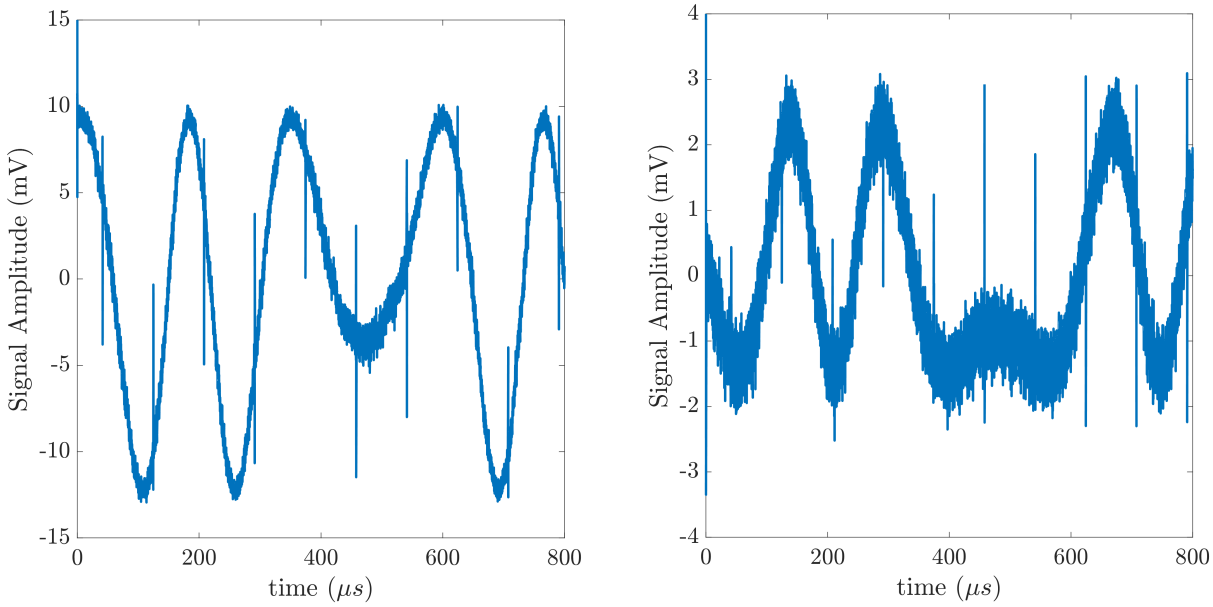



Figure 6.7 Carried signals on each carrier frequency after down conversion to baseband: (a) 65 $MHz$ carrier frequency, (b) 115 $MHz$ carrier frequency.

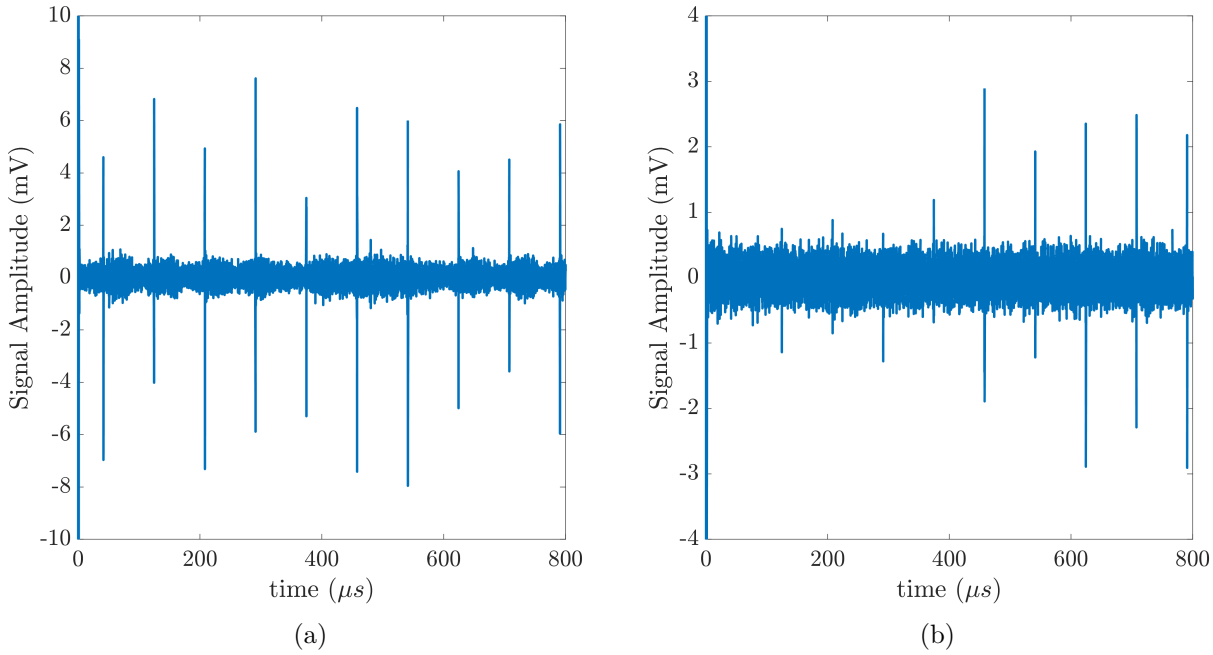
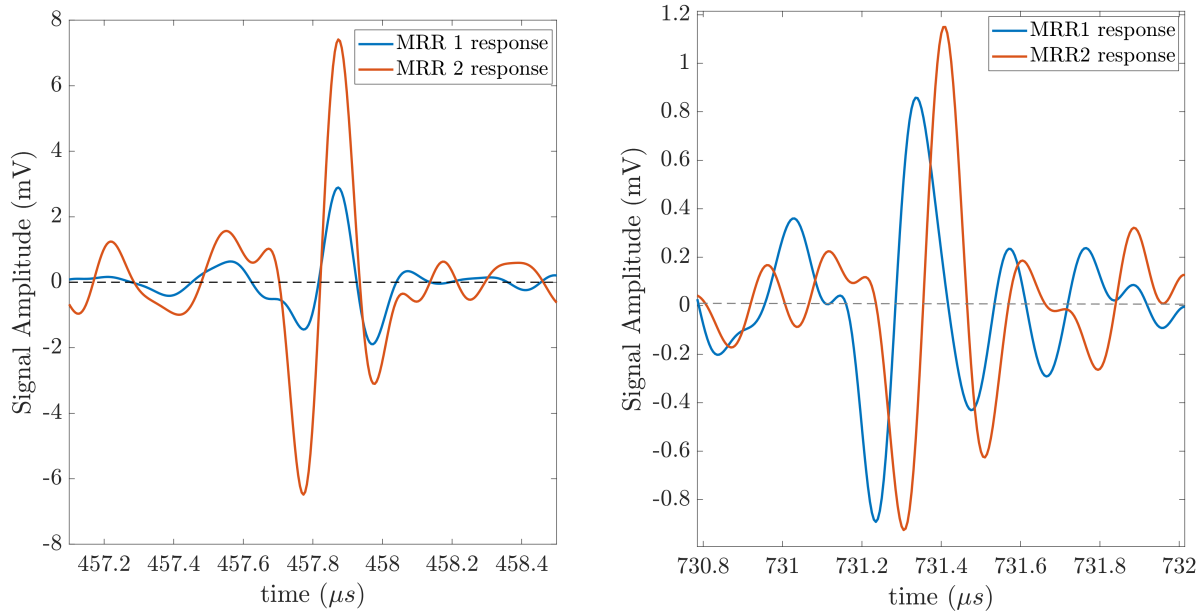



Figure 6.8 Retrived US signals from the MMRs after the bandpass filtration around the transmitter central frequency: (a) 65 $MHz$ carrier frequency, (b) 115 $MHz$ carrier frequency.



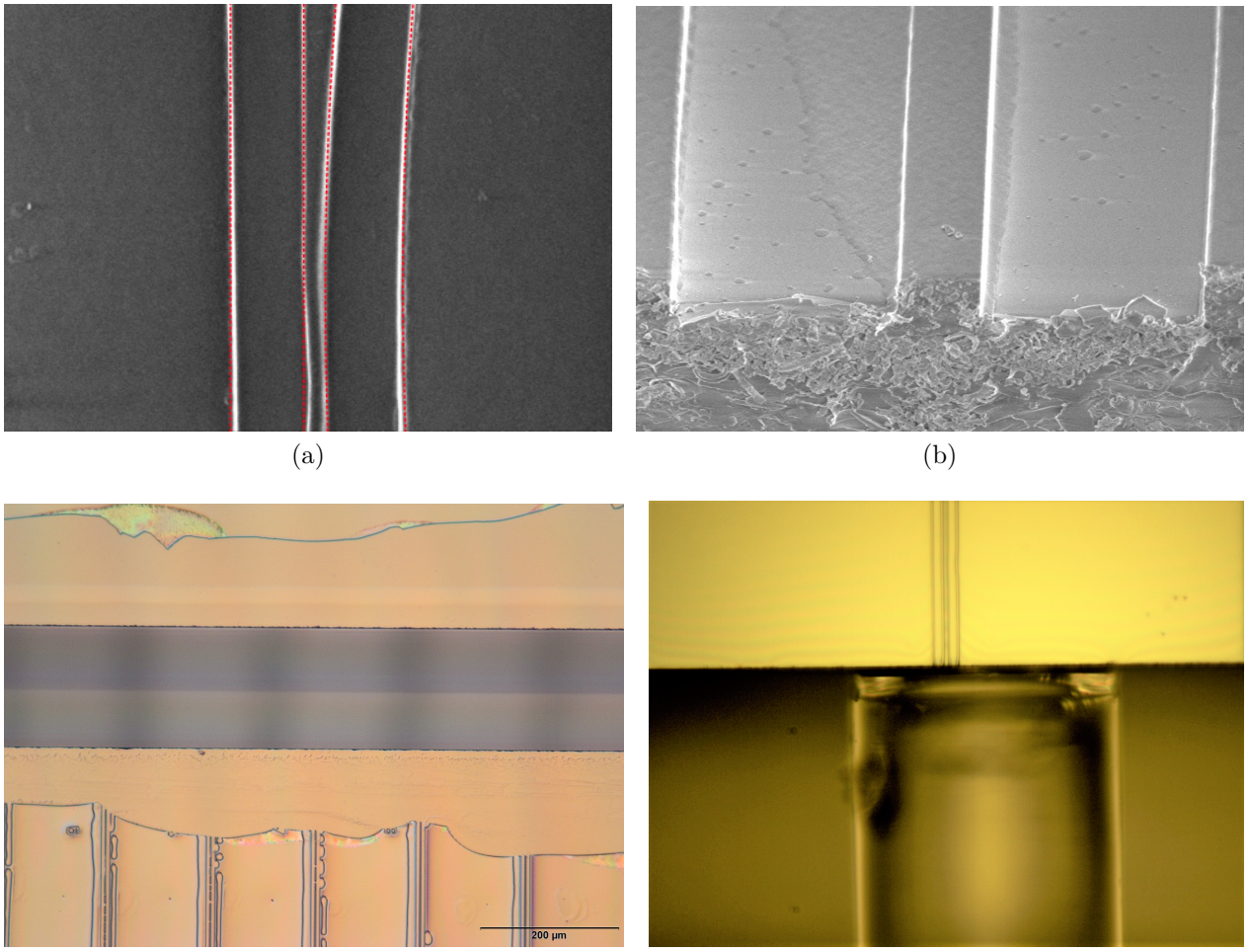

(a) (b)

Figure 6.9 Retrived US response of the two MRRs in both (a) Normal transmission mode, (b) Inclined transmission mode.

## 6.5 General discussion

### 6.5.1 Fabrication and packaging techniques

The offered soft nanoimprinting technique is successful in reaching critical dimensions in the order of 200 $nm$ which makes this technique a relatively low-cost technique as the Si hard mold is fabricated once and the cast low-cost PDMS mold can be used multiple times until it is contaminated. The PDMS mold can be cast again using the same Si hard mold. Therefore, for getting a device, the only thing that is needed is a hot plate, as it relies on filling the gaps with melted polymer with capillary force, and a torch UV light for flood exposure if the polymer is UV sensitive. Despite the excellent critical dimension that the nanoimprinting technique can achieve, the elastic property of the PDMS material can have a curvature deformation of the straight structures as shown in figure 6.10a, due to the applied pressure by hand that is nonuniform and uncontrolled. The nanoimprinting is perfect if the layer dedicated to this technique is the first layer of the patterned structure and the upper layers can be aligned to it. However, if this is not the case, the alignment of the PDMS mold structure on the current patterned layers is a big challenge. This challenge also drove us to use the dicing saw as structures are not aligned with the carrier wafer crystal orientation




(a) (b)

(c) (d)

Figure 6.10 SEM images of the fabricated devices showing (a) curvature deformation, (b) coupling edge, and microscopic images for (c) the dicing effect on polystyrene waveguides, (d) coupling fiber drifting after gluing.

making cleaving not an option. Using the dicing saw either leaves the edges with a high surface roughness, figure 6.10b, or destroys totally the edge of the waveguides as in the case of the Polystyrene trials that we fabricated, figure 6.10c, that increases the insertion loss. Due to the edge surface roughness and the low cross-section dimension of the waveguide in comparison to the coupling fiber core during coupling, a total insertion and propagation loss of $25\,dB$ was measured which makes the optical signal to be weak for detection. Furthermore, for the underwater US measurement constraint of our project, the samples are packaged with UV glue to attach the coupling fiber permanently to the edge sample. Any small movement of the glue when it shrinks during curing or when it is exposed to water affects the coupling and adds more insertion loss, in the order of $5dB$, figure 6.10d, which was an

additional challenge. Grating couplers [119] or other edge coupling techniques [120] were optimized for SOI photonics but are still under investigation case-by-case for the polymer materials [121, 122]. The fabrication uncertainties in the dimensions with EBL patterning were $50\,nm$ for PMMA resist that affects the resonance of the theoretically chosen ring radii. As shown in figure 6.3b, the measured spectrum shows differences in amplitudes as well as spectral positions of the resonances to each other because of these fabrication uncertainties which can be minimized but not eliminated. Localized heaters can be used to tune the index of refraction of each ring individually but it will increase the complexity of fabrication. A recently published article used optically controlled chalcogenide-based materials, whose index of refraction can be tuned optically after fabrication [66].

Furthermore, The SU-8 material is known for its negative thermo optic coefficient $\approx -1.1 \times 10^{-4}$ k$^{-1}$ [123] so the spectrum is temperature sensitive. Figure 6.11, shows the spectrum change of the two-ring microresonator array over temperature variation $T_w$ from $21°C$ to $27°C$. A change in the quality factor is also noticed due to the change in the cavity parameters and fabrication uncertainties, so polarization tuning is always required when the working temperature is reached and stable. Consequently, the showed measurements of the fabricated devices are from the best successfully fabricated devices. The fabrication process shows a reliability on the quality factor and the resonance wavelengths, however some fabricated devices were disqualified regardless of their performance due to the very narrow bandwidth required for the OFC criterion of parallel detection.

### 6.5.2 Optical power and noise limitations in dual OFC setup

Optical and RF power management in our setup is so important. However, as we are introducing the first version of the current setup and the fabricated devices, an optimization step is required to reach the maximum efficiency and low overall noise. First, as we are working on an interferometric mode, a laser source with a very narrow optical bandwidth is required for the coherence length limitation. The interferometric loop itself is sensitive to the unbalance in the optical path lengths between the two branches which are not perfectly equal and causes the noticed low frequency variation in the extracted signal from each comb signal. The carried ultrasound signal is also affected by these variations as it can either saturate the photodiode or pull it down to the noise level. Second, The output power of the laser source we used is limited to $16\,dBm$. We split the power equally between the signal interrogation OFC branch and the OFC local oscillator branch so that we only make use of half of the power for the interrogation of the US signal from the microring array. Each EOM has an extra $3\,dB$ optical insertion loss and the AOM in one branch has a $2\,dB$ optical insertion loss which

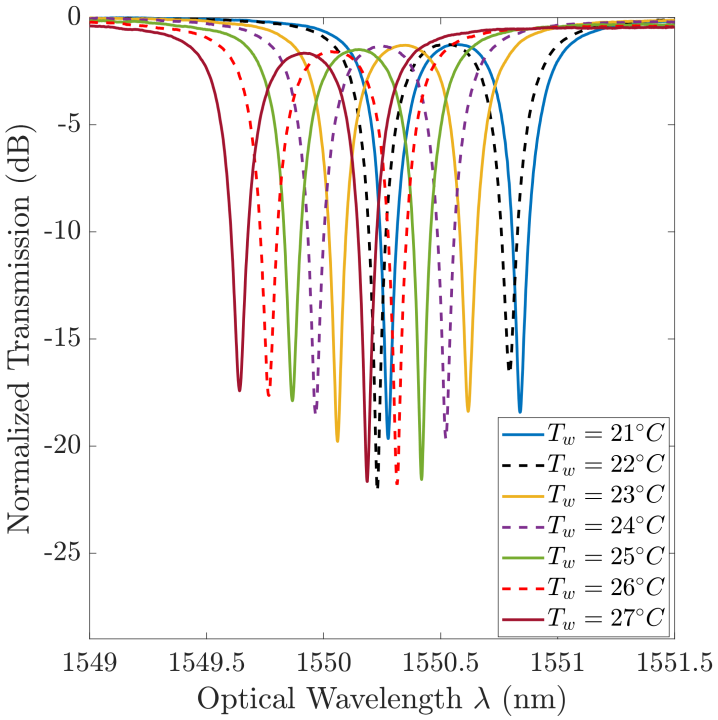



Figure 6.11 Effect of variation of water temperature $T_w$, on the resonance parameters of two-rings array.

both are unavoidable as these are factory specifications. Third, the EOM are distributing the optical powers to the sidebands during the generation of the optical frequency combs that we are mainly using for detection. Fourth, the insertion and propagation loss of $25\,dB$ that was measured for the fabricated devices discussed in the previous section can be reduced by reducing the edge roughness by chemical treatment after fabrication or using ultra-high numerical aperture (UHNA) fibers for coupling or replacing the edge coupling with a custom designed and fabricated grating couplers suitable for polymer waveguides. Besides, we are relying on the detection of our US signal using a high-quality factor in the linear curve of the spectrum which is $-20\,dB \rightarrow -25\,dB$ below the nonresonance laser power level, and by increasing the total level of the nonresonance power or using the rings in drop-in configuration that will increase the complexity of the system and loosing the SISO configuration. Thanks to the EOM dual comb configuration that combines the optical local oscillator higher power signal with the very low signal that allows the detection of these ultra-weak signals without averaging as indicated in figures 6.9 but the SNR is still low. These challenges required further optimization of the system by different means such as using ultrahigh power laser, replacing the EOMs and AOM with low insertion loss alternatives, and reducing the insertion

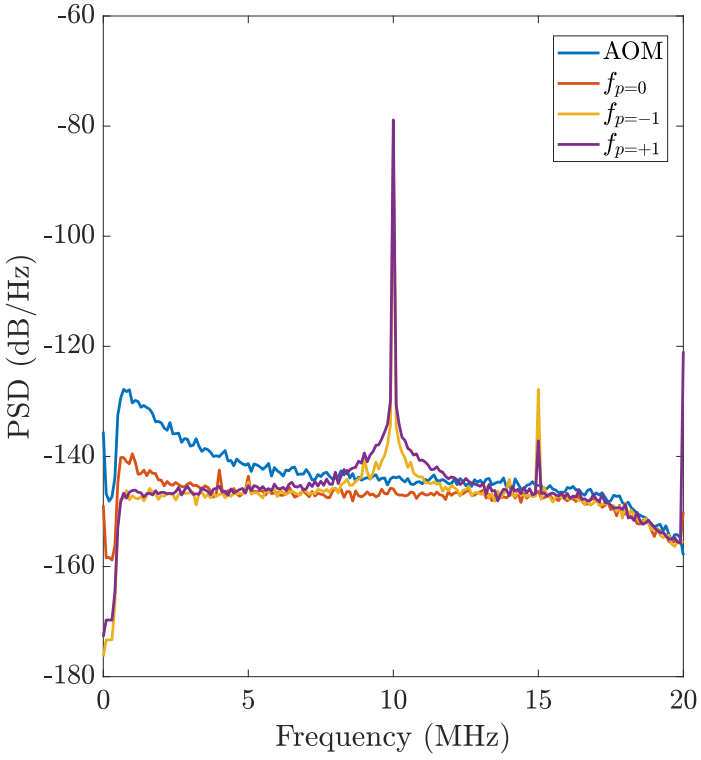



Figure 6.12 Welch PSD noise estimation of the OFC

loss of the devices by cleaving the samples instead for edge coupling or using grating couplers.

The noise analysis of the OFC generation was performed, figure 6.12, using Welch's power spectrum density estimator [124] for the signals that are retrieved from each comb frequency with a low pass filter of $20\,MHz$ while no ultrasound perturbance was applied. we used a Hanning window segment having the same number of samples per one pulse repetition period of the acoustic signal with an overlap of 40% between each window. The sources of noise in the dual optical frequency combs generated by electro-optic modulators are laser noise, phase noise, and photodiode noise. The phase noise sources are the laser source noise, the driving RF generator noise, the optical amplifier noise, and the environmental variation noise [125]. The noise analysis shows a high noise level at certain frequencies which are multiples of $4MHz$ and $5MHz$ only on the generated combs in comparison to the signal shifted with only the AOM and is using the same interferometric loop as well as the photodiode, and that explains why we still have noise along with our detected signal at these frequencies. In that manner, the phase noise due to the optical frequency comb generation is dominant by either the RF generator or the environmental variations. The phase noise can be eliminated by tuning the phase of the RF generator driving the EOM by a PID control based on the

phase measurement [68, 126] which was beyond our scope in this thesis.

## 6.6 Conclusion

In this chapter, we discussed the experimental results regarding the geometrical and functional properties of the fabricated MRR array. We also discussed the results of the acoustic characterization of the fabricated MRR. The choice of the OFC generation parameters was also investigated, which led to interrogating the signal from the MRR array simultaneously in two modes of detection, normal mode, and inclined mode. We concluded the chapter with a general discussion about the limitations of fabrication and the OFC setup including the noise analysis. A comparison between the current work and the state-of-the-art of the microring resonator devices is concluded in table 6.2. The next chapter will discuss the conclusion and recommendations that came out of this work.

Table 6.2 Comparison of the state-of-the-art on-chip optical microring sensors and their parallel detection techniques.

| Work | Material | Structure | Element size ($\mu m$) ($W \times H \times R$) | -6 dB acoustic bandwidth (MHz) | NEP (Pa) | Number of elements | Parallel interrogation |
|---|---|---|---|---|---|---|---|
| [57] | Polymer (PS) | Microring | $2.00 \times 2.00 \times 50$ | 70 | 4100 | 4 | - |
| [32] | Polymer (SU-8) | Microring | $0.80 \times 0.80 \times 30$ | 140 | 6.8 | 1 | - |
| [30] | Polymer (PS) | Microring | $0.80 \times 0.80 \times 30$ | 140 | 0.49 | 1 | - |
| [44] | SOI | Slab on microring | $0.45 \times 0.17 \times 15 \sim 20$ | 27 | 5.5 | 10 | WDM |
| [66] | Chalcogenide | Microring | $2.40 \times 0.85 \times 40$ | 175 | 7.1 | 15 | Digital OFC |
| This work | Polymer (SU-8) | Microring | $2.00 \times 1.500 \times 70 \sim 80$ | 13 | 161.3 | 2 | Dual OFC |

# CHAPTER 7 CONCLUSION AND RECOMMENDATIONS

## 7.1 Conclusion

On-chip optical-based techniques, especially microresonators, for detecting ultrasound signals for biomedical imaging gain great interest for their integration capabilities, small dimensions, high sensitivity, and immunity to electromagnetic interference noise. Efficient ultrasound imaging depends on multiple highly sensitive transducers in the form of an array. The sensitivity of these transducers to ultrasound is important, but efficient parallel interrogation of all the elements is critical, particularly for imaging of transient phenomena that require ultrafast acquisition rates.

The main objective of this thesis was to develop an approach for an all-optical ultrasound receiver that has ultrafast ultrasound imaging capabilities. In order to reach that goal, we started with a deep theoretical analysis of the microring resonators' performance, ultrasound sensitivity, and limitations with the help of FEM simulation tools. This analysis helped us choose suitable ring radii to be included in the detection array, considering the restrictions imposed by the optical frequency combs. The rings within the array are connected to the same bus waveguide, allowing a single-input, single-output configuration that massively reduces the number of channels. Another significant achievement was the fabrication of the designed microring array in a way that can be generalized for polymers and doesn't depend on the UV or electron beam sensitivity of the polymer. This technique is the nanoimprinting technique using a low-cost PDMS mold that was developed and optimized until the successful fabrication of a microring resonator array reaching critical dimensions of a few hundred nanometers. This microfabrication technique involves the following main steps: the fabrication of a hard mold made of Silicon, the casting of a soft mold made of PDMS, nanoimprinting of the final device structures using a hot plate, and packaging for the experimental setup.

For the experimental setup, an optical and acoustic characterization setup was investigated and built for extraction of the optical and acoustic parameters of the fabricated microring resonators. High quality factor resonance of $6 \times 10^4$ was achieved for the designed polymer microrings that allowed high sensitive acoustic measurements with a sensitivity $31\,mV/kPa$ and NEP of $161.3\,Pa$ with $-6\,dB$ bandwidth of $13\,MHz$. The optical dual frequency comb detection technique for parallel interrogation of the microring resonators in ultrasound detection was also investigated. As a proof of concept, the setup was built and used for the interrogation of two ring resonators simultaneously under the excitation of ultrasound waves. The same technique with the current setup is applicable to a larger number of ring resonators

that have their resonances within the bandwidth of the generated optical frequency combs. The setup parameters are tunable and can fit different applications of ultrasound detection with a wide range of frequencies.

In summary, this thesis has made a significant contribution by introducing the utilization of dual optical frequency combs for simultaneous signal interrogation from an array of polymer microring resonators which is, to the best of our knowledge, novel for this type of signal interrogation. Our groundbreaking concept for parallel signal detection has formed the basis of an invention disclosure for a patent application at Polytechnique Montreal, identified as *"DIV-1000-Capteur pour échographie biomédicale basé,"* which is currently pending review. Additionally, we have submitted a scholarly article titled *"Ultrafast ultrasound imaging by optical polymer microring resonator array and a dual optical frequency comb: A theoretical Concept"* concerning the theoretical analysis and simulations discussed in chapter 4, which is also under review. Furthermore, the fabrication process and the results of signal interrogation described in chapters 5,6 are being prepared for another article titled *"Parallel ultrasound signal interrogation of a polymer optical microring resonator array using dual optical frequency combs"*.

## 7.2 Recommendation and potential applications

From the fabrication point of view, the soft nanoimprinting technique is a low-cost promising technique to reach nanostructures, especially for the nonsensitive to UV or electron beam polymer materials. However, the inability to align the structures with other prefabricated structures poses some limitations on the integration of this technique with other techniques. Despite the fact that all the realistic parameters in the simulation were taken into consideration, there are some deviations in the fabricated devices, making tuning the fabricated microrings a must particularly when dealing with an ultra-narrow bandwidth of the optical spectrum limited by the electrooptic modulator bandwidth.

Furthermore, the coupling insertion loss of the fabricated devices should be massively reduced to avoid extra optical power loss inside the parallel interrogation loop aside from the uncontrolled losses introduced by the optical modulators. There are several suggested ways to reduce the insertion losses either having a clean facet for the edge coupling along with using high numerical aperture (NA) optical fibers for coupling instead of the traditional SMF-28 fibers, or grating couplers suitable for the polymer photonics. The limitation on polystyrene fabrication, particularly for packing, will be removed by the usage of grating couplers. As a result, SU-8 will be replaced by polystyrene for the device layer, taking advantage of its higher performance.

Also, there is a need for further acoustic characterization experiments. The device's current bandwidth and sensitivity are constrained by the existing acoustic experimental setup. To address this limitation, it is recommended to use a fiber hydrophone exactly at the same location as the MRR under characterization, which would provide a reference for both the frequency spectrum and pressure values at different driving voltages of the ultrasound transmitter. The fiber hydrophones have the advantage of having a comparable size to the MRR which gives reasonable and reliable results that match the theoretical limits.

Moreover, in the dual optical frequency interrogation setup, the current electrooptic modulators have a limited bandwidth of $10GHz$ that may seem a large bandwidth from the electronic bandwidth, but it is optically just $80pm$ with a constrained input RF power. Larger bandwidth EOMs with high input power capabilities should be considered as an enhancement to the current setup. Additionally, current EOMs are used in an open loop control configuration which introduces some phase instability noise and a limited number of generated combs that should be considered to reach the quantum limit of detection offered by the optical frequency combs and hence reaching $mPa$ NEP ranges. From the integration point of view, a lot of research is performed on on-chip electrooptic modulators that will massively decrease the size of the all-optical detection systems, especially for potential clinical use.

Finally, the provided methodology in this thesis can be applied in various applications having ultrafast-acting phenomena and requiring high sensitivity and detection capabilities offered by microring resonators. For ultrasound imaging, the current design fits well with the techniques that are working on quite low acoustic frequencies $< 15MHz$ due to the current size of each microring resonator which relates to half of the acoustic wavelength. For high-frequency applications like photoacoustic, a trade-off between using the polymer material as the core material and lateral resolution should be taken into consideration while maintaining working at the same optical C-band. The dual optical frequency combs setup is tunable and can fit all the aforementioned applications. In that manner, and due to the dynamic characteristics of the implemented all-optical receiver system and the wide acoustic bandwidth of the MRRs, the current design can be tuned between both applications that require either low-speed scanning or high-speed imaging.

# REFERENCES


[1] "North america ultrasound devices market," Tech. Rep., January 2022. [Online]. Available: https://www.marketdataforecast.com/market-reports/north-america-ultrasound-devices-market

[2] T. L. Szabo, *Diagnostic ultrasound imaging: inside out*. Academic press, 2004.

[3] V. Chan and A. Perlas, "Basics of ultrasound imaging," *Atlas of ultrasound-guided procedures in interventional pain management*, pp. 13–19, 2011.

[4] O. Couture *et al.*, "Ultrasound localization microscopy and super-resolution: A state of the art," *IEEE Transactions on Ultrasonics, Ferroelectrics, and Frequency Control*, vol. 65, no. 8, pp. 1304–1320, 2018.

[5] J. Bercoff, "Ultrafast ultrasound imaging," *Ultrasound imaging-Medical applications*, pp. 3–24, 2011.

[6] M. Tanter and M. Fink, "Ultrafast imaging in biomedical ultrasound," *IEEE transactions on ultrasonics, ferroelectrics, and frequency control*, vol. 61, no. 1, pp. 102–119, 2014.

[7] J. Provost *et al.*, "3d ultrafast ultrasound imaging in vivo," *Physics in Medicine & Biology*, vol. 59, no. 19, p. L1, 2014.

[8] J. Provost, A. Garofalakis *et al.*, "Simultaneous positron emission tomography and ultrafast ultrasound for hybrid molecular, anatomical and functional imaging," *Nature biomedical engineering*, vol. 2, no. 2, pp. 85–94, 2018.

[9] J.-L. Gennisson *et al.*, "4-d ultrafast shear-wave imaging," *IEEE transactions on ultrasonics, ferroelectrics, and frequency control*, vol. 62, no. 6, pp. 1059–1065, 2015.

[10] H. S. Hashemi, S. E. Salcudean, and R. N. Rohling, "Ultrafast ultrasound imaging for 3d shear wave absolute vibro-elastography," *arXiv preprint arXiv:2203.13949*, 2022.

[11] E. E. Smith *et al.*, "Cerebral microinfarcts: the invisible lesions," *The Lancet Neurology*, vol. 11, no. 3, pp. 272–282, 2012.

[12] P. A. Tonino *et al.*, "Angiographic versus functional severity of coronary artery stenoses in the fame study: fractional flow reserve versus angiography in multivessel evaluation," *Journal of the American College of Cardiology*, vol. 55, no. 25, pp. 2816–2821, 2010.

[13] Y. T. Ling *et al.*, "Sonomechanomyography (smmg): Mapping of skeletal muscle motion onset during contraction using ultrafast ultrasound imaging and multiple motion sensors," *Sensors*, vol. 20, no. 19, p. 5513, 2020.

[14] J. Song *et al.*, "Ultrasound measurement using on-chip optical micro-resonators and digital optical frequency comb," *Journal of Lightwave Technology*, vol. 38, no. 19, pp. 5293–5301, 2020.

[15] K. K. Shung, *Diagnostic ultrasound: Imaging and blood flow measurements*. CRC press, 2005.

[16] W. R. Ali and M. Prasad, "Piezoelectric MEMS based acoustic sensors: A review," *Sensors and Actuators A: Physical*, vol. 301, p. 111756, 2020.

[17] C. Zhang *et al.*, "Imprinted polymer microrings as high-performance ultrasound detectors in photoacoustic imaging," *Journal of Lightwave Technology*, vol. 33, no. 20, pp. 4318–4328, 2015.

[18] H. Wang *et al.*, "MEMS ultrasound transducers for endoscopic photoacoustic imaging applications," *Micromachines*, vol. 11, no. 10, p. 928, 2020.

[19] I. G. Mina *et al.*, "High frequency piezoelectric MEMS ultrasound transducers," *IEEE transactions on ultrasonics, ferroelectrics, and frequency control*, vol. 54, no. 12, pp. 2422–2430, 2007.

[20] J. Wang *et al.*, "Capacitive micromachined ultrasound transducers for intravascular ultrasound imaging," *Microsystems and Nanoengineering*, vol. 6, no. 1, pp. 1–13, 2020.

[21] C. D. Gerardo, E. Cretu, and R. Rohling, "Fabrication and testing of polymer-based capacitive micromachined ultrasound transducers for medical imaging," *Microsystems and nanoengineering*, vol. 4, p. 19, 2018.

[22] B. T. Khuri-Yakub and Ömer Oralkan, "Capacitive micromachined ultrasonic transducers for medical imaging and therapy," *Journal of Micromechanics and Microengineering*, vol. 21, no. 5, p. 054004, apr 2011.

[23] G. Wissmeyer *et al.*, "Looking at sound: optoacoustics with all-optical ultrasound detection," *Light: Science & Applications*, vol. 7, no. 1, pp. 1–16, 2018.

[24] A. Parriaux, K. Hammani, and G. Millot, "Electro-optic frequency combs," *Adv. Opt. Photon.*, vol. 12, no. 1, pp. 223–287, Mar 2020.

[25] A. Foltynowicz *et al.*, "Optical frequency comb spectroscopy," *Faraday discussions*, vol. 150, pp. 23–31, 2011.

[26] I. Coddington, N. Newbury, and W. Swann, "Dual-comb spectroscopy," *Optica*, vol. 3, no. 4, pp. 414–426, Apr 2016.

[27] C. Errico *et al.*, "Ultrafast ultrasound localization microscopy for deep super-resolution vascular imaging," *Nature*, vol. 527, no. 7579, pp. 499–502, 2015.

[28] R. S. Cobbold, *Foundations of biomedical ultrasound*. Oxford university press, 2006.

[29] C. Zhang *et al.*, "Ultrabroad bandwidth and highly sensitive optical ultrasonic detector for photoacoustic imaging," *Acs Photonics*, vol. 1, no. 11, pp. 1093–1098, 2014.

[30] H. Li *et al.*, "Disposable ultrasound-sensing chronic cranial window by soft nanoimprinting lithography," *Nature communications*, vol. 10, no. 1, pp. 1–9, 2019.

[31] J. Bauer-Marschallinger, K. Felbermayer, and T. Berer, "All-optical photoacoustic projection imaging," *Biomedical optics express*, vol. 8, no. 9, pp. 3938–3951, 2017.

[32] H. Li *et al.*, "A transparent broadband ultrasonic detector based on an optical microring resonator for photoacoustic microscopy," *Scientific Reports*, vol. 4, no. 1, p. 4496, 2014.

[33] E. Zhang, J. Laufer, and P. Beard, "Backward-mode multiwavelength photoacoustic scanner using a planar fabry-perot polymer film ultrasound sensor for high-resolution three-dimensional imaging of biological tissues," *Applied optics*, vol. 47, no. 4, pp. 561–577, 2008.

[34] S. Preisser *et al.*, "All-optical highly sensitive akinetic sensor for ultrasound detection and photoacoustic imaging," *Biomedical optics express*, vol. 7, no. 10, pp. 4171–4186, 2016.

[35] W. Rohringer *et al.*, "All-optical highly sensitive broadband ultrasound sensor without any deformable parts for photoacoustic imaging," in *Photons Plus Ultrasound: Imaging and Sensing 2016*, vol. 9708. SPIE, 2016, pp. 230–237.

[36] S. Ashkenazi *et al.*, "Optoacoustic imaging using thin polymer etalon," *Applied Physics Letters*, vol. 86, no. 13, p. 134102, 2005.

[37] P. Hajireza *et al.*, "Glancing angle deposited nanostructured film fabry-perot etalons for optical detection of ultrasound," *Optics express*, vol. 21, no. 5, pp. 6391–6400, 2013.

[38] C. Zhang *et al.*, "Review of imprinted polymer microrings as ultrasound detectors: Design, fabrication, and characterization," *IEEE Sensors Journal*, vol. 15, no. 6, pp. 3241–3248, 2015.

[39] R. Shnaiderman *et al.*, "A submicrometre silicon-on-insulator resonator for ultrasound detection," *Nature*, vol. 585, no. 7825, pp. 372–378, 2020.

[40] W. Yang *et al.*, "Ultrasonic signal detection based on Fabry–Perot cavity sensor," *Visual Computing for Industry, Biomedicine, and Art*, vol. 4, no. 1, p. 8, 2021.

[41] J. A. Guggenheim *et al.*, "Ultrasensitive plano-concave optical microresonators for ultrasound sensing," *Nature Photonics*, vol. 11, no. 11, pp. 714–719, 2017.

[42] P. Morris *et al.*, "A fabry–pérot fiber-optic ultrasonic hydrophone for the simultaneous measurement of temperature and acoustic pressure," *The Journal of the Acoustical Society of America*, vol. 125, no. 6, pp. 3611–3622, 2009.

[43] S. M. Leinders *et al.*, "A sensitive optical micro-machined ultrasound sensor (omus) based on a silicon photonic ring resonator on an acoustical membrane," *Scientific reports*, vol. 5, no. 1, pp. 1–9, 2015.

[44] W. J. Westerveld *et al.*, "Sensitive, small, broadband and scalable optomechanical ultrasound sensor in silicon photonics," *Nature Photonics*, vol. 15, no. 5, pp. 341–345, 2021.

[45] S. Basiri-Esfahani *et al.*, "Precision ultrasound sensing on a chip," *Nature communications*, vol. 10, no. 1, pp. 1–9, 2019.

[46] T. J. Kippenberg and K. J. Vahala, "Cavity opto-mechanics," *Optics express*, vol. 15, no. 25, pp. 17 172–17 205, 2007.

[47] B.-B. Li *et al.*, "Cavity optomechanical sensing," *Nanophotonics*, vol. 10, no. 11, pp. 2799–2832, 2021.

[48] C.-Y. Chao *et al.*, "High-frequency ultrasound sensors using polymer microring resonators," *ieee transactions on ultrasonics, ferroelectrics, and frequency control*, vol. 54, no. 5, pp. 957–965, 2007.

[49] C.-y. Chao and L. J. Guo, "Polymer microring resonators fabricated by nanoimprint technique," *Journal of Vacuum Science & Technology B: Microelectronics and Nanometer Structures Processing, Measurement, and Phenomena*, vol. 20, no. 6, pp. 2862–2866, 2002.

[50] T. Ling, S.-L. Chen, and L. J. Guo, "Fabrication and characterization of high q polymer micro-ring resonator and its application as a sensitive ultrasonic detector," *Opt. Express*, vol. 19, no. 2, pp. 861–869, Jan 2011.

[51] S. Samanta, P. Banerji, and P. Ganguly, "Micro ring resonator using SU-8 waveguides for temperature sensor," *Optics InfoBase Conference Papers*, vol. 4, no. 1, pp. 4–6, 2014.

[52] P. Girault *et al.*, "Integrated polymer micro-ring resonators for optical sensing applications," *Journal of Applied Physics*, vol. 117, no. 10, p. 104504, 2015.

[53] Y. Chen, "Applications of nanoimprint lithography/hot embossing: a review," *Applied Physics A*, vol. 121, no. 2, pp. 451–465, 2015.

[54] J. Vinje, K. S. Beckwith, and P. Sikorski, "Electron beam lithography fabrication of su-8 polymer structures for cell studies," *Journal of Microelectromechanical Systems*, vol. 29, no. 2, pp. 160–169, 2020.

[55] W. Zhou, *Nanoimprint lithography: an enabling process for nanofabrication*. Springer Science & Business Media, 2013.

[56] T. Ling, S.-L. Chen, and L. J. Guo, "High-sensitivity and wide-directivity ultrasound detection using high q polymer microring resonators," *Applied Physics Letters*, vol. 98, no. 20, p. 204103, 2011.

[57] A. Maxwell *et al.*, "Polymer microring resonators for high-frequency ultrasound detection and imaging," *IEEE Journal of Selected Topics in Quantum Electronics*, vol. 14, no. 1, pp. 191–197, 2008.

[58] W. J. Westerveld *et al.*, "Acoustical pressure sensor with photonic waveguide," May 3 2022, US Patent 11,320,303.

[59] N. Picqué and T. W. Hänsch, "Frequency comb spectroscopy," *Nature Photonics*, vol. 13, no. 3, pp. 146–157, 2019.

[60] D. Fehrenbacher *et al.*, "Free-running performance and full control of a passively phase-stable er: fiber frequency comb," *Optica*, vol. 2, no. 10, pp. 917–923, 2015.

[61] A. Liehl *et al.*, "Deterministic nonlinear transformations of phase noise in quantum-limited frequency combs," *Physical review letters*, vol. 122, no. 20, p. 203902, 2019.

[62] T. Fortier and E. Baumann, "20 years of developments in optical frequency comb technology and applications," *Communications Physics*, vol. 2, no. 1, pp. 1–16, 2019.

[63] A. Shams-Ansari *et al.*, "An integrated lithium-niobate electro-optic platform for spectrally tailored dual-comb spectroscopy," *arXiv preprint*, 2020.

[64] J. T. Friedlein *et al.*, "Dual-comb photoacoustic spectroscopy," *Nature communications*, vol. 11, no. 1, pp. 1–10, 2020.

[65] J. Pan *et al.*, "Microbubble resonators combined with a digital optical frequency comb for high-precision air-coupled ultrasound detectors," *Photon. Res.*, vol. 8, no. 3, pp. 303–310, Mar 2020.

[66] ——, "Parallel interrogation of the chalcogenide-based micro-ring sensor array for photoacoustic tomography," *Nature Communications*, vol. 14, no. 1, p. 3250, 2023.

[67] H. Weng *et al.*, "Octave-spanning kerr frequency comb generation with stimulated raman scattering in an aln microresonator," *Optics Letters*, vol. 46, no. 3, pp. 540–543, 2021.

[68] R. Zhuang *et al.*, "Electro-optic frequency combs: Theory, characteristics, and applications," *Laser & Photonics Reviews*, p. 2200353, 2023.

[69] J. Li *et al.*, "Electro-optical frequency division and stable microwave synthesis," *Science*, vol. 345, no. 6194, pp. 309–313, 2014.

[70] V. Van, *Optical microring resonators: theory, techniques, and applications.* CRC Press, 2016.

[71] J. Heebner, R. Grover, and T. Ibrahim, *Optical microresonator theory.* Springer, 2008.

[72] E. A. J. Marcatili, "Dielectric rectangular waveguide and directional coupler for integrated optics," *The Bell System Technical Journal*, vol. 48, no. 7, pp. 2071–2102, 1969.

[73] W. J. Westerveld *et al.*, "Extension of marcatili's analytical approach for rectangular silicon optical waveguides," *Journal of Lightwave Technology*, vol. 30, no. 14, pp. 2388–2401, 2012.

[74] T. Ling, "High-q optical micro-cavity resonators as high sensitive bio-chemical and ultrasonic sensors," Ph.D. dissertation, University of Michigan, 2012.

[75] M. Hammer, K. R. Hiremath, and R. Stoffer, "Analytical approaches to the description of optical microresonator devices," in *AIP conference proceedings*, vol. 709, no. 1. American Institute of Physics, 2004, pp. 48–71.

[76] B. E. Saleh and M. C. Teich, *Fundamentals of photonics*. john Wiley & sons, 2019.

[77] K. H. Kim *et al.*, "Air-coupled ultrasound detection using capillary-based optical ring resonators," *Scientific reports*, vol. 7, no. 1, pp. 1–11, 2017.

[78] V. Govindan and S. Ashkenazi, "Bragg waveguide ultrasound detectors," *IEEE transactions on ultrasonics, ferroelectrics, and frequency control*, vol. 59, no. 10, pp. 2304–2311, 2012.

[79] D. T. Blackstock and A. A. Atchley, "Fundamentals of Physical Acoustics," *The Journal of the Acoustical Society of America*, vol. 109, no. 4, pp. 1274–1276, 04 2001.

[80] W. D. Sacher and J. K. S. Poon, "Dynamics of microring resonator modulators," *Opt. Express*, vol. 16, no. 20, pp. 15 741–15 753, Sep 2008.

[81] A. Parriaux, K. Hammani, and G. Millot, "Electro-optic frequency combs," *Adv. Opt. Photon.*, vol. 12, no. 1, pp. 223–287, mar 2020.

[82] C. E. M. Strauss, "Synthetic-array heterodyne detection: a single-element detector acts as an array," *Opt. Lett.*, vol. 19, no. 20, pp. 1609–1611, Oct 1994.

[83] D. Fried and J. Seidman, "Heterodyne and photon-counting receivers for optical communications," *Applied optics*, vol. 6, no. 2, pp. 245–250, 1967.

[84] C. W. Helstrom, "Detectability of coherent optical signals in a heterodyne receiver," *JOSA*, vol. 57, no. 3, pp. 353–361, 1967.

[85] P. Zhang *et al.*, "Simulation analysis of balance detection technique in coherent optical receiver," *Optics and Photonics Journal*, vol. 11, no. 8, pp. 301–313, 2021.

[86] C.-Y. Chao, W. Fung, and L. Guo, "Polymer microring resonators for biochemical sensing applications," *IEEE Journal of Selected Topics in Quantum Electronics*, vol. 12, no. 1, pp. 134–142, 2006.

[87] C. Lemieux-Leduc, "Microcavités à modes de galerie en polymère pour la détection de gaz," Ph.D. dissertation, Ecole Polytechnique, Montreal (Canada), 2019.

[88] X. Zhang *et al.*, "Complex refractive indices measurements of polymers in visible and near-infrared bands," *Applied optics*, vol. 59, no. 8, pp. 2337–2344, 2020.

[89] C. J. Robin, A. Vishnoi, and K. N. Jonnalagadda, "Mechanical behavior and anisotropy of spin-coated su-8 thin films for mems," *Journal of Microelectromechanical Systems*, vol. 23, no. 1, pp. 168–180, 2014.

[90] H. Lorenz *et al.*, "Su-8: a low-cost negative resist for mems," *Journal of Micromechanics and Microengineering*, vol. 7, no. 3, p. 121, 1997.

[91] T. Namazu *et al.*, "Visco-elastic properties of micron-thick su-8 polymers measured by two different types of uniaxial tensile tests," in *18th IEEE International Conference on Micro Electro Mechanical Systems, 2005. MEMS 2005.* IEEE, 2005, pp. 447–450.

[92] T. Xu *et al.*, "Characterization of the mechanical behavior of su-8 at microscale by viscoelastic analysis," *Journal of Micromechanics and Microengineering*, vol. 26, no. 10, p. 105001, 2016.

[93] F. Ay *et al.*, "Prism coupling technique investigation of elasto-optical properties of thin polymer films," *Journal of applied physics*, vol. 96, no. 12, pp. 7147–7153, 2004.

[94] J. E. Mark *et al.*, *Physical properties of polymers handbook*. Springer, 2007, vol. 1076.

[95] D.-Y. Chiou *et al.*, "Characterization and optimization design of the polymer-based capacitive micro-arrayed ultrasonic transducer," *Japanese Journal of Applied Physics*, vol. 46, no. 11R, p. 7496, 2007.

[96] J.-k. CHU, S.-l. LI, and R. ZHANG, "Micro-measurement of su-8 photoelastic performance," *Optics and Precision Engineering*, p. 03, 2016.

[97] S.-W. Youn *et al.*, "Microstructuring of su-8 photoresist by uv-assisted thermal imprinting with non-transparent mold," *Microelectronic Engineering*, vol. 85, no. 9, pp. 1924–1931, 2008.

[98] J. E. Mark, "Polymer data handbook, 2nd ed." *Journal of the American Chemical Society*, vol. 131, no. 44, pp. 16 330–16 330, 2009, pMID: 19764753.

[99] X. Zhang *et al.*, "Complex refractive indices measurements of polymers in visible and near-infrared bands," *Appl. Opt.*, vol. 59, no. 8, pp. 2337–2344, Mar 2020.

[100] F. Sabri *et al.*, "In vivo ultrasonic detection of polyurea crosslinked silica aerogel implants," *PLOS ONE*, vol. 8, no. 6, pp. 1–8, 06 2013.

[101] K. Lee *et al.*, "Micromachining applications of a high resolution ultrathick photoresist," *Journal of Vacuum Science & Technology B: Microelectronics and Nanometer*

*Structures Processing, Measurement, and Phenomena*, vol. 13, no. 6, pp. 3012–3016, 1995.

[102] G. H. Major *et al.*, "Spectroscopic ellipsometry of su-8 photoresist from 190 to 1680 nm (0.740–6.50 ev)," *Surface and Interface Analysis*, vol. 53, no. 1, pp. 5–13, 2021.

[103] S. Ashkenazi, T. Buma, and M. O'Donnell, "High frequency ultrasound detection using fabry-perot optical etalon," *IEEE Ultrasonics Symposium, 2004*, vol. 1, pp. 68–71, 2004.

[104] H. Jayatilleka *et al.*, "Crosstalk in soi microring resonator-based filters," *J. Lightwave Technol.*, vol. 34, no. 12, pp. 2886–2896, Jun 2016.

[105] S. Vilov, B. Arnal, and E. Bossy, "Overcoming the acoustic diffraction limit in photoacoustic imaging by the localization of flowing absorbers," *Opt. Lett.*, vol. 42, no. 21, pp. 4379–4382, Nov 2017.

[106] X. Tu *et al.*, "Ultrahigh q polymer microring resonators for biosensing applications," *IEEE Photonics Journal*, vol. 11, no. 2, pp. 1–10, 2019.

[107] M. Borselli, T. J. Johnson, and O. Painter, "Beyond the rayleigh scattering limit in high-q silicon microdisks: theory and experiment," *Optics express*, vol. 13, no. 5, pp. 1515–1530, 2005.

[108] J. K. Poon *et al.*, "Soft lithography replica molding of critically coupled polymer microring resonators," *IEEE Photonics technology letters*, vol. 16, no. 11, pp. 2496–2498, 2004.

[109] K. Sri, "Advanced analysis of biomedical signals," *Biomedical Signal Analysis for Connected Healthcare; Academic Press: Cambridge, MA, USA*, pp. 157–222, 2021.

[110] S. K. Mitra, *Digital signal processing: a computer-based approach*. McGraw-Hill Higher Education, 2001.

[111] H. Lan, *Soft UV nanoimprint lithography and its applications*. InTech New York, 2013.

[112] M. Madou, "Fundamentals of microfabrication and nanotechnology, three-volume set: The science of miniaturization," 2009.

[113] S. Yasin, D. Hasko, and H. Ahmed, "Comparison of mibk/ipa and water/ipa as pmma developers for electron beam nanolithography," *Microelectronic engineering*, vol. 61, pp. 745–753, 2002.

[114] L. E. Ocola, M. Costales, and D. J. Gosztola, "Development characteristics of polymethyl methacrylate in alcohol/water mixtures: a lithography and raman spectroscopy study," *Nanotechnology*, vol. 27, no. 3, p. 035302, 2015.

[115] D. Barbero *et al.*, "High-resolution nanoimprinting with a robust and reusable polymer mold," *Advanced Functional Materials*, vol. 17, no. 14, pp. 2419–2425, 2007.

[116] D. Qin, Y. Xia, and G. M. Whitesides, "Soft lithography for micro-and nanoscale patterning," *Nature protocols*, vol. 5, no. 3, p. 491, 2010.

[117] A. O'Neill, J. S. Hoo, and G. Walker, "Rapid curing of pdms for microfluidic applications," *Chips and Tips*, vol. 23, 2006.

[118] R. Guertin *et al.*, "Multi-gas detection using fabry-perot interferometers on silicon chip," *Sensors and Actuators B: Chemical*, vol. 335, p. 129655, 2021.

[119] L. Cheng *et al.*, "Grating couplers on silicon photonics: Design principles, emerging trends and practical issues," *Micromachines*, vol. 11, no. 7, p. 666, 2020.

[120] X. Mu *et al.*, "Edge couplers in silicon photonic integrated circuits: A review," *Applied Sciences*, vol. 10, no. 4, p. 1538, 2020.

[121] Y. Xu *et al.*, "Efficient polymer waveguide grating coupler with directionality enhancement," *Optics Communications*, vol. 463, p. 125418, 2020.

[122] C. Prokop *et al.*, "Air-suspended su-8 polymer waveguide grating couplers," *Journal of Lightwave Technology*, vol. 34, no. 17, pp. 3966–3971, 2016.

[123] M. Ibrahim *et al.*, "Athermal silicon waveguides with bridged subwavelength gratings for te and tm polarizations," *Optics express*, vol. 20, no. 16, pp. 18 356–18 361, 2012.

[124] P. Welch, "The use of fast fourier transform for the estimation of power spectra: a method based on time averaging over short, modified periodograms," *IEEE Transactions on audio and electroacoustics*, vol. 15, no. 2, pp. 70–73, 1967.

[125] S. Xiao *et al.*, "Toward a low-jitter 10 ghz pulsed source with an optical frequency comb generator," *Optics Express*, vol. 16, no. 12, pp. 8498–8508, 2008.

[126] C. Deakin, Z. Zhou, and Z. Liu, "Phase noise of electro-optic dual frequency combs," *Optics Letters*, vol. 46, no. 6, pp. 1345–1348, 2021.